

# Carbon Nanotube Based Electromechanical Probes

by

Onnik Yaglioglu

B.S., Bogazici University (1999)  
S.M., Massachusetts Institute of Technology (2002)  
S.M., Massachusetts Institute of Technology (2004)

Submitted to the Department of Mechanical Engineering  
in partial fulfillment of the requirements for the degree of

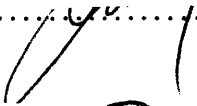
Doctor of Philosophy


at the

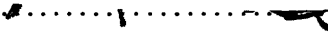
MASSACHUSETTS INSTITUTE OF TECHNOLOGY

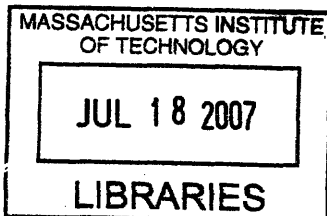
June 2007

© Massachusetts Institute of Technology 2007

Signature of Author .....  
 Department of Mechanical Engineering  
20 May 2007

Certified by .....  
 Alexander H. Slocum  
Professor of Mechanical Engineering, MacVicar Faculty Fellow  
Thesis Supervisor

Accepted by .....  
 Lallit Anand  
Chairman, Department Committee on Graduate Students



ARCHIVES



# Carbon Nanotube Based Electromechanical Probes

by

Onnik Yaglioglu

Submitted to the Department of Mechanical Engineering  
on 20 May 2007, in partial fulfillment of the  
requirements for the degree of  
Doctor of Philosophy

## Abstract

Electromechanical probing applications continuously require smaller pitches, faster manufacturing and lower electrical resistance. Conventional techniques, such as MEMS based cantilever probes have their shortcomings in terms of the lowest pitch that can be achieved, cost and yield. Given their promising mechanical and electrical properties, carbon nanotubes (CNTs) are strong candidates for future probing applications. A new class of metal-CNT hybrid electromechanical probes is presented where vertically aligned carbon nanotube structures, grown with a chemical vapor deposition (CVD) technique, act as elastic springs, and a metal coating on the probes is used for increased electrical conduction. This design and architecture presents a scalable approach where thousands of probes can be fabricated in very short production times. 1.5 Ohm resistance and reliable performance for 6000 cycles at 50  $\mu\text{m}$  over-travel was achieved for a column of  $200\mu\text{m}\times 200\mu\text{m}$  cross-section and  $1\mu\text{m}$  of Au deposition. In-situ scanning electron microscope mechanical compression tests revealed a unique deformation mechanism of the CNT structures where continued compression results in successive buckle formation which later can serve as micro-bellows and elastic springs. A novel stiffness tuning method is presented to control the elastic properties of a given CNT probe by controlling the initial compressing amount. Further stiffness tuning is achieved by changing gas composition during CVD growth where CNT diameter and density is modified. Lateral compression and densification tests show that these CNT structures are highly anisotropic and have very different deformation mechanisms in vertical and lateral directions. Mechanical properties resulting from two main CVD growth techniques, namely fixed catalyst where a thin film of catalyst layer is deposited onto the growth substrate, and floating catalyst where the catalyst particles are introduced in the gas phase, are compared. It is found that floating catalyst CVD growth yields much stiffer structures due to the relatively larger CNT diameters. As the adhesion of CNT structures to the growth substrate is very weak and the support layer is typically an insulator, a versatile transfer printing technique is developed which enables simultaneous placement and reinforcement of the probes on a wide range of substrates, including metals and printed circuit boards. Electromechanical performance and failure mechanisms of fully functional metal-CNT hybrid probes are presented.

Thesis Supervisor: Alexander H. Slocum

Title: Professor of Mechanical Engineering, MacVicar Faculty Fellow



# Acknowledgements

I have so many people to acknowledge who supported me along this long and winding road that I fear I will certainly miss someone. Many thanks to:

- Prof. Alex Slocum for being a very supportive and enthusiastic advisor, and a great friend.
- NSF and FormFactor Inc. for supporting my PhD project.
- Rod Martens from FormFactor Inc. for his continuous support and advice.
- John Gritters, Ben Eldridge and Igor Khandros from FormFactor Inc. for their support.
- My thesis committee: Profs. Jeff Lang, Brian Wardle, Carl Thompson and Jing Kong for their valuable comments and support.
- Colleagues at FormFactor Inc. who played a very important role in the completion of this thesis: Mike Harburn, Trelia Fang, Gaetan Mathieu, Mike Armstrong, Jim Williams, Brian Benson, Deborah Lawson, Jerry Tran, David Wang, Sangtae Park, Zhijun Zao, Sam Tor, Daniel Ngo, Huong Vu, Steven Uchimura, Simon Ko, Rigo Deleon, Rey Mercado, Randy Havener, Steve Van Tessel, Shoua Lo, Dominic Trucetta, Randy Drake (Therma), Scott Hansen (Therma), Mike (Therma), John (Therma), Pete Conrad, Robert Hernandez, Art Beverleigh (TPI Systems), Jason Martinez, Scott Hauser.
- Colleagues at University of Hawaii for the fruitful collaboration: Prof. Cao, Garret Minoru Hashiro and Xianglong Li.
- John Hart for his support throughout the project.

- Colleagues at MIT for their technical support: Kurt Broderick, Enrique Garcia, Manu Prakash, Patrick Boisvert, Tony Garret, Jae-Bum Joo.
- Staff at MIT for their tremendous help over the years: Leslie Regan and Maureen Lynch.
- Prof. Y.M. Chiang for sharing his laboratory for our nanotube growth facilities.
- Colleagues at PERG lab and TELAMS for their support.
- Alex Buxman from FEI for his help with in-situ SEM videos and FIB cutting.
- My parents Nisan and Iris Yaglioglu for their love, support, and for sacrificing so much from their life for my education since elementary school.
- My brother Burag Yaglioglu for being my best friend and for his incredible support.
- My ex-girlfriend Maral Bal for her love and support during the initial years of graduate school and the period when I was preparing for the qualifiers.
- Hachikian family for their love and support.
- My wonderful extended family for their love.
- My roommates Jason, Suzanne and April for being great roommates.
- Vahe Caliskan for his friendship, support and advice throughout graduate school.
- Kirk Bozdogan for his continuous support.

This thesis is dedicated to my parents.

# Contents

|          |   |           |
|----------|---|-----------|
| <b>1</b> | <b>Introduction</b>   | <b>19</b> |
| 1.1      | Carbon Nanotubes and Motivation for Probing Applications . . . . .                  | 19        |
| 1.2      | Objective, Scope, Contributions and Organization of the Thesis . . . . .            | 23        |
| <b>2</b> | <b>Carbon Nanotube Growth Methods and Column Manufacturing</b>                      | <b>27</b> |
| 2.1      | CNT Growth Techniques . . . . .   | 27        |
| 2.2      | Fixed Catalyst CVD Growth System . . . . .  | 28        |
| 2.3      | Floating catalyst CVD Growth System . . . . .                                       | 33        |
| 2.4      | Comparison of CVD Methods . . . . .   | 34        |
| 2.5      | Fabrication of CNT Columns . . . . .  | 36        |
| <b>3</b> | <b>Mechanical Characterization of Vertically Aligned Carbon Nanotube Structures</b> | <b>41</b> |
| 3.1      | Experimental Setup and Testing Issues . . . . .                                     | 41        |
| 3.1.1    | Tribometer . . . . .  | 42        |
| 3.1.2    | In-Situ SEM Compression . . . . .   | 44        |
| 3.2      | Deformation Mechanism of CNT Columns Grown with Fixed Catalyst CVD . . . . .        | 46        |
| 3.2.1    | Initial Observations . . . . .  | 46        |
| 3.2.2    | In-situ SEM Compression . . . . .   | 49        |
| 3.2.3    | Detailed Testing with Tribometer . . . . .  | 51        |
| 3.2.4    | Modeling and Analysis . . . . .   | 59        |
| 3.2.5    | Effect of Column Area on Stiffness . . . . .  | 62        |
| 3.2.6    | Lateral Stiffness of Vertically Aligned CNT Structures . . . . .                    | 64        |

|          |  |            |
|----------|--|------------|
| 3.2.7    | Hydrogen Preconditioning of Catalyst . . . . .   | 66         |
| 3.3      | Deformation Mechanism of Columns Grown with Floating Catalyst CVD . . . . .                        | 70         |
| 3.3.1    | Initial Observations and In-situ SEM compression . . . . .   | 70         |
| 3.3.2    | Detailed Testing with Tribometer . . . . .   | 71         |
| 3.4      | Fundamental Findings and Guidelines for Probe-Design . . . . .                                     | 74         |
| 3.4.1    | Effect of CVD Growth Method and Parameters on Mechanical Properties<br>of CNT Structures . . . . . | 75         |
| 3.4.2    | Summary of Findings for Fixed catalyst CNT Structures . . . . .                                    | 75         |
| 3.4.3    | Summary of Findings for Floating catalyst CNT Structures . . . . .                                 | 78         |
| <b>4</b> | <b>Transfer of CNT Structures onto Conductive Substrates and Electrical Char-</b>                  |            |
|          | <b>acterization</b> . . . . .  | <b>81</b>  |
| 4.1      | Transfer Process . . . . .   | 84         |
| 4.2      | Internal Structure . . . . .   | 84         |
| 4.3      | Practical Issues and Yield . . . . .   | 88         |
| 4.4      | Electromechanical Characterization . . . . .   | 88         |
| 4.5      | Electrical Characterization Discussion . . . . .   | 93         |
| <b>5</b> | <b>Hybrid Metal-CNT Electromechanical Probes</b> . . . . .   | <b>95</b>  |
| 5.1      | Strategies for Probe Design and Manufacturing . . . . .  | 95         |
| 5.2      | Metal Deposition Techniques . . . . .  | 96         |
| 5.2.1    | Electroless Plating . . . . .  | 96         |
| 5.2.2    | Sputter Deposition . . . . .   | 98         |
| 5.3      | Probe Development . . . . .  | 100        |
| 5.4      | Electromechanical Characterization . . . . .   | 105        |
| 5.5      | Failure Mechanisms . . . . .   | 106        |
| <b>6</b> | <b>Other Applications: Nano Art</b> . . . . .  | <b>111</b> |
| <b>7</b> | <b>Conclusions and Recommendations for Future Work</b> . . . . .                                   | <b>121</b> |
| 7.1      | Summary . . . . .  | 121        |
| 7.2      | Recommendations for Future Work . . . . .  | 124        |



# List of Figures

|     |  |    |
|-----|--|----|
| 1-1 | (a) A single wall carbon nanotube (SWNT), (b) A multi-wall carbon nanotube (MWNT), a double-wall carbon nanotube (DWNT) (from [1]). . . . .  | 21 |
| 1-2 | Probe card and microsprings by FormFactor Inc. (courtesy of FormFactor, Inc.) .  | 22 |
| 1-3 | Interdependancies of physical properties for structures made of carbon nanotubes.  | 25 |
| 2-1 | Comparison of growth techniques yielding VA-CNT films. For viable industrial applications, upper right corner is most desirable. . . . .   | 28 |
| 2-2 | Schematics of the furnace used to grow vertically aligned carbon nanotube columns from "fixed catalyst". . . . .   | 29 |
| 2-3 | Initial stages of vertical growth with base growth. (a) Sketch depicting random initial growth direction and inactive catalyst aprticles which don't yield CNTs. (b) Schematics of base growth. . . . .  | 30 |
| 2-4 | Initial stages of growth with the base growth mechanism obtained with the fixed catalyst CVD method. (a) Circular pattern. (b) Close-up image of a corner of transition between patterned layer and the support layer where no CNT growth occurs. Empty spots, due to inactive catalyst particles, can be seen. (c, d) Close up images of the empty spots showing the inactive catalyst particles and tangled CNT film formation from the neighbouring catalyst particles. . . . . | 31 |
| 2-5 | Sketch demonstrating vertical growth of CNTs and formation of forests. . . . .   | 32 |
| 2-6 | Schematics of the furnace used to grow vertically alligned carbon nanotube films from floating catalyst. . . . .   | 33 |

|      |   |    |
|------|---|----|
| 2-7  | Close-up images of a column side wall grown with floating catalyst CVD. (a) CNT diameter measurements in SEM. (b) SEM image taken with back scattered electrons showing the bright iron nanoparticles acting as catalyst during the growth. . . . .   | 34 |
| 2-8  | SEM images at increasing magnification of CNT column sidewalls grown with different CVD processes. . . . .  | 35 |
| 2-9  | (a) Typical TEM image used to measure outer diameter and inner diameter of CNTs. (b) A close up image of a CNT. Both pictures correspond to CNTs grown with argon flush. . . . .  | 36 |
| 2-10 | Unit CNT film area used to calculate average CNT-CNT spacing. . . . .   | 37 |
| 2-11 | CNT columns grown with fixed catalyst CVD method (hydrogen flush). Pitch, shape and height of the columns can be easily controlled by patterning and by growth time respectively. . . . .   | 39 |
| 2-12 | Columns grown with floating catalyst CVD method. . . . .  | 40 |
| 2-13 | Columns of different shapes grown with floating catalyst CVD method. . . . .  | 40 |
| 3-1  | (a) Schematics of the experimental setup. As the punch, a 1.6 mm diameter brass rod is used. (b) Photograph of the tribometer used for mechanical characterization. (c) In-situ monitoring of CNT columns during compression with 2 perpendicular cameras. (courtesy of FormFactor, Inc.) . . . . . | 42 |
| 3-2  | Components of the tribometer: The load sensor attached to the deformation stage which moves vertically through a leadscrew assembly. (courtesy of FormFactor, Inc.) . . . . .   | 43 |
| 3-3  | Sketch depicting the backlash issue for 10 $\mu$ m backlash, which makes it impossible to characterize columns at deformations near or smaller than 10 $\mu$ m. . . . .   | 44 |
| 3-4  | (a,c) Components of the in-situ SEM probing system. (b) SEM image of the probe inside the SEM chamber used to compress CNT structures for in-situ characterization. (courtesy of FormFactor, Inc.) . . . . .  | 45 |

|      |  |    |
|------|--|----|
| 3-5  | (a) Successive buckle formation: number of buckles is the same as number of the ripples observed during testing, indicating that each ripple corresponds to a buckle formation. (b) Number of buckles is proportional to the imposed deformation. . . . .          | 47 |
| 3-6  | (a) Close up SEM image of a corner from a CNT column before deformation (fixed catalyst growth with argon flush). (b) Close up image of the buckles formed during deformation depicting regular buckled shapes and plastic deformation. . . . .                    | 48 |
| 3-7  | (a) SEM image of a column and probe after compression showing buckle formation at the top portion where the probe and column touch. (b) Regular buckle patterns formed at the top portion having identical patterns as buckles form at the bottom section. . . . . | 49 |
| 3-8  | CNT columns of various shapes forming similar buckles upon compression (fixed catalyst growth with Argon flush). (a) Triangular column. (b) Hexagonal column. (c) Cross shaped column. . . . .   | 50 |
| 3-9  | Shape and size of the buckles formed are inherent properties of the CNTs the columns are made of. Bottom sections of circular columns grown by fixed catalyst CVD with (a) argon flush and (b) helium and hydrogen flush after deformation. . . . .                | 51 |
| 3-10 | Successive buckle formation of CNT column under compression. Images are taken during in-situ SEM compression test. . . . .   | 52 |
| 3-11 | (a) In-situ SEM buckle formation test. (b) Elastic recovery during release of the probe. . . . .   | 53 |
| 3-12 | (a) Breathing bellow-like buckles during testing. This elastic range can be used as a spring for various applications. (b) Close-up snapshots of a buckle before and after compression showing individual buckles shrink and expand during testing. . . . .        | 54 |
| 3-13 | Sketch demonstrating the test procedure where CNT columns are successively compressed to larger deformations resulting in increased number of buckles (a) 5 buckles. (b) 10 buckles. (c) 15 buckles. . . . .   | 56 |
| 3-14 | Sketch depicting mechanical behavior of CNT columns. Note that elastic recovery occurs through different stiffnesses depending on number of buckles formed during compression: (a) 5 buckles, $k_5$ (b) 10 buckles, $k_{10}$ (c) 15 buckles, $k_{15}$ . . . . .    | 57 |

|      |  |    |
|------|--|----|
| 3-15 | (a) Compression test results of CNT column with $400\mu m$ diameter. The compression cycles are performed in $50\mu m$ increments. (b) Second touchdown tests performed after each cycle before imposing the next incremental deformation, demonstrating elastic operation after any cycle without forming a new buckle. (c) Stiffness values measured during elastic recovery or initial compression of the next cycle. The stiffness values are plotted against the corresponding number of buckles (approximate). . . . . | 58 |
| 3-16 | Cylindrical element with length $L$ and crosssectional area of $A$ . . . . .   | 59 |
| 3-17 | (a) Definitions used in the deformation model. (b) Model of CNT column deformation where each buckled layer adds a new springs in series, thereby reducing overall stiffness of the structure. (c) Model correlation with test data. . . . .   | 61 |
| 3-18 | (a) Mask for the test structures. (b) Columns grown to various shapes with floating catalyst CVD. . . . .  | 63 |
| 3-19 | Stiffness of the CNT columns is proportional to the cross-sectional area of the column. Stiffness values of various area columns are plotted after different compression amounts. . . . .  | 64 |
| 3-20 | (a) A compressed column cut with focused ion beam (FIB) to see the cross-section of the column after buckle formation. (b) Half of the column removed. Buckled region spans the whole cross-section. (c, e) Close-up images of the the corner of the column and (d) middle section showing the transition from unbuckled region to buckled region. (f) Regular corner of a buckled column for comparison with cut corner. . . . .  | 65 |
| 3-21 | (a) Test configuration to characterize lateral stiffness of CNT column. (b) Test data showing that as the column gets densified, its stiffness increases. There is again large plastic deformation followed with relatively short elastic recovery. (c) Comparison of stiffness change during vertical and lateral compression. . . . .  | 67 |
| 3-22 | (a) SEM images of the sidewall of a CNT column before densification. (b) SEM simages of the sidewall after $300\mu m$ compression. . . . .   | 68 |

|  |    |
|--|----|
| 3-23 (a) Compression test and successive buckle formation of a CNT column grown with fixed catalyst method using hydrogen flush throughout the CVD process.  |    |
| (b) Stiffness values corresponding to successive buckles. . . . .  | 69 |
| 3-24 Effect of hydrogen flush throughout the CVD growth. The stiffness of the same size column under same test conditions increase four times. . . . .   | 70 |
| 3-25 In-situ SEM compression test snapshots of a CNT column grown with floating catalyst recipe. The images show the bottom section of the column. (a) Compression. (b) Subsequent release, showing the buckled region recovers elastically.   | 71 |
| 3-26 Close-up snapshots of the corner of a CNT column grown with floating catalyst during in-situ compression test. . . . .  | 72 |
| 3-27 (a) Compression test results of CNT columns grown with floating catalyst. (b) Average stiffness of the CNT columns plotted against column area. . . . .   | 73 |
| 3-28 Ashby chart comparing mechanical properties of CNT structures grown with various CVD growth methods with conventional materials. . . . .  | 76 |
| 3-29 Stiffness map of various geometry and compression level CNT columns which can be used for design purposes. . . . .  | 78 |
|  |    |
| 4-1 Fabrication sequence of the CNT columns. The columns are grown from a patterned catalyst on silicon substrate, and then transferred onto a copper substrate using a thin conductive epoxy. . . . .   | 83 |
| 4-2 Transfer process from silicon substrate to a copper substrate using a thin film of epoxy. (a) As-grown columns on silicon substrate. (b), (c) Copper substrate, epoxy layer, CNT columns and silicon substrate assembly after curing. (d) Composite CNT columns on copper substrate after separation from silicon substrate. Uniform height after growth, alignment of the two substrates and pressure applied prior curing are critical for a good transfer. SEM images of (e) as grown MWNT columns from patterned catalyst and (f) large array of transferred columns onto copper substrate. Note the “mushroom” structures. The scaling bar in (e) corresponds to 2 mm and scaling bar in (f) correspond to 500 $\mu$ m. | 85 |
| 4-3 (a) Transferred columns of various pitches and cross-sections. (b) Close up image of transferred columns with 100 $\mu$ m pitch and 50 $\mu$ m x 50 $\mu$ m cross-section . . .  | 86 |

|     |  |    |
|-----|--|----|
| 4-4 | (a) SEM image of a composite CNT micro-probe. The CNT columns typically shrink to 80% of their original width due to capillary action of penetrating composite resin during curing process (b) Cross-section of the micro-probe after cutting with laser beam. The cross-section shrinks to 27% of its original area. The density increases from $8.1\text{kg}/\text{m}^3$ to $1070\text{ kg}/\text{m}^3$ . (c) Cross-section of the micro-probe after cutting using a microtome. The scaling bar in (a) corresponds to $200\ \mu\text{m}$ , and scaling bars in (b) and (c) correspond to $50\mu\text{m}$ . . . . . | 86 |
| 4-5 | (a) SEM image of sidewall of CNT column before curing. (b) SEM image of sidewall of CNT column after curing. (c) SEM image of the bottom of a CNT column showing silver particles, which stay at the roots, and do not penetrate into the structure. The scaling bar in (a) and (b) correspond to $5\ \mu\text{m}$ , and scaling bar in (c) correspond to $20\mu\text{m}$ . . . . .  | 87 |
| 4-6 | Partial transfer due to non-uniform height of as grown columns.(a) Close-up image showing the substrate with CNT columns come into contact with the transfer substrate. Due to nonuniform growth, there are regions which do not come into contact with the conductive epoxy. (b) Silicon and copper substrates after the transfer. . . . .  | 88 |
| 4-7 | Experimental setup for electromechanical characterization of CNT columns and composite micro-probes. Applied force, and voltage drop are measured, while displacement and current are imposed. . . . .   | 89 |
| 4-8 | (a) Stress-strain curve and electrical resistance of a micro-probe under a full cycle of loading and unloading. Force relaxation occurs when the displacement is held constant. Note constant resistance plateau and large permanent deformation after compression. (b) Time histories of stress and strain better illustrate the force relaxation. . . . .  | 91 |
| 4-9 | Ashby chart comparing as grown columns and transferred columns with conventional materials. Note the very low density and relatively large modulus of as grown columns. . . . .  | 92 |
| 5-1 | Strategies for electromechanical probe design and manufacturing. . . . .   | 96 |

|      |   |     |
|------|---|-----|
| 5-2  | SEM images of electroless plated Pd on CNT films grown with fixed catalyst CVD method. . . . .  | 97  |
| 5-3  | SEM images of electroless plated Pd on CNT film grown with floating catalyst CVD technique. Electroless depositions results in intrinsic stress. . . . .  | 98  |
| 5-4  | Film evolution during sputter deposition of Pd onto CNT film grown with fixed catalyst CVD method. . . . .  | 99  |
| 5-5  | TEM images of Pd sputtered CNTs showing full coverage. . . . .  | 100 |
| 5-6  | Film evolution during sputter deposition of Pd onto CNT film grown with floating catalyst CVD method. . . . .   | 101 |
| 5-7  | Pictures of hybrid metal-CNT probes. . . . .  | 102 |
| 5-8  | Hybrid electromechanical probes made by sputtering Au onto CNT columns grown with floating catalyst CNT method. (a-d) 200 $\mu m$ pitch square columns sputtered with Au for 24 minutes. (f-h) 400 $\mu m$ pitch square columns sputtered with Au for 12 minutes.(d) and (f) are close-up images of the top surfaces of the sputtered CNT columns. Even though the main difference is the sputter time, it is easy to note that the top surface of the larger columns are much smoother, which is a result of the growth process, particularly the termination of the growth and total growth time. The two different size columns were grown at separate CVD runs. . . . . | 103 |
| 5-9  | CNT side-wall coverage after different durations of metall sputtering. . . . .  | 104 |
| 5-10 | Au sputtered CNT column cut with FIB to observe Au penetration into the structure. . . . .  | 105 |
| 5-11 | Close-up SEM images of sections of Au sputtered CNT columns cut with FIB. (a) Sputtered film penetration after 4min. of Au deposition. (b) Sputtered film penetration after 24 min. Au deposition. . . . .  | 106 |
| 5-12 | Performance of a 200 $\mu m$ diameter hybrid metal-CNT probe under cyclic load. . .   | 107 |
| 5-13 | Electromechanical probe performance and comparison with two different porosity outer metal shell. . . . .   | 107 |

|      |  |     |
|------|--|-----|
| 5-14 | Failure mechanisms observed during deformation hybrid CNT-Au electromechanical probes. (a) A circular Au sputtered (24min) column before deformation. (b) Same column after deformation showing failures at the top and bottom. Due to the thick top Au layer, as well as due to the inherent property of the top surface resulting from the termination of the CVD process, the top "cap" comes off. The outer metal layer also peels off at the bottom where the buckling and deformation occurs. (c) A square column shown after deformation where the top cap comes off, but the bottom section failure is not as drastic. (d) Close up image of the bottom section showing traces of deformation, but experiments show that electrical continuity is maintained due to the large number of CNTs remaining in contact. . . . . | 108 |
| 6-1  | Controlled buckling of CNT structures. . . . .   | 112 |
| 6-2  | Controlled buckling of CNT structures. . . . .   | 113 |
| 6-3  | Controlled buckling of CNT structures. . . . .   | 114 |
| 6-4  | Focused ion beam (FIB) cutting and etching of metal-CNT hybrid columns. . .  | 115 |
| 6-5  | FIB cutting and etching of CNT structures. . . . .   | 116 |
| 6-6  | Sputter etching of CNT film. . . . .   | 117 |
| 6-7  | Sputtered Au onto CNT film. . . . .  | 118 |
| 6-8  | Electroless plating of Pd onto CNT film. . . . .   | 119 |
| 7-1  | Failure mechanism of metal layer around a CNT. . . . .   | 128 |
| 7-2  | Hollow cylinder column design. . . . .   | 129 |



# List of Tables

|     |  |    |
|-----|--|----|
| 2.1 | Process condition for the growth with Argon flush. . . . .   | 29 |
| 2.2 | Process condition for the growth with Hydrogen flush.. . . .   | 30 |
| 2.3 | Process conditions for CVD growth with floating catalyst. . . . .  | 33 |
| 2.4 | Comparison of resulting CNT properties from different recipes. . . . .   | 37 |
| 2.5 | Image reversal process used to lift-off metal layer (Fe for fixed catalyst growth and Au for floating catalyst growth) for desired pattern and column shape. . . .   | 38 |
| 4.1 | Comparison of the mechanical properties of as-grown and transferred columns. .   | 90 |
| 4.2 | Comparison of individual CNT resistance for vertically aligned CNT bundles at comparable scales. It should be noted that resistance values include both contact and bulk resistance; hence we the values are not normalized with respect to bundle length. . . . . | 94 |
| 5.1 | Contents of the solution used for electroless plating of Pd onto CNT films. . . .  | 97 |



# Chapter 1

## Introduction

This chapter presents a brief introduction into the science of carbon nanotubes, motivation for the thesis work, objective and scope of the thesis, organization of the thesis and a summary of fundamental contributions.

### 1.1 Carbon Nanotubes and Motivation for Probing Applications

Carbon nanotubes have many potential benefits in many industries, and despite more than 15 years of research since their discovery, many aspects of the science, including the very mechanism of the growth, still remains under investigation. It is worthwhile to quote Richard E. Smalley, Chemistry Nobel Laureate 1996 from his preface to the book "Carbon Nanotubes: Synthesis, Structures, Properties, and Applications"[2]:

*It is clear to most of us working in this field that we have only just begun. The potential is vast. Here we have what is almost certainly strongest, stiffest, toughest molecule that can ever be produced, the best molecular conductor of both heat and electricity. In one sense the carbon (fullerene) nanotube is a new man-made polymer to follow on from nylon, polypropylene, and kevlar. In another, it is a new "graphite" fiber, but now with the ultimate possible strength. In yet another, it is a new species in organic chemistry, and potentially in molecular biology as well, a carbon molecule*

*with the almost alien property of electrical conductivity, and super-steel strength.*

*Houston, Texas, January 2001*

A carbon nanotube (CNT) is a rolled graphene sheet, or a collection of them, into the shape of a tube (Figure 1-1). The main attributes of a carbon nanotube are:

- *Number of walls:* This is a measure of how many concentric rolled graphene sheets are forming the CNT. This basically determines if the CNT is single walled (SWNT) or multi-walled (MWNT).
- *CNT diameter:* The diameter of a CNT has wide implications on its physical properties such as optical, electrical and magnetic, mainly due to changing bandgap, as well as mechanical properties, mainly due to changing number of bonds holding carbon atoms together.
- *CNT wall thickness:* This can be calculated by multiplying number of walls by wall to wall distance of 0.34 nm. Number of walls also dictates the inner diameter of the carbon nanotube.
- *Chirality:* The chirality refers to the rolling angle of the graphene sheet which was used to create the carbon nanotube. Chirality has a direct effect on the bandgap and thereby on the electrical properties of the CNT, as well as mechanical properties.

Important attributes of a collection of CNTs are:

- *Average CNT to CNT spacing:* This determines the spatial density of CNTs.
- *Average length of CNTs:* This determines the CNT film or forest thickness.
- *Alignment:* This is a measure of the orientation of the CNTs within the film. This has important implications on mechanical and electrical properties of the assembly. Due to the one dimensional nature of the CNTs, any level of alignment translates into anisotropy in mechanical and electrical properties.

Direct control or tuning of any of the above attributes independently, whether it is an attribute of an individual CNT or a collection of CNTs, is an outstanding challenge. Usually,

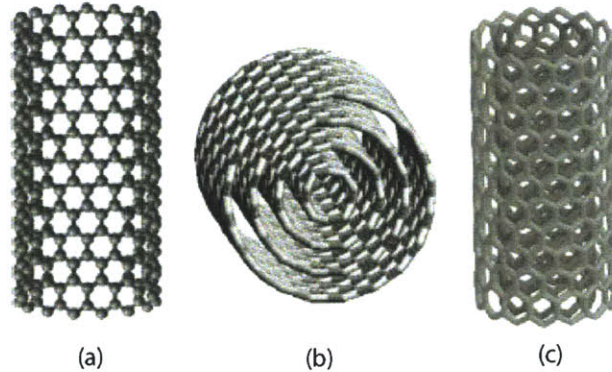


Figure 1-1: (a) A single wall carbon nanotube (SWNT), (b) A multi-wall carbon nanotube (MWNT), a double-wall carbon nanotube (DWNT) (from [1]).

the ability of controlling one attribute comes in the expense of affecting another attribute as well. For example, as will be discussed in Chapter 2, control of CNT density is achieved in the expense of a change in the CNT diameter in the undesirable direction, namely a decrease in average CNT diameter.

Due to their outstanding electrical and mechanical properties including high stiffness and mechanical resilience, ballistic electron transport at micron-scales, and high current-carrying capacity [2], carbon nanotubes (CNTs) could enable a new class of electrical elements ranging from transistors to interconnects. However, realizing the properties of individual CNTs in assemblies of CNTs has been a formidable challenge. Realistic applications of CNTs at micro-scales must employ thousands or millions of CNTs in a parallel fashion and the understanding of the electromechanical behavior is not mature enough. Most of the research so far has been either for sensing [3], or actuation applications [4, 5, 6, 7, 8], whereas their potential benefit in probing applications have not been investigated, where obtaining both mechanical integrity and electrical conduction is critical.

Electromechanical probing applications continuously require smaller pitches, faster manufacturing and lower electrical resistance. One of the industries which utilizes contacting electro-mechanical probes is the probe-card industry where the goal is to test semiconductor chips while still on the wafer in a very reliable manner. A probe-card by FormFactor Inc. is shown in Figure 1-2 which uses MEMS based cantilever probes which have certain shortcomings in

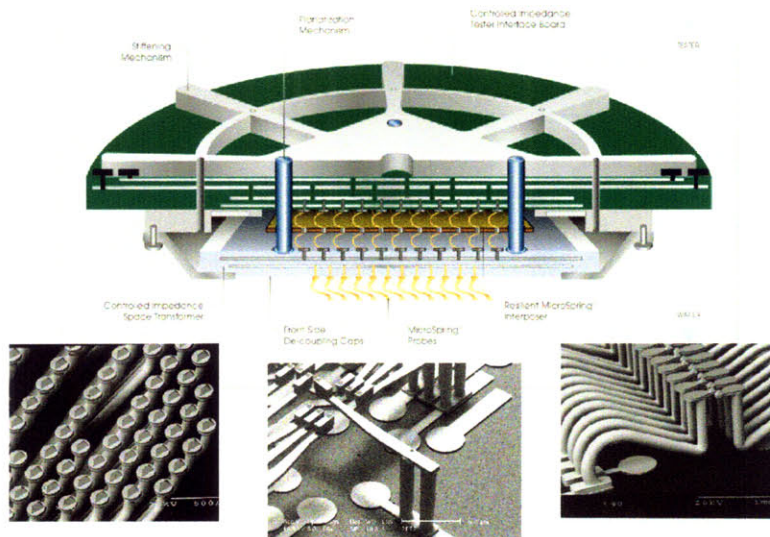


Figure 1-2: Probe card and microsprings by FormFactor Inc. (courtesy of FormFactor, Inc.)

terms of lowest pitch that can be achieved, cost and yield. The requirements for probe properties are driven by the semiconductor industry where the chip size continue to shrink. In this context, vertical probing architectures gain particular attention to achieve lower pitches. However, to achieve low pitch structures without compromising elastic properties is a challenge with conventional materials. Due to their very resilient nature, carbon nanotubes are attractive alternatives for electromechanical probing applications and could play an important role in the development of the next generation probes. Also, CNT based probe architecture presents a scalable approach where thousands of probes can be fabricated in very short production times in full wafer batch fabrication minimizing the fabrication steps currently necessary with the conventional methods, which can also have significant cost benefits.

Basic functional requirements for electromechanical probes are:

- Manufacturability
- Low pitch without interference ( $\leq 50\mu m$ )
- Low electrical resistance ( $\leq 1\Omega$  per probe)
- Cyclic operation ( $\geq 10^6$  touchdowns)

- Ability to tune the stiffness ( $\sim 10g/mil$ )
- High compliance at low pitch
- Planarization effect
- Current carrying capacity
- High temperature operation

Ability to tune the stiffness of a given probe with a certain geometry, among other requirements listed above, is quite challenging, and impossible for a given material and geometry. As will be discussed later in Chapter 2 and Chapter 3, CNT architectures allow interesting and novel tuning mechanisms, which is one of the fundamental contributions of this work.

## 1.2 Objective, Scope, Contributions and Organization of the Thesis

This thesis deals with vertically aligned multi-walled carbon nanotubes grown by chemical vapor deposition (CVD). For scalable applications and particularly for applications in electromechanical probing, as will be discussed in more detail in Chapter 2, carbon nanotubes grown with this method are the most suitable due to their length and inherent properties. For the past 15 years, researchers working with the CVD growth method have been mostly concerned about the growth rate and if the tubes are single walled or multi-walled. However, for most of the potential applications, the improvements in the growth rate aren't of particular interest. The inherent properties of the CNTs, especially the attributes of a collection of CNTs discussed in the previous section are much more important for the desired mechanical and electrical performance. This thesis makes an attempt to relate growth conditions to the ultimate mechanical properties of the resulting structure. As mentioned earlier, the ability to tune the attributes of a CNT film is limited, an understanding of how those attributes affect their performance would greatly help and give insight in terms of how to design experiments properly to obtain desired tuning.

The thesis investigates the use of two CVD growth mechanisms for probing applications, namely *fixed catalyst* where a thin film of catalyst layer is deposited onto the growth substrate; and *floating catalyst* where the catalyst particles are introduced in the gas phase. Method of CNT probe/column fabrication is discussed, and issues such as height uniformity and loading effects are discussed. CNTs resulting from each CVD growth are characterized by scanning electron microscopy and transmission electron microscopy to obtain accurate measurements of CNT diameter and number of walls. Furthermore, a variation of the fixed catalyst CVD method, where the gas composition is changed, is investigated. Then columns made of these techniques are mechanically characterized with a high resolution tribometer as well as in-situ scanning electron microscope.

The objective of the thesis, summarized in Figure 1-3, is to correlate inherent CNT properties to ultimate mechanical and electrical properties, and thereby linking the fabrication methods directly to the performance metrics by understanding the underlying mechanisms. The approach of the thesis is to characterize CNT structures on macro level and correlating them to the inherent properties of CNTs to get fundamental understanding. The thesis further investigates effect of geometry, and external modifications on CNT probe performance such as metal deposition onto the probes.

The organization of the thesis is as follows:

Chapter 2 discusses CNT growth techniques used in the thesis, their main differences and the resulting CNT properties in terms of their diameter, number of walls and density. It presents the fabrication method used for CNT probes and discusses the growth mechanism causing vertical growth, which is the main enabler of the column manufacturing. Chapter 3 presents the mechanical characterization of columns made of vertically aligned carbon nanotubes (VA-CNTs). Column grown with the three methods described in Chapter 2 are tested and compared in terms of their mechanical properties. It also presents deformation models and design guidelines for probe fabrication. Chapter 4 presents a transfer printing technique onto conductive substrate to achieve mechanical adhesion as well as electrical connection to the base substrate, which also in densification and stiffening of the CNT structures. Mechanical and electrical characteristics of transferred probes are presented. Chapter 5 presents metal film formation on CNT structures, metal-CNT hybrid electromechanical probes, their performance



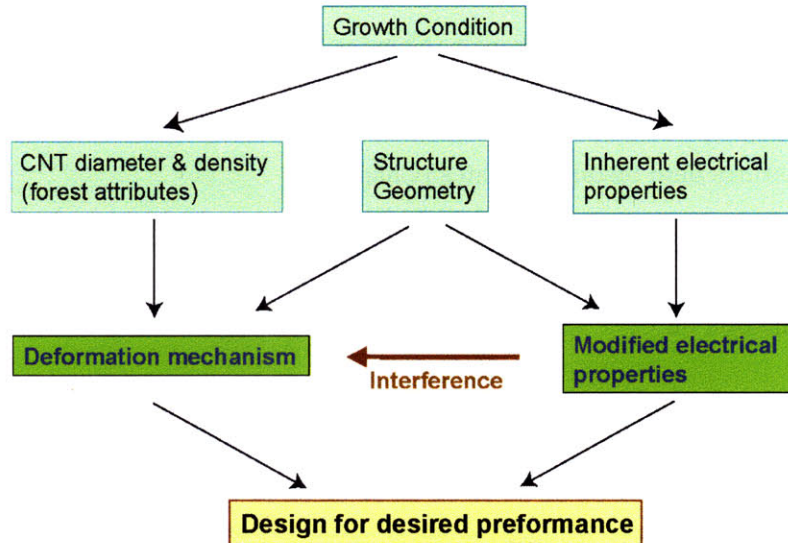


Figure 1-3: Interdependencies of physical properties for structures made of carbon nanotubes.

and failure mechanisms. Chapter 6 presents another application of the growth methods and techniques used in this thesis, namely nano-art. SEM images of CNT structures after various processes such as sputter etching, focused ion beam milling, reactive ion etching, controlled buckling and electroless metal deposition is presented without any post processing. Chapter 7 summarizes important results and conclusions presented in previous chapters, fundamental contributions of this thesis and presents recommendations for future work.

Fundamental contributions of this work are:

- Methodology for mechanical characterization of VA-CNT structures (Chapter 3).
- Identification of a buckling based deformation mechanism for compressed CNT structures (Chapter 3).
- Demonstration of stiffness tuning of a CNT structure by controlled compression and buckle formation (Chapter 3).
- Demonstration of stiffness tuning by controlling gas composition during growth (Chapter 3).

- Investigation of the relationship between CNT growth method, resulting CNT structures, and macro-scale mechanical behavior (Chapter 3).
- Transfer printing technique to simultaneously transfer, densify and electrically connect CNT structures onto metal substrates (Chapter 4).
- Methodology for characterizing electrical properties of VA-CNT structures (Chapter 4).
- Metal formation on CNT structures for increased electrical conduction (Chapter 5).
- Metal-CNT hybrid electrical probe design where VA-CNTs act as elastic springs and metal coating serves for improved electrical conduction (Chapter 5).
- Demonstration of first fully functional electromechanical probes made fully of CNTs (Chapter 5).
- Design guidelines for CNT probe design (Chapter 5).

## Chapter 2

# Carbon Nanotube Growth Methods and Column Manufacturing

This chapter describes and discusses CNT growth techniques employed in this thesis.

### 2.1 CNT Growth Techniques

Among various CNT growth techniques including arch discharge and laser ablation [2], chemical vapor deposition (CVD) technique is the most suitable method for scalable industrial applications where large number of CNT assemblies having micro to macro lengths is desirable. CVD techniques under the right conditions usually yield vertically aligned CNTs without external alignment efforts such as applied electric field during growth.

CVD growth technique can be divided into two main categories, namely fixed catalyst CVD and floating catalyst CVD. In the fixed catalyst CVD technique a thin film of catalyst layer [9, 10, 11, 12, 13], typically a transition metal, is deposited onto a support or buffer layer such as  $Al_2O_3$ . Both layers can be successively deposited with various techniques including evaporation or sputtering onto the growth substrate, typically silicon. In this method the carbon source is typically a hydrocarbon gas carried with an inert gas onto the growth substrate. The growth is typically conducted in a tube furnace heated up to 700 – 800°C range.

In the floating catalyst CVD technique, the catalyst particles are introduced in the gas phase instead of being deposited onto the growth substrate prior to the growth [14, 15, 16, 17,

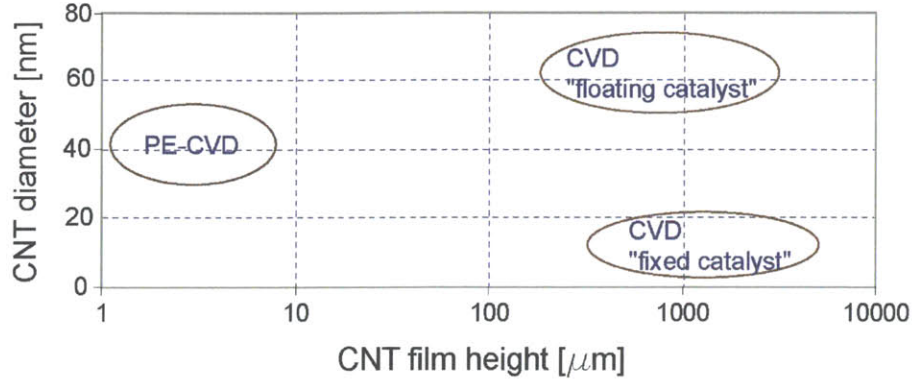


Figure 2-1: Comparison of growth techniques yielding VA-CNT films. For viable industrial applications, upper right corner is most desirable.

18, 19, 20, 21, 22, 23]. The carbon source is evaporated from the same solution containing the catalyst particles and carried along with the catalyst particles onto the growth surface, which is typically an oxide film. The growth is again conducted in a furnace at high temperature.

An additional variation of the CVD growth technique is the plasma enhanced CVD (PE-CVD) method, where growth is accomplished in a plasma environment [24, 25, 26, 27, 28, 29, 30]. Even though this technique yields very well aligned (due to the electric field) and large diameter CNTs, the film thickness is typically in the order of microns.

Figure 2-1 presents a comparison of scalable CVD growth techniques for micro/macro-scale applications. Due to their large film heights, fixed catalyst CVD and floating catalyst CVD methods are promising methods for scalable applications, and are explored throughout this thesis for the particular application in hand. The fixed catalyst method employed in this thesis is based on the method presented in [31], and the floating catalyst CVD growth is based on the method presented in [32].

## 2.2 Fixed Catalyst CVD Growth System

In this method, CNTs are grown from a catalyst layer of 1.2/10 nm  $Fe/Al_2O_3$  film deposited by e-beam evaporation on a silicon wafer and  $C_2H_4$  gas serves as the carbon source. The furnace schematics used for CNT growth with the fixed catalyst method is shown in Figure 2-2. The

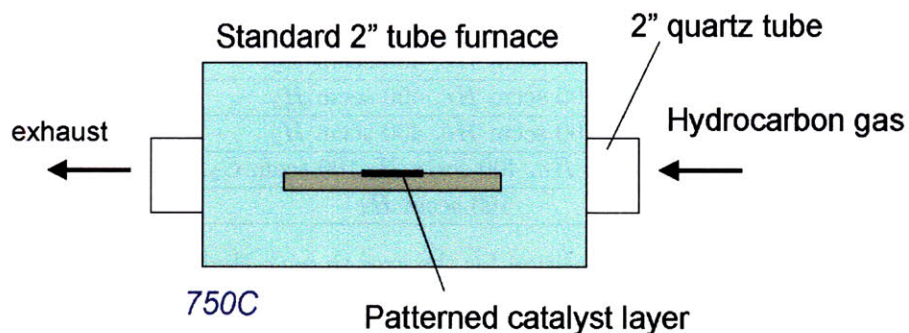


Figure 2-2: Schematics of the furnace used to grow vertically aligned carbon nanotube columns from "fixed catalyst".

| Time(min.)     | Gas Flow  | Temp ( $^{\circ}C$ ) |
|----------------|---|----------------------|
| 0-10           | 400 sccm <i>Ar</i>                                      | 0                    |
| 10-25          | 400 sccm <i>Ar</i>                                      | 0-750 (ramp)         |
| 25-35          | 400 sccm <i>Ar</i>                                      | 750                  |
| 35-40          | 400 sccm $H_2$ , 150 sccm <i>Ar</i>                     | 750                  |
| 40+growth time | 400 sccm $H_2$ , 150 sccm <i>Ar</i> , 100 sccm $C_2H_4$ | 750                  |
| ~30min         | 400 sccm <i>Ar</i>                                      | furnace off          |

Table 2.1: Process condition for the growth with Argon flush.

growth is performed in a quartz tube furnace (Lindberg) at atmospheric pressure. The furnace is ramped to the growth temperature of 750  $^{\circ}C$  under 400 sccm *Ar*; then 400/150 sccm  $H_2$ /*Ar* is introduced for 5 minute, then 100/400/150 sccm  $C_2H_4$ / $H_2$ /*Ar* is maintained for the typical growth period of 15 minutes. The details of the growth sequence is listed in Table 2.1.

The fixed catalyst growth technique used here yields base growth, where the catalyst particle remains on the growth substrate and addition of carbon results in lengthening of the CNTs attached to the catalyst particle. Figure 2-3 demonstrates the base growth mechanism. It should be emphasized that not all of the catalyst particles yield a CNT. In fact, only a small fraction of them yield CNTs. The catalyst particle formation during the ramp time and subsequent activity has direct consequences on the CNT diameter and areal density of CNTs. It was recently demonstrated that introduction of hydrogen into the furnace during certain periods of growth has significant effect on catalyst activity [33]. Growth conditions of another variation of the fixed catalyst recipe where hydrogen is supplied during the ramp time as well (instead

| Time(min.)     | Gas Flow  | Temp ( $^{\circ}C$ ) |
|----------------|---|----------------------|
| 0-10           | 100 sccm <i>He</i>                                      | 0                    |
| 10-20          | 100 sccm <i>He</i> , 400 sccm $H_2$                     | 0                    |
| 20-30          | 100 sccm <i>He</i> , 400 sccm $H_2$                     | 0-750 (ramp)         |
| 30-40          | 100 sccm <i>He</i> , 400 sccm $H_2$                     | 750                  |
| 40+growth time | 100 sccm <i>He</i> , 400 sccm $H_2$ , 100 sccm $C_2H_4$ | 750                  |
| ~30min         | 100 sccm <i>He</i>                                      | furnace off          |

Table 2.2: Process condition for the growth with Hydrogen flush..

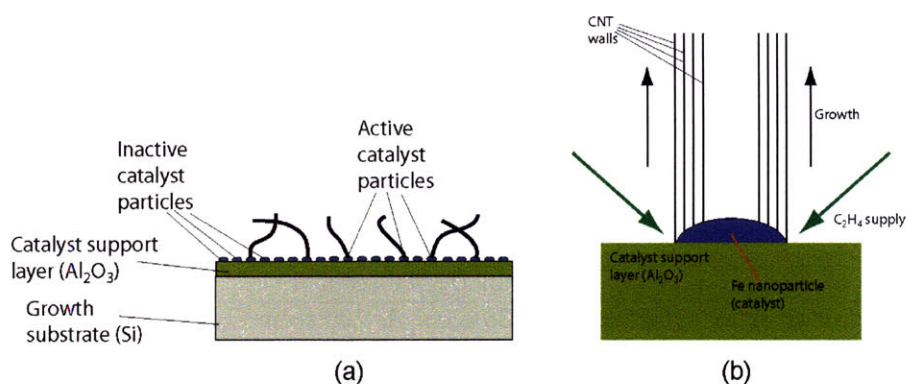


Figure 2-3: Initial stages of vertical growth with base growth. (a) Sketch depicting random initial growth direction and inactive catalyst particles which don't yield CNTs. (b) Schematics of base growth.

of only 5 minutes prior to growth) is summarized in Table 2.2.

Figure 2-4 presents the initial stages of the CNT growth. The catalyst particles which don't yield CNTs can be clearly seen in Figure 2-4 (d). It is also worthwhile to note that the CNTs are initially not aligned and grow in all directions forming CNT clusters. The growth then continues with the base growth mechanism. The formation of aligned CNT film is depicted in Figure 2-5. First, CNTs grow in all directions forming clusters. As the CNTs forming those clusters get longer and longer with the addition of new carbon atoms at the bottom where the reaction is catalyzed, the clustered layer gets lifted, resulting in guided growth of the CNTs. Basically, after a certain point, the CNTs have no where else to go other than growing upwards.

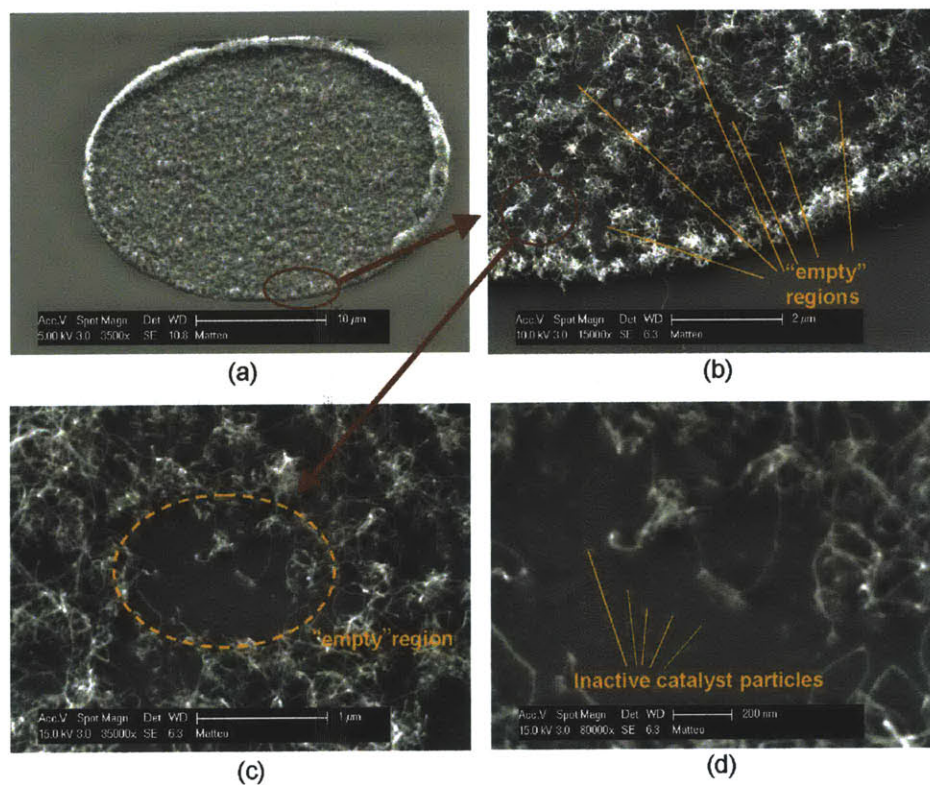


Figure 2-4: Initial stages of growth with the base growth mechanism obtained with the fixed catalyst CVD method. (a) Circular pattern. (b) Close-up image of a corner of transition between patterned layer and the support layer where no CNT growth occurs. Empty spots, due to inactive catalyst particles, can be seen. (c, d) Close up images of the empty spots showing the inactive catalyst particles and tangled CNT film formation from the neighbouring catalyst particles.

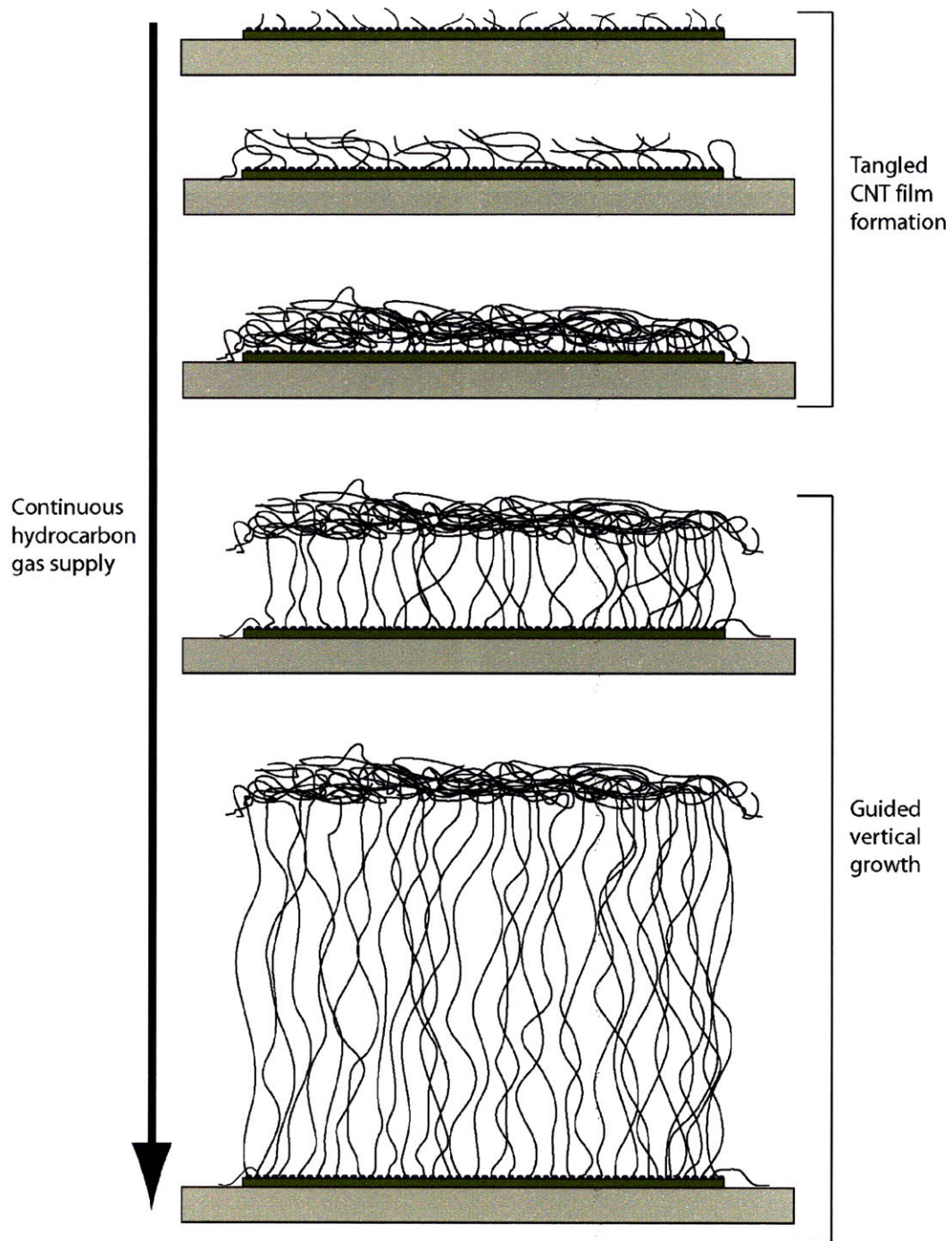


Figure 2-5: Sketch demonstrating vertical growth of CNTs and formation of forests.



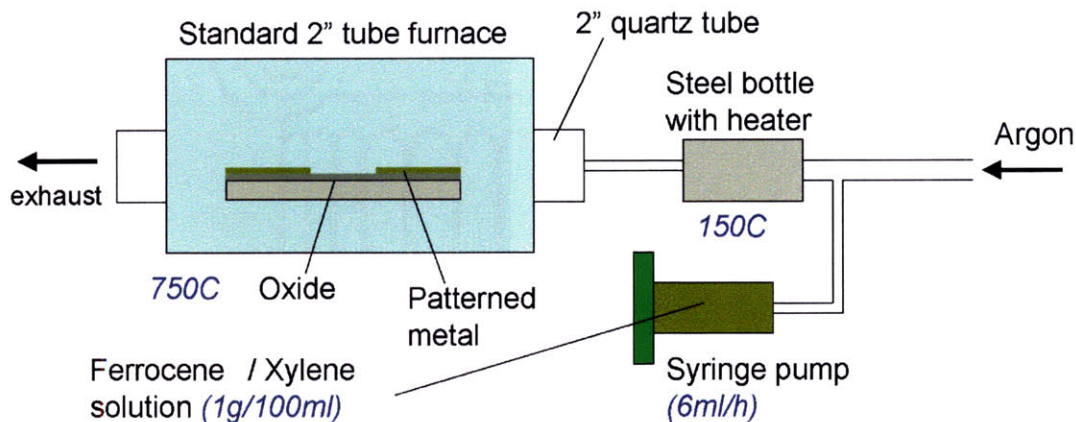


Figure 2-6: Schematics of the furnace used to grow vertically aligned carbon nanotube films from floating catalyst.

|                           |          |
|---------------------------|----------|
| Ferrocene/Xylene solution | 1g/100ml |
| Syringe pump rate         | 6ml/h    |
| Steel bottle temperature  | 150°C    |
| Tube furnace temperature  | 750°C    |

Table 2.3: Process conditions for CVD growth with floating catalyst.

## 2.3 Floating catalyst CVD Growth System

The furnace schematics used for CNT growth with the floating catalyst method is shown in Figure 2-6. The carbon source (xylene) and the catalyst particles (Ferrocene- $Fe(C_5H_5)_2$ ) are contained in a solution and pumped through a syringe pump into a heated steel bottle where they evaporate and get carried into the furnace with Argon gas as carrier gas. Important process parameters are listed in Table 2.3.

A significant difference between the floating catalyst and fixed catalyst method is that during the floating catalyst CVD growth the catalyst particles constantly rain onto the CNTs and the catalyst particles can be found throughout the length of a CNT. Figure 2-7a shows a close up SEM image of the CNTs grown with this technique. Figure 2-7 is an SEM image taken in back-scattered mode showing catalyst particles along the length of the CNTs. CNT films grown with the floating catalyst grow in a similar fashion vertically upward and yield aligned CNTs.

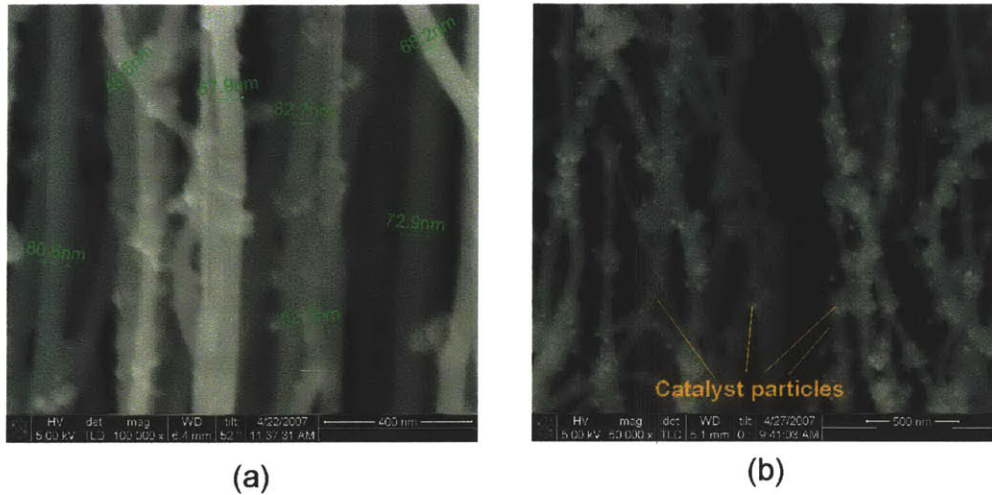


Figure 2-7: Close-up images of a column side wall grown with floating catalyst CVD. (a) CNT diameter measurements in SEM. (b) SEM image taken with back scattered electrons showing the bright iron nanoparticles acting as catalyst during the growth.

## 2.4 Comparison of CVD Methods

As discussed earlier, various CVD methods yield different inherent CNT film properties such as CNT diameter and CNT density. These are very important attributes of the CNT structures, and as will be shown in Chapter 3, they have very significant implications on the mechanical properties of CNT structures resulting from these methods. Close up SEM images of CNTs resulting from the CVD techniques employed in this thesis are shown in Figure 2-8. At a first glance, a significant density increase is noticed from the fixed catalyst growth without hydrogen to the fixed catalyst growth with hydrogen. This is attributed to the higher catalyst activity provided by the hydrogen gas. Another noticeable difference is the significant increase in CNT diameter from the fixed catalyst recipe to the floating catalyst recipe.

To get a better understanding of the CNT structures and obtain measurements of the inherent properties of CNTs, the films are analyzed with transmission electron microscope (TEM). Figure 2-9 shows TEM images of CNTs grown with fixed catalyst recipe (argon flush). First, the CNT film to be measured is dispersed in a isopropanol bath and sonicated to separate CNTs from one another. Then the TEM grid is dipped into this solution with a tweezer and

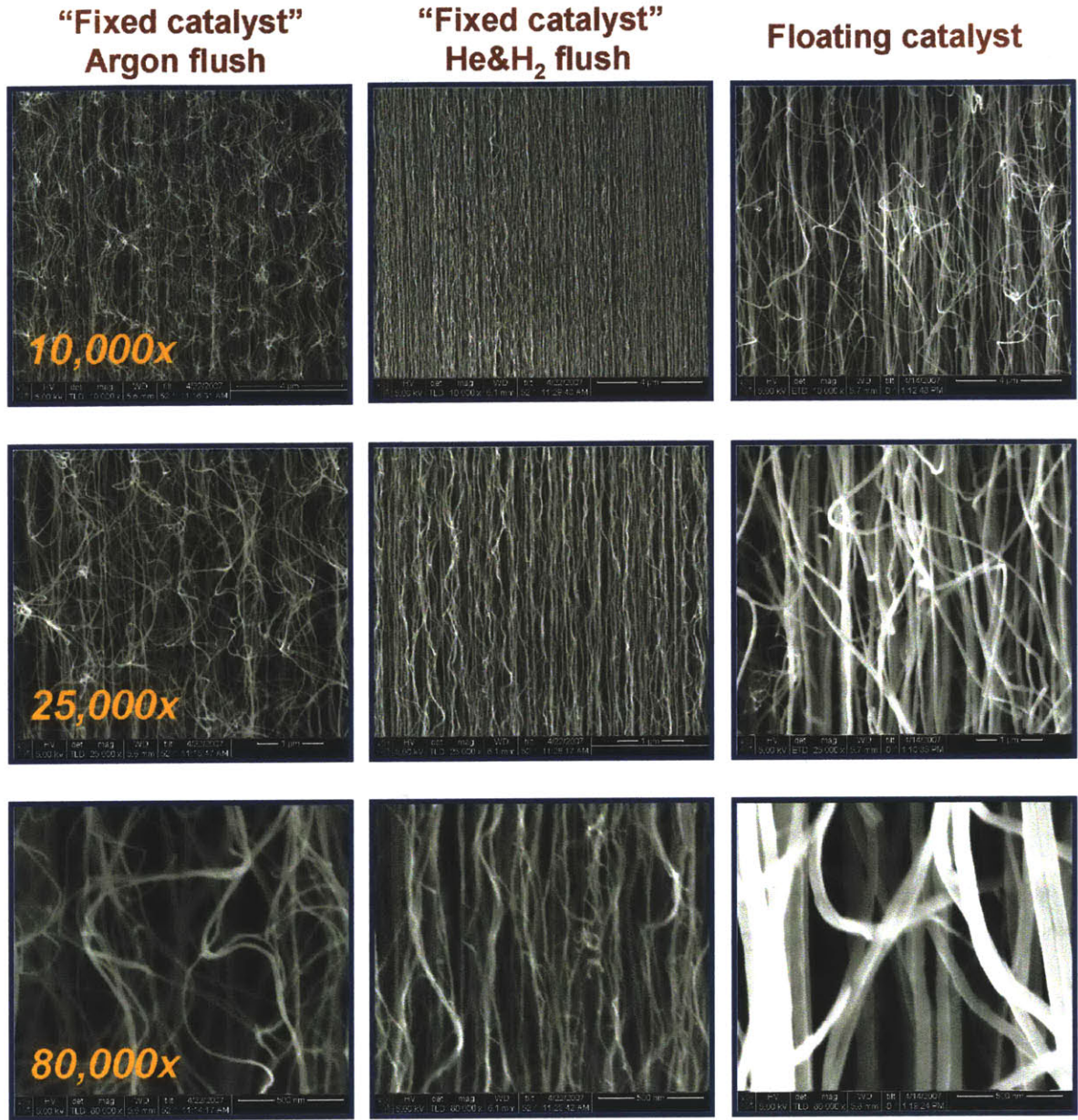


Figure 2-8: SEM images at increasing magnification of CNT column sidewalls grown with different CVD processes.

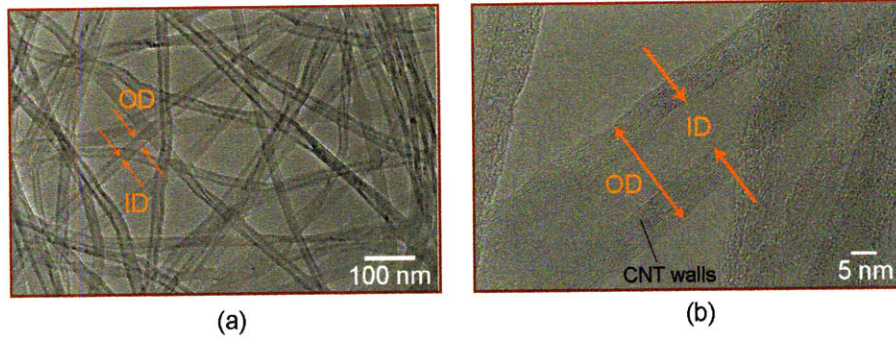


Figure 2-9: (a) Typical TEM image used to measure outer diameter and inner diameter of CNTs. (b) A close up image of a CNT. Both pictures correspond to CNTs grown with argon flush.

swept until some CNTs are captured onto the surfaces. After an image like 2-9 (a) is obtained, the outer and inner diameters of CNTs are measured with a microscopy software.

The density of CNT structures are calculated by measuring the mass of a continuous CNT film with a sensitive balance, and then dividing the mass by the volume of the CNT film. The volume fraction of the CNTs is calculated by dividing this density by the density of the graphite ( $2.2\text{kg}/\text{m}^3$ ). The volume fraction of the CNTs can be also expressed as the area ratio of CNTs to the film area, as shown in Figure 2-10 which depicts a unit area containing one CNT and average CNT-CNT spacing  $a$  :

$$V_f = \frac{A_{CNT}}{A_{total}} = \frac{(OD^2 - ID^2)\pi}{4a^2} \quad (2.1)$$

where  $V_f$  is the volume fraction,  $OD$  and  $ID$  are average outer and inner diameters measured by TEM, and  $a$  is average CNT-CNT spacing in the film. Using the measured values with TEM and the sensitive balance, average CNT-CNT spacing is calculated using equation 2.1. Table 2.4 summarizes TEM measurement results and related calculations.

## 2.5 Fabrication of CNT Columns

The ability to grow CNT films into desired shapes is very important for applications such as electromechanical probes. The nature of the growth mechanism discussed earlier should allow vertical growth from small areas of catalytic activity mainly due to the fact that CNT

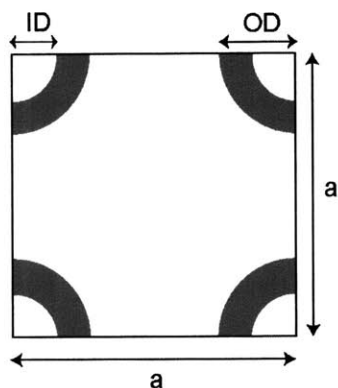


Figure 2-10: Unit CNT film area used to calculate average CNT-CNT spacing.

| CNT growth recipe                 | Fixed catalyst<br>Argon flush | Fixed catalyst<br>Hydrogen flush | Floating catalyst  |
|-----------------------------------|-------------------------------|----------------------------------|--------------------|
| Structural Density ( $kg/m^3$ )   | 8                             | 15                               | 200                |
| Volume Fraction of CNTs           | 0.36 %                        | 0.68 %                           | 9.09 %             |
| Structural Porosity               | 99.64 %                       | 99.32 %                          | 90.91 %            |
| CNT Outer Diameter (nm)           | 25.8                          | 8.1                              | 89.9               |
| CNT Inner Diameter (nm)           | 11.1                          | 4.3                              | 15.1               |
| Average Number of Walls           | 21.7                          | 5.6                              | 110                |
| Average CNT-CNT Spacing (nm)      | 342                           | 74                               | 260                |
| CNT Areal Density (CNTs/ $cm^2$ ) | $8.54 \times 10^8$            | $1.84 \times 10^{10}$            | $1.47 \times 10^9$ |

Table 2.4: Comparison of resulting CNT properties from different recipes.

|    |  |
|----|--|
| 1) | Clean Acetone-IPA-DI water   |
| 2) | HMDS   |
| 3) | Spin coat photoresist - AZ 5214E: 10s dispense @ 1rpm, then 30s @1500rpm |
| 4) | Pre bake : 90C 1min. (hot plate)   |
| 5) | Exposure : 3s (hard pressure contact)                                    |
| 6) | Post bake : 115C, 1min (hot plate)                                       |
| 7) | Flood exposure : 2min (one exposure)                                     |
| 8) | Develop : AZ400K(1:4), 90s   |
| 9) | Wet transfer and hard rinse with water                                   |

Table 2.5: Image reversal process used to lift-off metal layer (Fe for fixed catalyst growth and Au for floating catalyst growth) for desired pattern and column shape.

dimensions are much smaller than the pattern sizes. For the case of fixed catalyst method, shape control is achieved by patterning the catalyst layer from which CNTs grow. Similarly, for the case of floating catalyst growth, the area of the oxide layer is controlled by patterning a metal layer deposited earlier onto the oxide surface.

For both growth techniques, patterning is achieved using the lift-off process summarized in Table 2.5 based on an image reversal photoresist. After the lithography step, the metal layer to be patterned ( $Fe/Al_2O_3$  for fixed catalyst and Au for floating catalyst method) is deposited onto the photoresist and then lifted off in acetone. It is worthwhile to mention that if the patterning of the Fe layer requires a dark field mask, the patterning of the Au will require a bright field mask, or vice versa, for the same geometric patterns

Figure 2-11 shows high pitch square and circular CNT columns grown with the fixed catalyst CVD method from patterned catalyst layer. This demonstrates the ability to control shape and pitch very accurately with this method. Similarly, shape control can be achieved with the floating catalyst CVD technique. Figures 2-12 and 2-13 show various examples.

This chapter provided discussions and details of CVD recipes employed in this thesis, namely fixed catalyst CVD, fixed catalyst CVD with hydrogen preconditioning of the catalyst layer, and floating catalyst CVD. Characteristics of the CNT structures, such as CNT diameter, CNT aerial density, and structural porosity, resulting from each growth technique were discussed. This chapter also presented techniques to fabricate CNT columns with desired shapes by lithography techniques. The implications of the inherent properties of the CNT structures on the mechanical properties will be discussed in the next chapter.

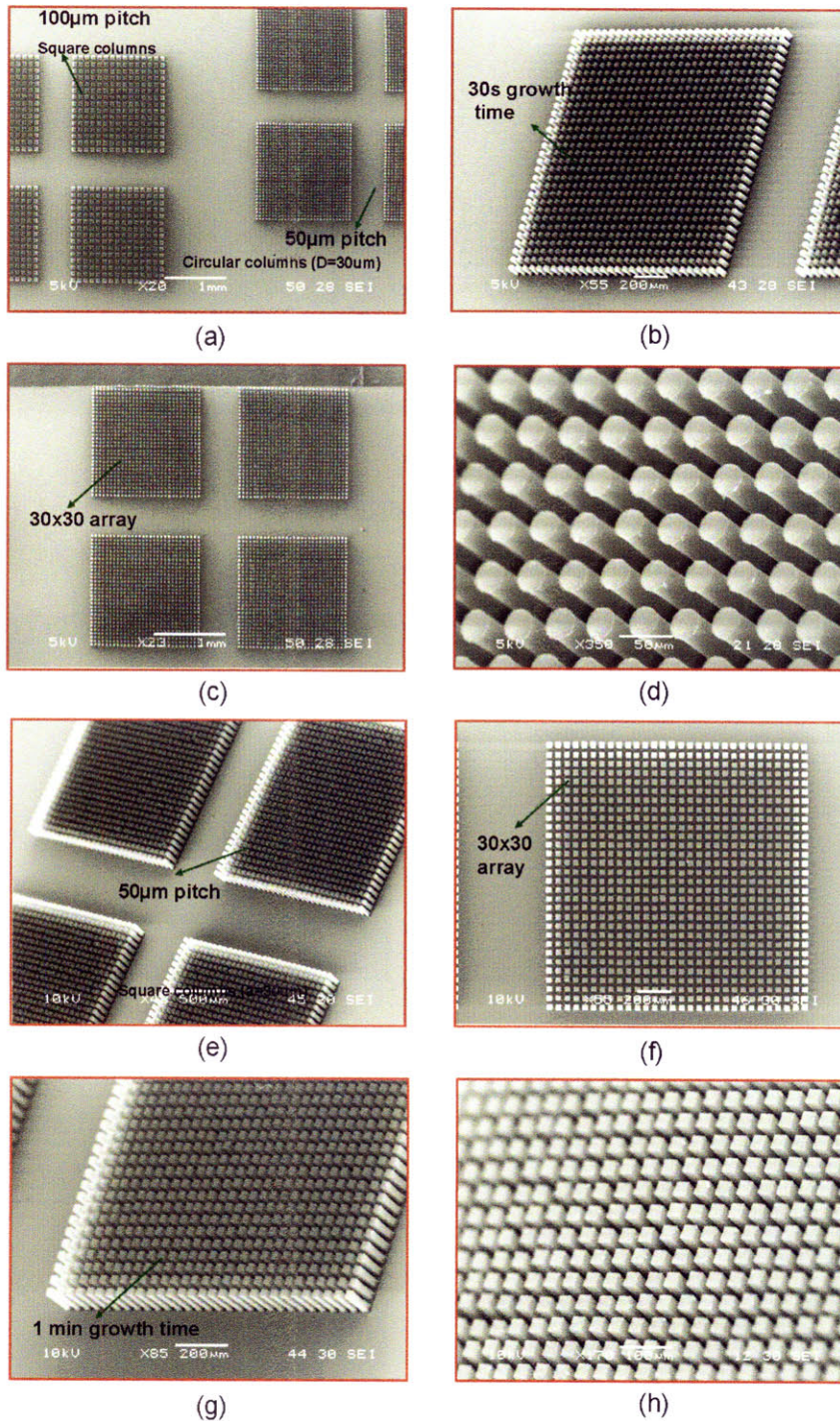


Figure 2-11: CNT columns grown with fixed catalyst CVD method (hydrogen flush). Pitch, shape and height of the columns can be easily controlled by patterning and by growth time respectively.

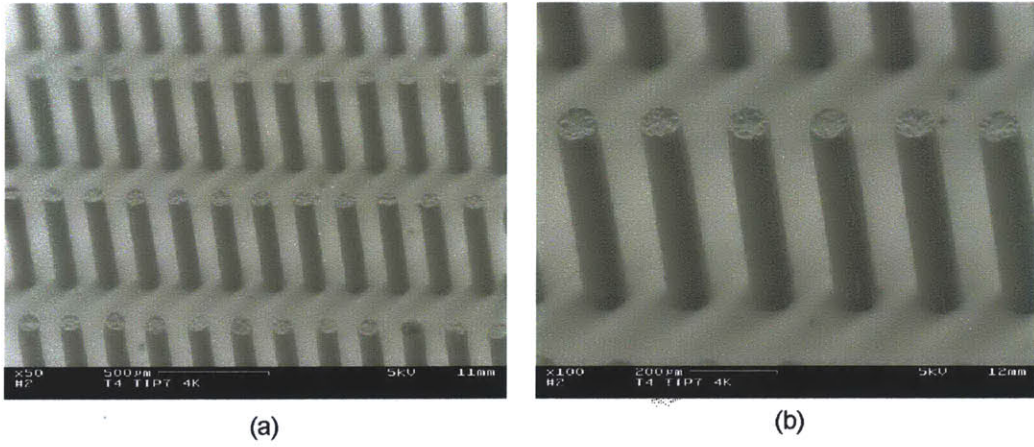


Figure 2-12: Columns grown with floating catalyst CVD method.

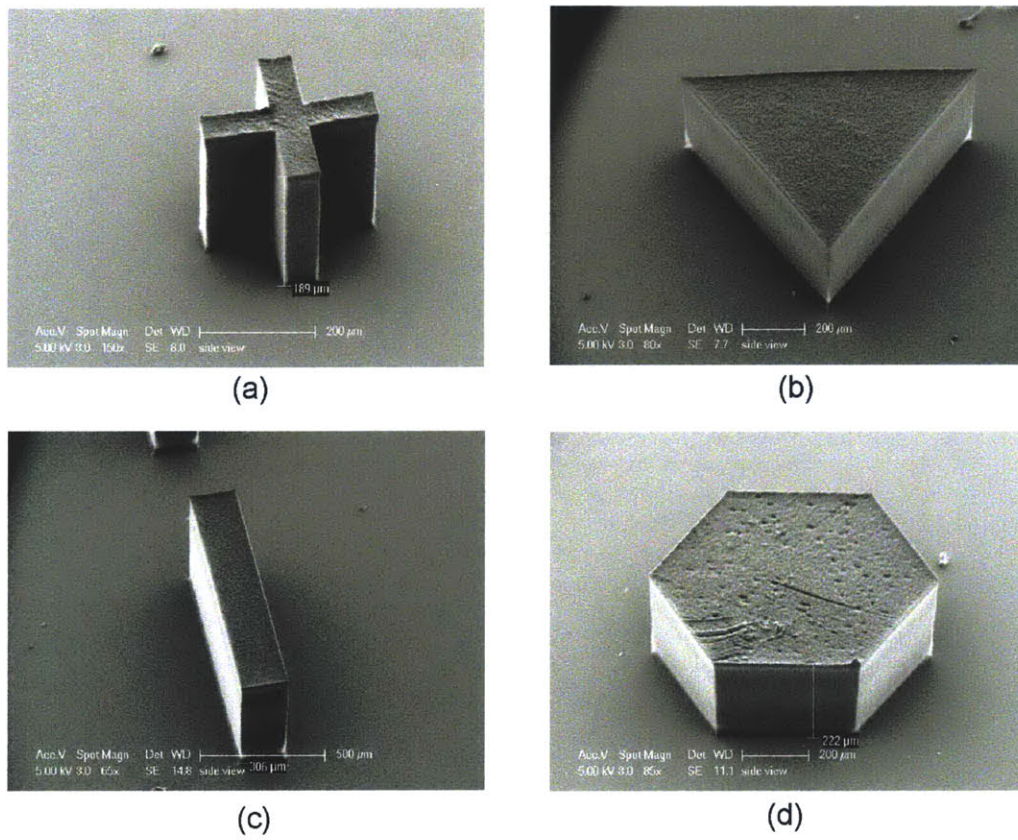


Figure 2-13: Columns of different shapes grown with floating catalyst CVD method.



## **Chapter 3**

# **Mechanical Characterization of Vertically Aligned Carbon Nanotube Structures**

This chapter presents a comprehensive study of the mechanical properties of VA-CNT structures. CNT structures grown using the growth techniques discussed in Chapter 2 are characterized and resulting mechanical properties are compared. Deformation models to explain the mechanical behavior of CNT structures are discussed.

### **3.1 Experimental Setup and Testing Issues**

Mechanical characterization of CNT structures is performed with a CETR Micro Tribometer ([www.cetr.com](http://www.cetr.com)) as well as in situ SEM with a probe inserted through a feed-through in the SEM chamber ([www.omniprobe.com](http://www.omniprobe.com)). The tribometer, which allows simultaneous measurement of applied force, displacement and time, is used for detailed testing and characterization whereas in-situ SEM probe is used to observe the CNT structures during compression, record videos and to get insight into the deformation mechanism.

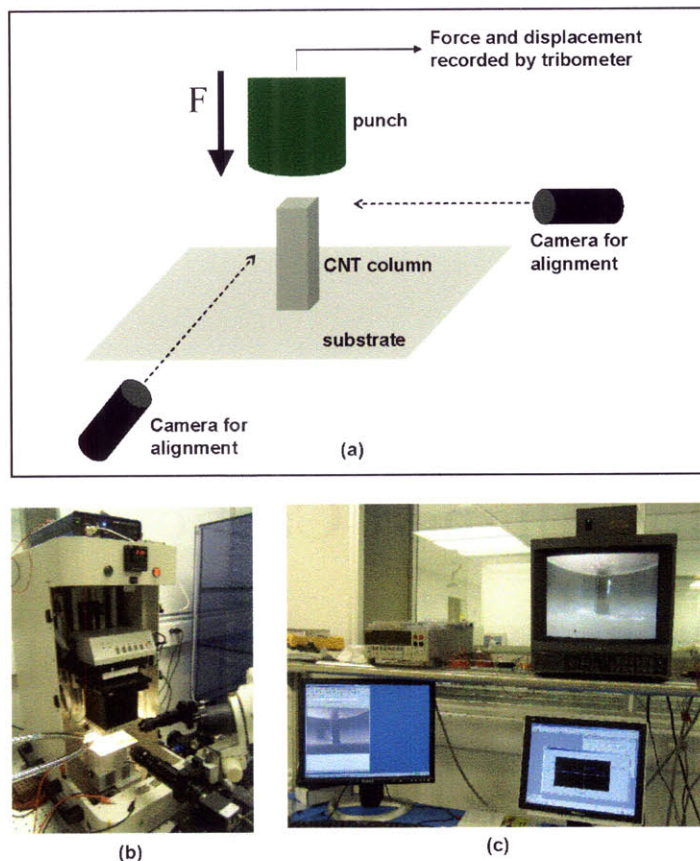


Figure 3-1: (a) Schematics of the experimental setup. As the punch, a 1.6 mm diameter brass rod is used. (b) Photograph of the tribometer used for mechanical characterization. (c) In-situ monitoring of CNT columns during compression with 2 perpendicular cameras. (courtesy of FormFactor, Inc.)

### 3.1.1 Tribometer

The experimental setup is shown in Figure 3-1, where CNT columns are compressed parallel to the CNT alignment direction. In all of the tests, the displacement is imposed at a constant rate of  $10\mu/s$  and force is measured using a load sensor suited to the stiffness of the structure under the test. For softer CNT structures, as is the case with the columns resulting from the fixed catalyst CVD growth, a load sensor with a maximum range of 50g and a resolution of 50mg (0.5mN) is used, whereas for harder CNT structures resulting from the floating catalyst CVD growth, a 500g load sensor with a resolution of 0.5g (5mN) is used.

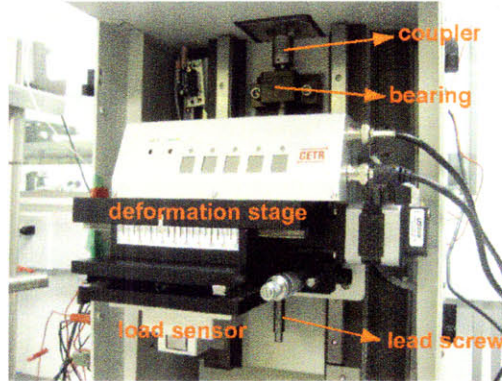


Figure 3-2: Components of the tribometer: The load sensor attached to the deformation stage which moves vertically through a leadscrew assembly. (courtesy of FormFactor, Inc.)

As both load sensors used are cantilever based detectors (strain gauges), it is important to take the stiffness of the load sensor into account when calculating the stiffness of the structure under test. This becomes especially very important when the stiffness of the structure under test is comparable to the stiffness of the sensor, which is the case for the tests performed with the 50g sensor. Since the structure and the load sensor act as springs in series, the stiffness of a CNT column,  $k_c$ , can be calculated as:

$$k_c = \frac{k_s k_m}{k_s + k_m} \quad (3.1)$$

where  $k_s$  and  $k_m$  are the stiffness of the load sensor and the measured stiffness respectively.

Another important issue is the backlash in the leadscrew moving the deformation stage in the tribometer assembly, shown in Figure 3-2. The backlash is particularly important when one needs to perform cyclic testing. An example case is illustrated in Figure 3-3 for a leadscrew with a backlash of  $10\mu m$ . If the experiment is adjusted such that at  $z = 0$  the punch and sample are in contact, at the end of the first cycle, the sample is already compressed  $10\mu m$ , and the force reading is positive. This is misleading and shows as if the sample is pushing back, or getting longer or stronger, which is in fact an artifact of the backlash. If the imposed deformation is  $10\mu m$  or less, the deformation stage would not move at all. It is also important to note that the amount of backlash might vary along the length of the leadscrew. For the

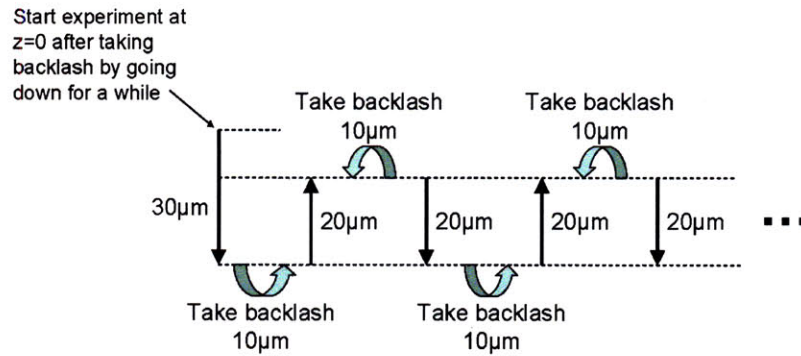


Figure 3-3: Sketch depicting the backlash issue for 10µm backlash, which makes it impossible to characterize columns at deformations near or smaller than 10µm.

purposes of the current characterization work, this backlash didn't pose significant problem as all the deformations imposed during testing are larger than 50µm and backlash was around 5µm for the section of the leadscrew used during the experiments.

### 3.1.2 In-Situ SEM Compression

The in-situ compression tests are performed with a FEI dual beam system with an integrated OmniProbe. The particular model used is an earlier version and has manual controls. The in-situ probe doesn't have force or displacement sending capabilities and it was used to observe CNT structures deform during compression and gain insight into the deformation mechanism. The probe used to compress CNT structures is shown in Figure 3-4.

An important issue is the lateral stiffness of the probe for the experiments performed, as will be discussed in later sections of this chapter. The system used for in-situ SEM characterization has a long probe reaching from the tip of the probe assembly to the top surface of the CNT column. For the tests performed, it is very critical that the probe contacts the top surface of the CNT column perfectly parallel, as well as it is very rigid in lateral directions. As the probe assembly is mounted through a feed-through on the SEM chamber, attention needs to be paid so that the sample holder and the probe are perpendicular. If this is not the case, the effect of lateral compliance becomes more prominent. In the case of tribometer, lateral stiffness is not an issue.

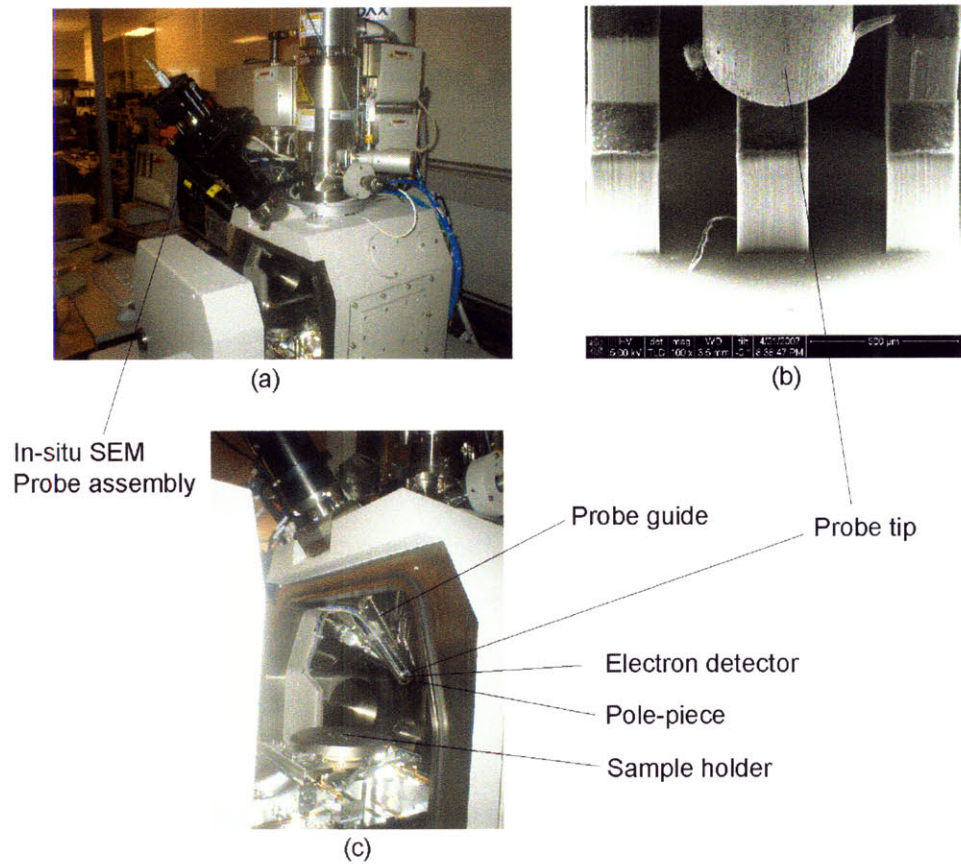


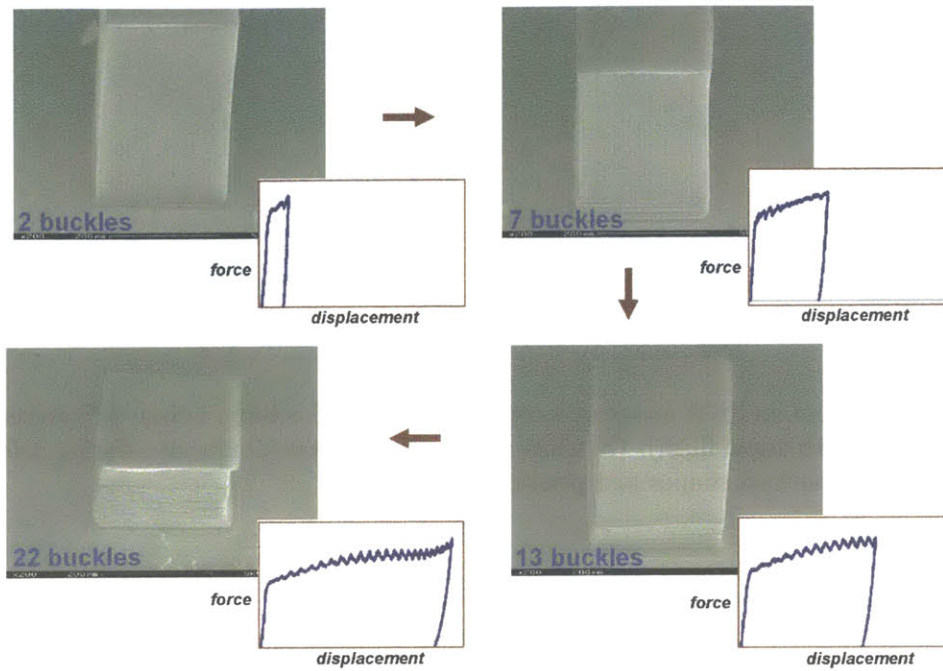
Figure 3-4: (a,c) Components of the in-situ SEM probing system. (b) SEM image of the probe inside the SEM chamber used to compress CNT structures for in-situ characterization. (courtesy of FormFactor, Inc.)

## 3.2 Deformation Mechanism of CNT Columns Grown with Fixed Catalyst CVD

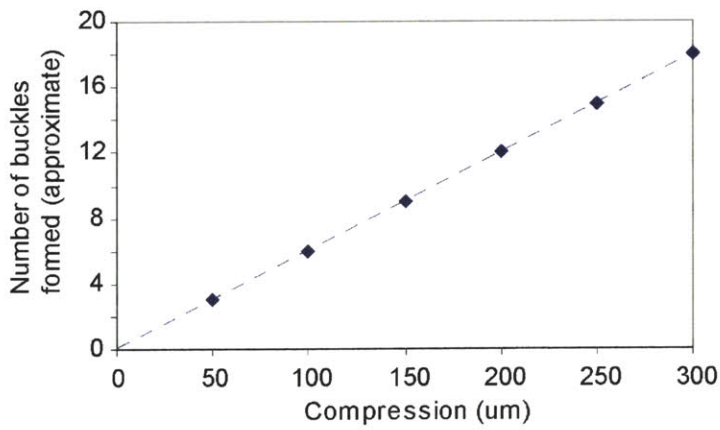
### 3.2.1 Initial Observations

For the case of fixed catalyst growth, the most important initial observation about the deformation of VA-CNT structures is that beyond a certain strain value, the structures start buckling in a consecutive manner, and the buckles keep forming until the compression stops, or all of the structure is consumed and converted into ripples. This buckle formation is very regular and repeatable, provided that the probe and the CNT column are perfectly parallel, lateral stiffness of the probe is very high, and the compression speed is low ( $\sim 10\mu\text{m}/\text{s}$ ). Successive buckle formation is depicted in Figure 3-5 where identical CNT columns are compressed to different strain values. Another important observation is that number of ripples in the test data, namely force vs. vertical deformation, is the same as number of buckles. This indicates that during buckle formation, the force drops rapidly and increases again during the compression of the buckles already formed until another buckle is formed. This process continuous until the compression is stopped. Upon the release of the force completely, the CNT columns remain roughly at the same height they were compressed to, except a short recovery length. In other words, the deformation results in very large plastic deformation. It is also worthwhile to note that the number of buckles is proportional to the imposed deformation on the column, which is depicted in Figure 3-5 c.

This localized, and plastic buckle formation mechanism is most pronounced for the columns grown with the fixed catalyst CVD method with Argon flush (hydrogen introduced only shortly before growth) where the buckle formation is easily observable optically with the cameras shown in Figure 3-1. It can be also easily detected by the load sensor and the buckle formation is recorded as ripples. Figure 3-6 shows the wall of a CNT column before and after buckle formation. For the case of CNT columns grown with the fixed catalyst CVD method with hydrogen flush, the deformation mechanism, namely large plastic deformation and buckle formation, is the same, but the detection of the buckle formation during the test is not as pronounced as the CNTs grown with argon flush. Also the average length of the buckles is shorter, as shown in Figure 3-9 which compares the resulting buckles on a column grown with fixed catalyst CVD



(a)



(b)

Figure 3-5: (a) Successive buckle formation: number of buckles is the same as number of the ripples observed during testing, indicating that each ripple corresponds to a buckle formation. (b) Number of buckles is proportional to the imposed deformation.

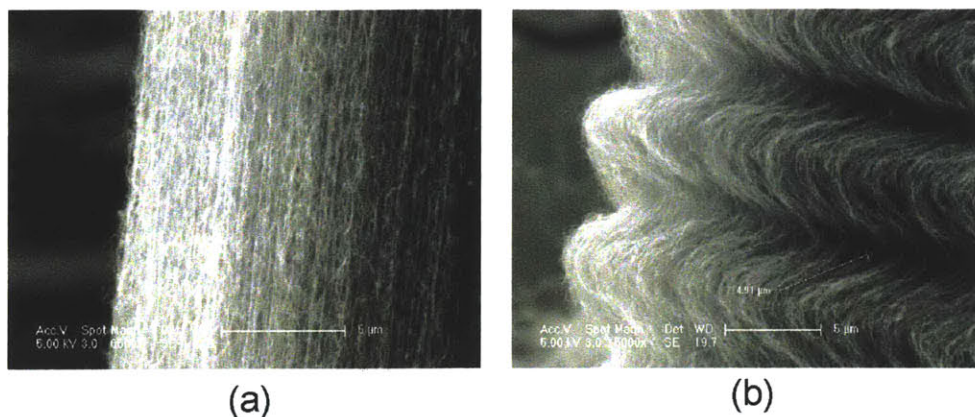


Figure 3-6: (a) Close up SEM image of a corner from a CNT column before deformation (fixed catalyst growth with argon flush). (b) Close up image of the buckles formed during deformation depicting regular buckled shapes and plastic deformation.

with argon flush with buckles on a column grown by fixed catalyst CVD with hydrogen flush.

Buckles start forming mostly at the bottom of the column, but buckles starting to form at the top, namely where the column contacts the punch, have also been observed rarely as shown in Figure 3-7. This suggests that the buckles start forming at macro-scale imperfections, and the bottom portion of the column, where the CNT's initiate from the patterned catalyst layer, has the greatest likelihood for buckle initiation.

Another interesting observation is that upon compression, columns of various sizes and shapes including circular, triangular, hexagonal and cross-shaped ones, form similar size and shape buckles formed by columns with square cross-section, as shown in Figure 3-8. This indicates that the buckle formation process is independent of size and shape of the column. In other words, the buckle formation is not geometry dependent and is an inherent property of the CNTs the structure is made of, which can be observed in Figure 3-9. Another observation is that the buckles resulting from the hydrogen flush aren't as "pretty" as the ones resulting from argon flush, and number of buckles are approximately are 12 buckles per 100 μm deformation (6 buckles/100 μm without hydrogen).



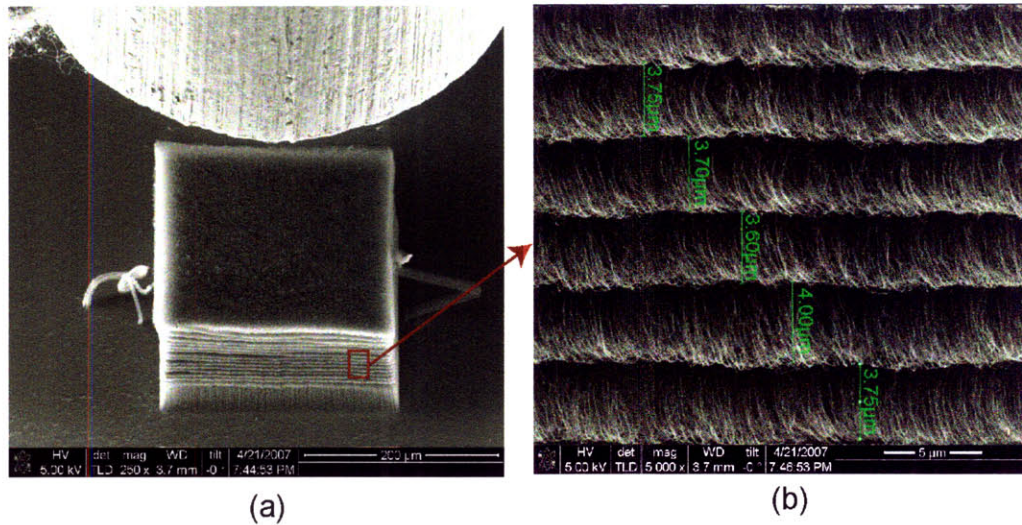
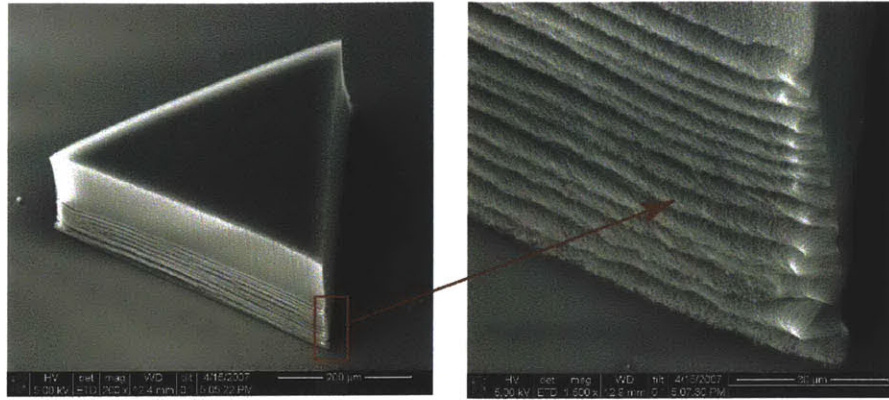


Figure 3-7: (a) SEM image of a column and probe after compression showing buckle formation at the top portion where the probe and column touch. (b) Regular buckle patterns formed at the top portion having identical patterns as buckles form at the bottom section.

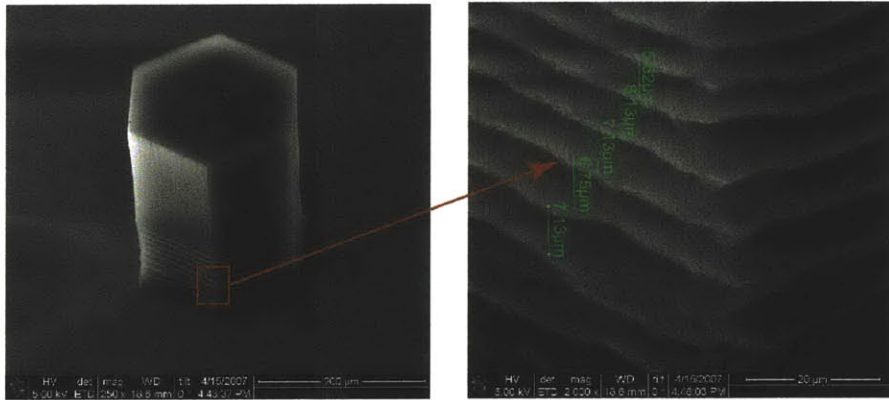
### 3.2.2 In-situ SEM Compression

To get more insight into the deformation mechanism of CNT structures, in-situ SEM compression tests are performed and videos are recorded. Snapshot pictures from the recordings of the videos are presented in this section. First a CNT column under compression is observed while successive buckles form, which is shown in Figure 3-10. While the buckles form in a continuous manner, it has been often observed that the top portion of the column swings like a "belly dancer" where the structures rotates very slightly around the center of the column either clockwise or counterclockwise.

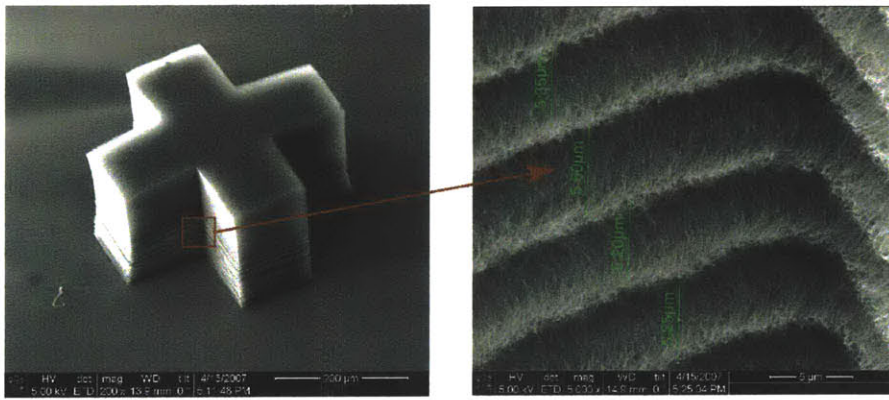
Then the corner of a CNT column is observed during buckle formation and subsequent relaxation where the probe compressing the column is retracted slowly. Snapshot pictures of this experiment is shown in Figure 3-11. After the formation of the buckles, when the probe starts retracting, the existing buckles start expanding, which results in an overall elastic recovery of the structure, which can be easily observed in Figure 3-11. Beyond a certain point, the buckles stop expanding and the test results in a large plastic deformation. However, if the column is compressed again, the buckles shrink and if the compression stops before forming a



(a)



(b)



(c)

Figure 3-8: CNT columns of various shapes forming similar buckles upon compression (fixed catalyst growth with Argon flush). (a) Triangular column. (b) Hexagonal column. (c) Cross shaped column.

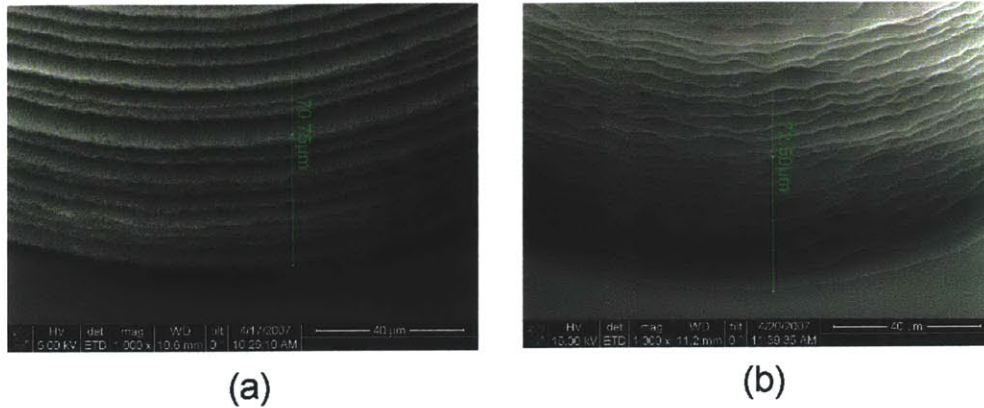


Figure 3-9: Shape and size of the buckles formed are inherent properties of the CNTs the columns are made of. Bottom sections of circular columns grown by fixed catalyst CVD with (a) argon flush and (b) helium and hydrogen flush after deformation.

new buckle, the same elastic recovery can be achieved. This is an important observation as it demonstrates that after large plastic deformation, there is some elastic recovery, which can be indeed used as a spring mechanism, which will be discussed later in this chapter.

To obtain further insight into the post-buckling elastic behavior, in other words, to better understand the expansion and contraction of the individual buckles after they form, a column already compressed to form buckles is tested in-situ SEM in its elastic range, that is the column is compressed and released without exceeding the elastic limit so that no additional buckles are formed, and individual buckles are observed. Figure 3-12 shows snapshots from the experiment. It can be seen that individual buckles "breathe" like a bellow, or an accordion, elastically. Figure 3-12 b shows close-up snapshots during test where it can be easily seen that the buckle shrinks upon compression. The position of the buckle changes because the buckles below shrink as well, and the length of the column becomes shorter. As the electron beam monitoring the column is stationary, the shrinking buckle move downwards relative to the electron beam.

### 3.2.3 Detailed Testing with Tribometer

After the initial observations and in-situ SEM investigations, to better understand the deformation of CNT structures, the columns are tested systematically with the tribometer using the

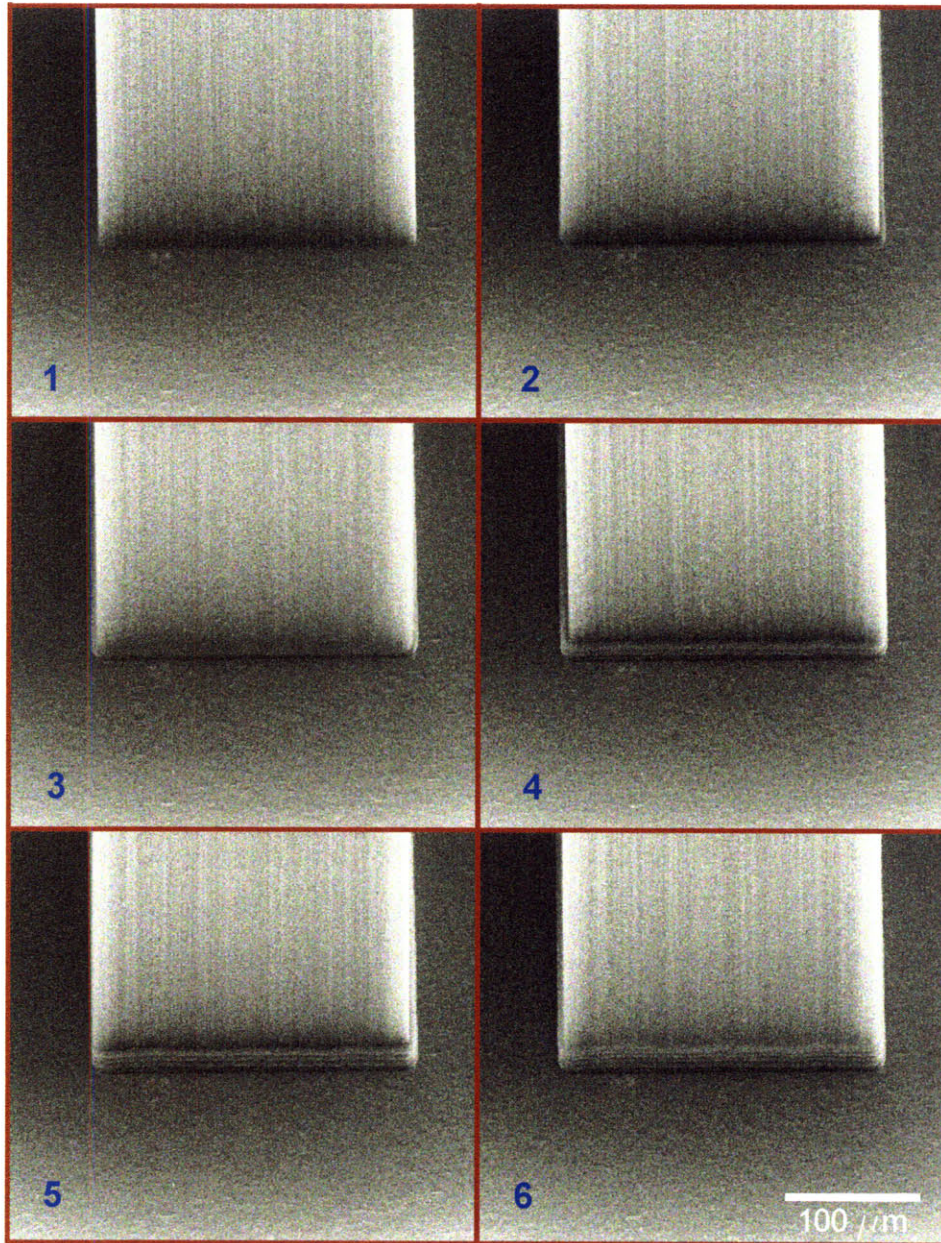


Figure 3-10: Successive buckle formation of CNT column unde compression. Images are taken during in-situ SEM compression test.

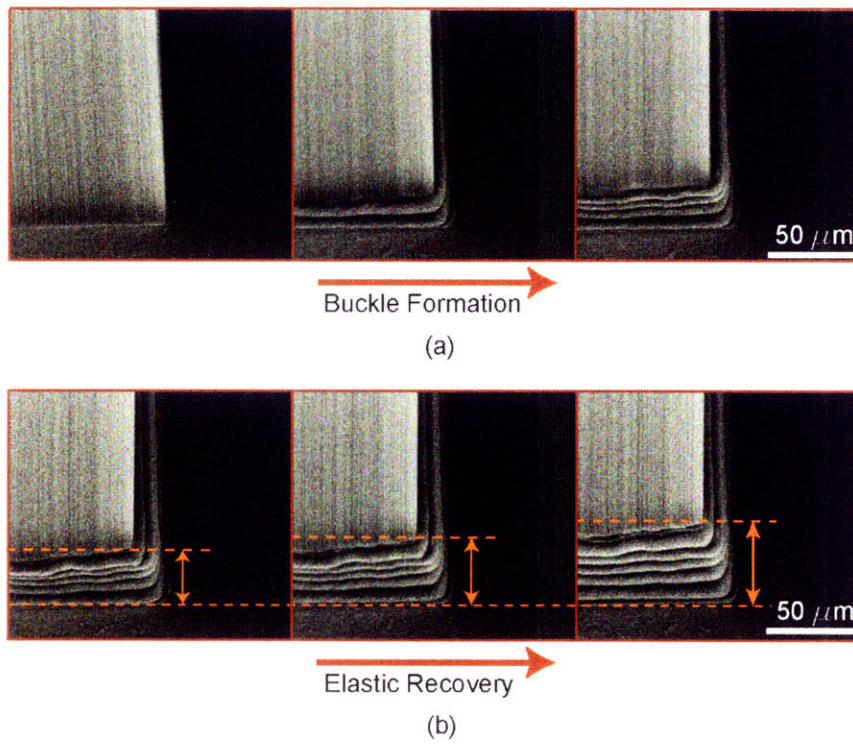


Figure 3-11: (a) In-situ SEM buckle formation test. (b) Elastic recovery during release of the probe.

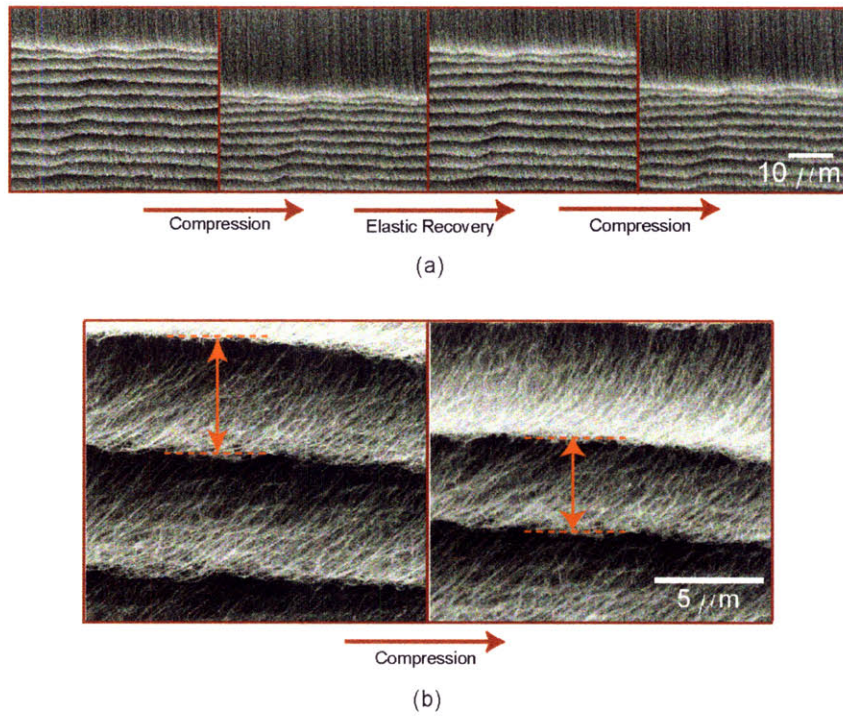


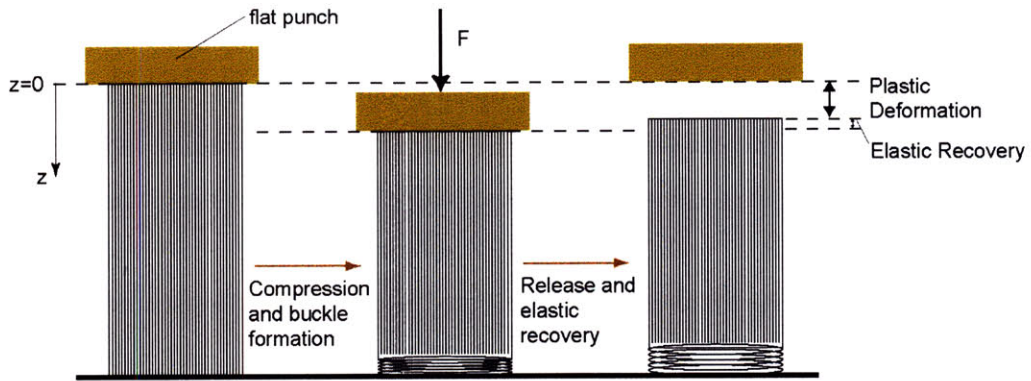
Figure 3-12: (a) Breathing bellow-like buckles during testing. This elastic range can be used as a spring for various applications. (b) Close-up snapshots of a buckle before and after compression showing individual buckles shrink and expand during testing.

procedure described in Figure 3-13. First, the punch is brought down until it comes into contact with the CNT column where alignment of the punch with the column is done by observing live images provided by the two perpendicular cameras shown in Figure 3-1. This position is marked as  $z = 0$  and during the remaining of the test, all the deformations, including plastic deformations are defined with respect to this starting point. The column is first compressed by a pre-determined amount, typically  $50\mu m$ , and then released where the punch is brought back to  $z = 0$ . This compression routine is repeated by increasing the compression amount incrementally, typically by  $50\mu m$  each cycle. Figure 3-13 depicts a three cycle compression test.

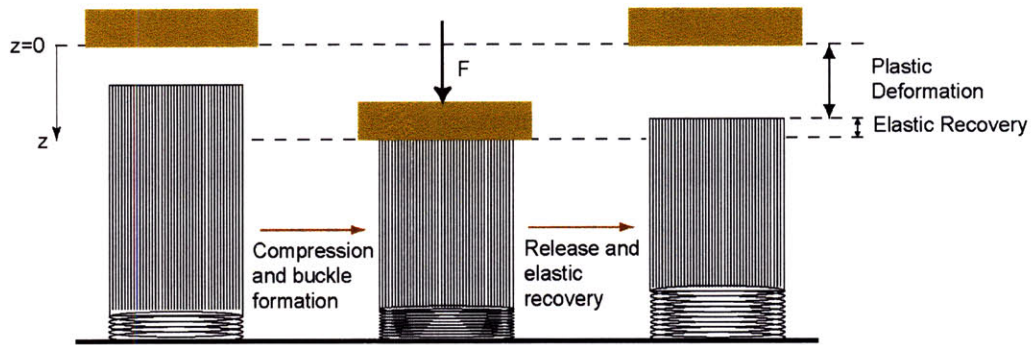
Typical vertical force vs. deformation curves are shown in Figure 3-14. The first cycle starts with an elastic compression. After a certain force is reached, the column starts collapsing and forms successive buckles until the compression stops. During the release of the punch, the column recovers some of the compressed length elastically, but this a small fraction of the overall deformation. In other words, the compression and buckle formation results in large plastic deformation. The second cycle starts with an elastic compression, this time with the same stiffness as the stiffness observed during the elastic recovery of the first cycle. This is followed by successive buckle formations and again an elastic release. The third cycle starts with an elastic compression with the same stiffness observed during the elastic recovery of the second cycle and the test continuous until the desired number of incremental compressions is reached.

At any time during this procedure, the elastic portion of the structure can be utilized as a spring, where the whole buckled portion behaves similar to an accordion. As discussed earlier, in-situ SEM compression tests revealed that during the elastic recovery and small deflection spring operation, the previous formed buckles "breathe". In other words, their wavelength becomes shorter as they get compressed, and longer as the structure is released.

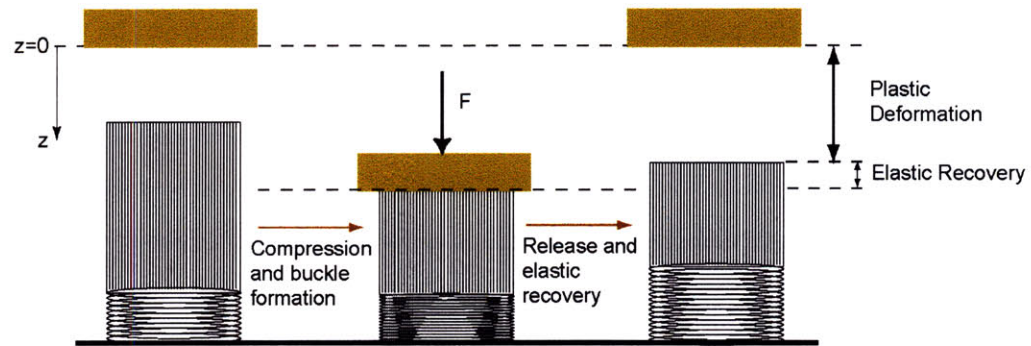
Figure 3-15 a shows incremental compression of a circular column with a diameter of  $400\mu m$ . The column is compressed in  $50\mu m$  increments until a total displacement of  $300\mu m$  imposed by the punch. During the test routine, before moving on to the next deformation stage, i.e. to the next incremental deformation, the column was compressed one more time with the same deformation amount. Since the buckles are already formed, the force-displacement curve only shows the elastic region, having the same stiffness with the elastic recovery portion. This is



(a)



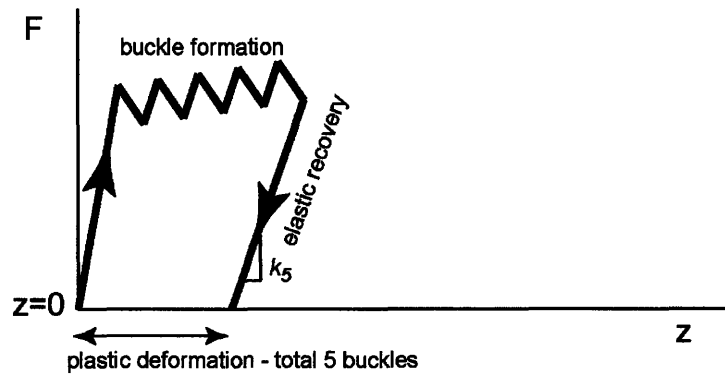
(b)



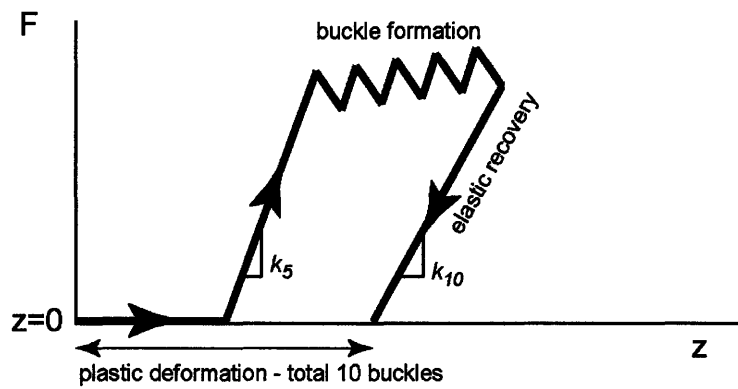
(c)

Figure 3-13: Sketch demonstrating the test procedure where CNT column are successively compressed to larger deformations resulting in increased number of buckles (a) 5 buckles. (b) 10 buckles. (c) 15 buckles.

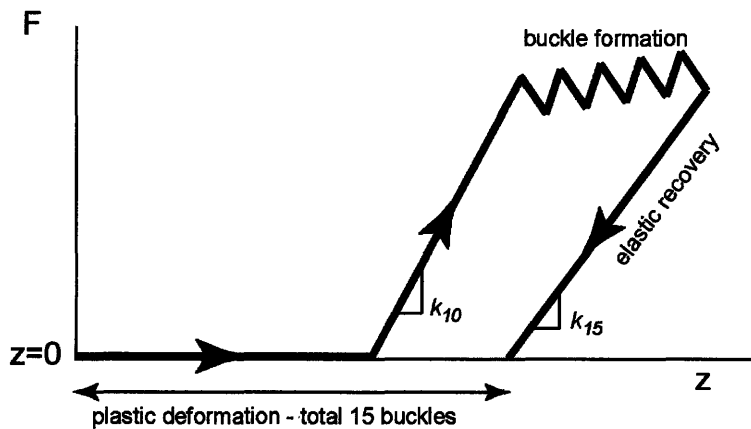




(a)



(b)



(c)

Figure 3-14: Sketch depicting mechanical behavior of CNT columns. Note that elastic recovery occurs through different stiffnesses depending on number of buckles formed during compression: (a) 5 buckles,  $k_5$  (b) 10 buckles,  $k_{10}$  (c) 15 buckles,  $k_{15}$

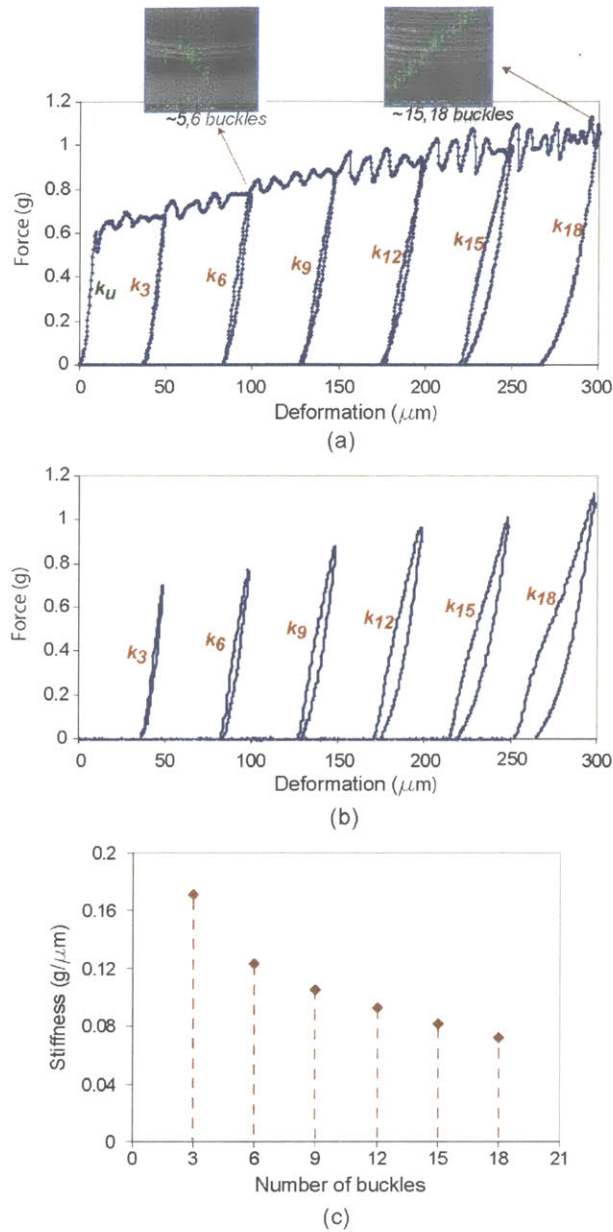


Figure 3-15: (a) Compression test results of CNT column with  $400\mu\text{m}$  diameter. The compression cycles are performed in  $50\mu\text{m}$  increments. (b) Second touchdown tests performed after each cycle before imposing the next incremental deformation, demonstrating elastic operation after any cycle without forming a new buckle. (c) Stiffness values measured during elastic recovery or initial compression of the next cycle. The stiffness values are plotted against the corresponding number of buckles (approximate).

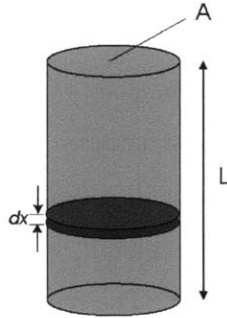


Figure 3-16: Cylindrical element with length  $L$  and cross-sectional area of  $A$ .

repeated after each cycle and the force-deformation curves are shown in Figure 3-15 b.

The stiffness values corresponding to each cycle in Figure 3-15 a is plotted as a function of the total number of buckles (approximate) formed in Figure 3-15 c. The stiffness values decrease as the number of buckles increase. Intuitively, this is expected since as previously discussed, the buckles deform similar to a bellow and perform as springs, and as more buckles are formed, effectively additional springs in series are introduced to the structure, reducing the overall stiffness. This is discussed in detail in Section 3.2.4.

### 3.2.4 Modeling and Analysis

By the assumptions of classical mechanics, for a column shown in Figure 3-16, the vertical stiffness is given by:

$$k = E \frac{A}{L} \quad (3.2)$$

where  $E$  is the Young's modulus of the material the column is made of, and  $A$  and  $L$  are the cross-sectional area and length of the column respectively. Equation 3.2 is derived by assuming uniform strain along the length of the column and integrating that strain, which is:

$$\epsilon = \frac{\sigma}{E} \quad (3.3)$$

where  $\sigma$  is the stress.

For CNT structures, however, the uniform strain assumption is not valid beyond the initial

and very short elastic region. Most of the deformation occurs locally, where the buckles form, and not uniformly distributed along the length of the structure. The fact that CNT columns show a very unique deformation mechanism, along with the other observations discussed above, motivated a more detailed study of these structures.

There are two contributions to the overall compliance of a CNT column. The first is the compliance of the aligned portion of the column, where the stiffness depends on the length of the aligned portion and is linear elastic. The second one is the compliance of the buckled portion of the column, where the compliance depends on how many buckles there are. As observed in Figure 3-15, the stiffness of the structure reduces as more buckles are added. This is mainly due to the additional springs added in series with the previous ones, which make the buckled portion of the structure more compliant. On the other hand, as more buckles form, the length of the aligned portion gets smaller, making it stiffer. However, for a given number of buckles, the stiffness is linear elastic. Overall, the addition of new springs in series due to buckle formation overwhelms the stiffening of the aligned portion.

The definitions used in the compliance modeling are depicted in Figure 3-17 a. The stiffness of the aligned portion can be calculated as

$$k_{aligned} = E_a \frac{A}{L_a} \quad (3.4)$$

where  $E_a$  is the modulus of the VA-CNT structure in the elastic region,  $A$  is the area of the column, and  $L_a$  is the length of the aligned portion. On the other hand, assuming that the stiffness of each buckled layer is the same, the stiffness of the buckled portion can be expressed as:

$$k_{buckled} = \frac{k_b}{n} \quad (3.5)$$

where  $k_b$  is the stiffness of one buckled layer and  $n$  is the number of buckles. The overall stiffness of the structure can be calculated using

$$\frac{1}{k_{total}} = \frac{1}{k_{aligned}} + \frac{1}{k_{buckled}} \quad (3.6)$$

The stiffness model is shown in Figure 3-17 b. The modulus of the aligned portion can be

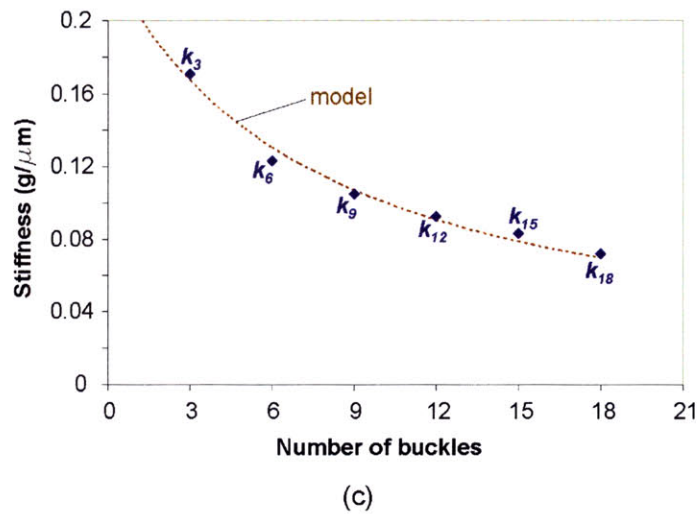
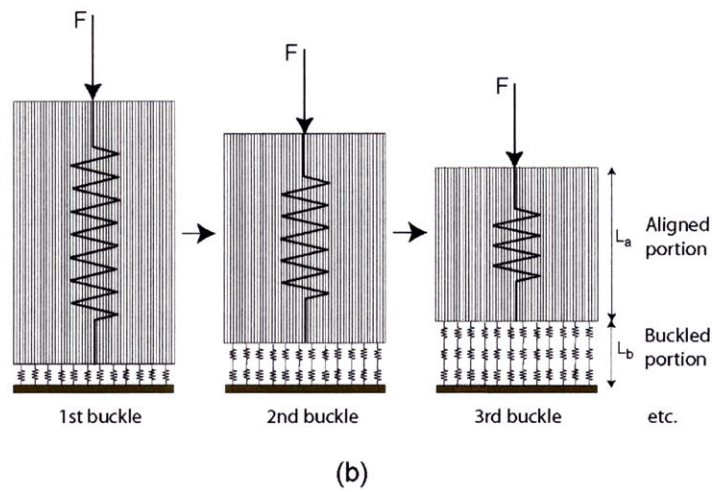
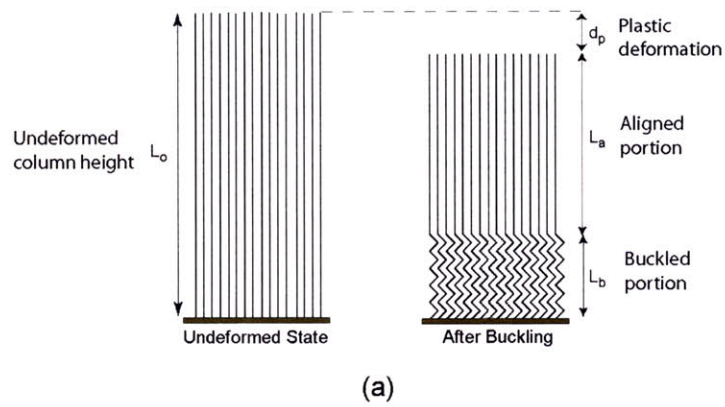


Figure 3-17: (a) Definitions used in the deformation model. (b) Model of CNT column deformation where each buckled layer adds a new springs in series, thereby reducing overall stiffness of the structure. (c) Model correlation with test data.

calculated from the initial compression before any buckles are formed. This stiffness is labeled as  $k_u$  in Figure 3-15 a. For the case of CNTs grown with the fixed catalyst method and argon flush, it can be said that the plastic deformation is roughly three times the length of the buckled portion of the column, which can be expressed as:

$$\frac{d_p}{L_b} \sim 3 \quad (3.7)$$

Also it is observed that each buckle formation results in approximately  $18\mu m$  of plastic deformation and average length of a buckle is  $7\mu m$ . The length of the aligned portion then can be calculated as:

$$L_a = L_o - (d_p + L_b) \simeq L_o - 25n(\mu m) \quad (3.8)$$

where  $L_o$  is the initial height of the column and  $n$  is the number of buckles. The initial height of the column tested and shown in Figure 3-15 is  $478\mu m$ . The stiffness of an individual buckle,  $k_b$  is calculated using the stiffness after the last cycle where the length of the aligned portion is only  $28\mu m$  and most of the compliance is due to the buckled portion. Plugging the  $E_a$  calculated from the measurement of  $k_u$  and the  $k_b$  into the model described above, the theoretical predictions are plotted along with the stiffness measurements in Figure 3-17, showing good correlation. Even though this model is fairly simple, it demonstrates that the aligned portion has a contribution to the deformation mechanism. Without taking it into account, namely accounting for only the compliance due to individual buckles, and assuming only springs in series, the model predicts a much steeper stiffness decrease, which is not observed in the data.

### 3.2.5 Effect of Column Area on Stiffness

The same compression routine is repeated for columns of different cross-sectional area as grown from the mask shown in Figure 3-18. A typical test die is also shown in the same figure. The mask has square and circular columns which have the same cross-sectional area in a given row. The main goal of this mask design is to enable a fair comparison between mechanical properties of different size and shape columns due to the fact that all of the columns are grown at the very same conditions, namely during the same CVD run. This eliminates any possible process

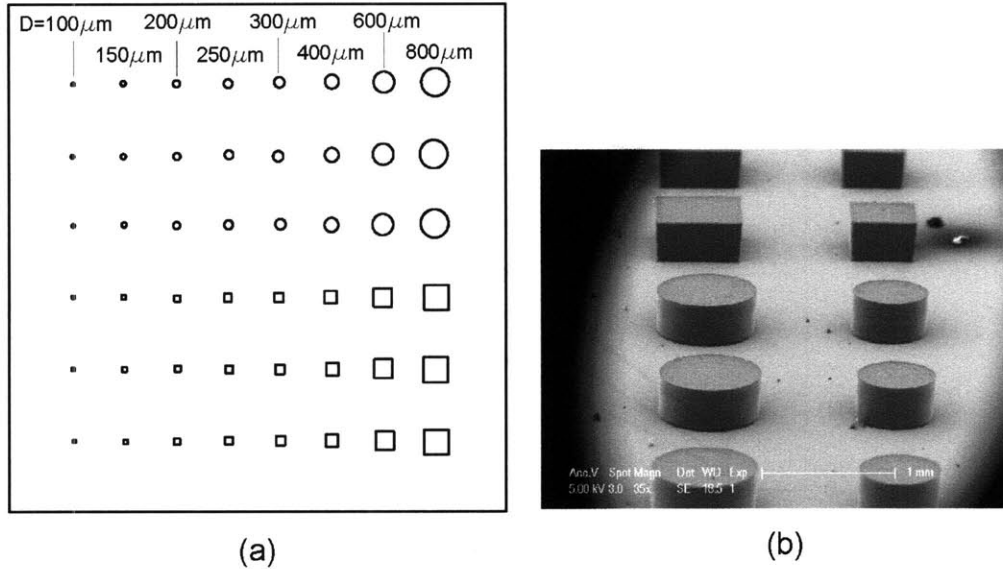


Figure 3-18: (a) Mask for the test structures. (b) Columns grown to various shapes with floating catalyst CVD.

variation between different growths.

As discussed, each final compression amount results in a different stiffness value. To keep the comparison fair, stiffness values of columns of different areas are compared at the same compression amount. Figure 3-19 depicts stiffness values of columns having various areas after different compression amounts, namely  $100\mu m$ ,  $200\mu m$  and  $300\mu m$ . It can be seen that the stiffness of CNT columns is directly proportional to the area. Also, as discussed earlier, as the compression amount increases, the number of buckles increase, and hence the slope of the curve for the  $300\mu m$  is the lowest.

The finding that the stiffness is proportional to the column area indicates that all of the carbon nanotubes in the column contribute to the overall stiffness of the structure. In other words, the deformation is occurring throughout the cross-section instead of only at the perimeter. To investigate this further and to understand if the buckles form inside the column as well, a deformed column with buckles already formed is cut in the middle using focused ion beam (FIB), shown in Figure 3-20 a. One of the halves is removed and the cut section is observed with SEM. From Figure 3-20 b,c d it can be clearly seen that the morphology of the whole

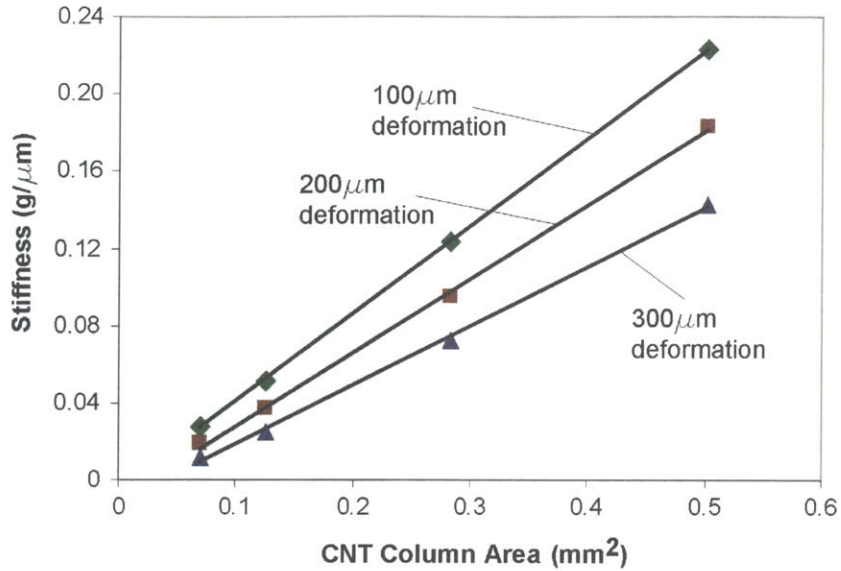


Figure 3-19: Stiffness of the CNT columns is proportional to the cross-sectional area of the column. Stiffness values of various area columns are plotted after different compression amounts.

cross-section is changed during buckle formation, and the whole area is contributing to the deformation mechanism. This also explain why the stiffness values, at any deformation level and number of buckles, is directly proportional to the area.

### 3.2.6 Lateral Stiffness of Vertically Aligned CNT Structures

All of the experiments and analysis presented so far in this chapter pertain to vertically aligned CNT structures which are compressed in the direction parallel to the CNT alignment. This section present testing of a CNT column in lateral direction, i.e. compression in a direction perpendicular to the alignment of the CNTs. Along with general curiosity, part of the motivation for this test is the fact that more force is required to form the next buckle every time, which is similar to strain hardening. The previous section has analyzed and modeled the stiffness of the CNT column, but the buckling phenomena and its detailed investigation are beyond the scope of this discussion. Nevertheless, to investigate if there is any stiffening is happening, a CNT column, which is almost a cube ( 530x530x520 $\mu\text{m}$ ) is tipped over onto the substrate it is grown and compressed with the punch of the tribometer as shown in 3-21 a. Figure 3-21 (b)



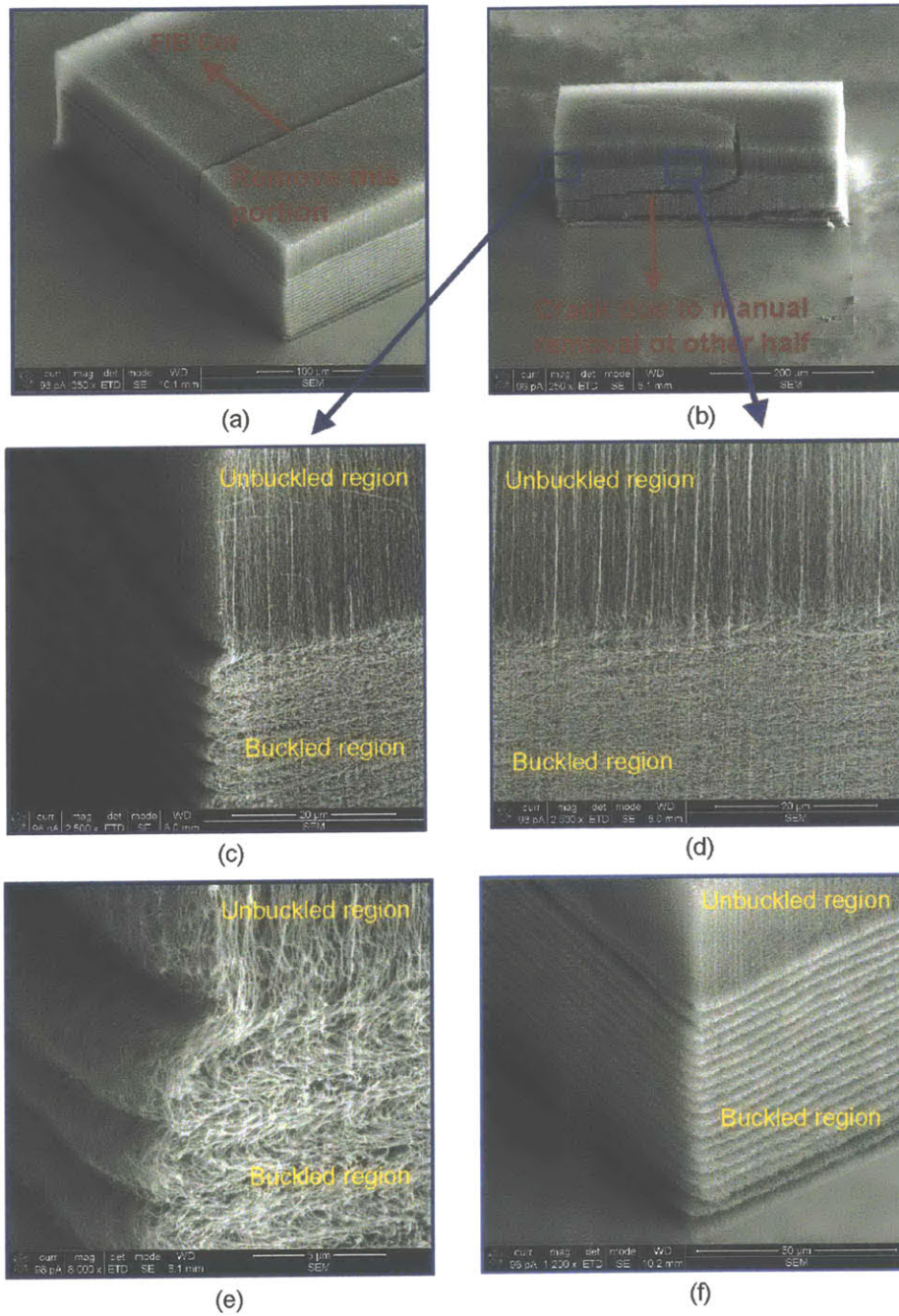


Figure 3-20: (a) A compressed column cut with focused ion beam (FIB) to see the cross-section of the column after buckle formation. (b) Half of the column removed. Buckled region spans the whole cross-section. (c, e) Close-up images of the the corner of the column and (d) middle section showing the transition from unbuckled region to buckled region. (f) Regular corner of a buckled column for comparison with cut corner.

shows test data from the compression test. It can be clearly seen that the structure becomes stiffer as it get densified. Similar to the case of vertical compression, there are once again large plastic deformations occurring, followed by relatively short elastic recovery.

Figure 3-21 (c) plots the stiffness values measured from Figure 3-21 (b) as a function of the compression amount. It also compares the stiffness change of a same area column (circular) in vertical compression at same deformation levels. It is interesting to note that the same structure behaves very differently in lateral and vertical direction, demonstrating that VA-CNT structures are highly anisotropic.

Figure 3-22 shows SEM images of the sidewall of laterally compressed CNT column and compares with the sidewall prior compression. There is no easily observable morphology change, however, it should be noted that these structures are highly porous (99.6%) and the CNTs are very tangled. These factors make the observation of the densification optically difficult.

### **3.2.7 Hydrogen Preconditioning of Catalyst**

The same experimental procedure is followed with columns grown by CVD with hydrogen flush. Test results are shown in Figure 3-23 for a column with the same dimension discussed in Figure 3-15. The mechanical behavior is the same except the forces are higher. To further investigate this change, stiffness values corresponding to  $200\mu m$  imposed deformation for different area columns for the cases with and without hydrogen flush is compared in Figure 3-24. It can be observed that the stiffness values of CNT columns grown with hydrogen flush is four times larger than the stiffness of CNT columns grown with hydrogen introduced only shortly before the growth starts.

This significant stiffness change is attributed to the different CNT diameter and spatial density resulting from the hydrogen flush. Details of the resulting CNT structure was discussed in previous chapter. From Figure 2-8 it can be seen that introduction of hydrogen at the beginning of the CVD process results in CNT density increase accompanied by a CNT diameter decrease, resulting in an overall stiffness increase by four times. If there was no change in diameter, in other words, if the density change was the only morphology difference between the two cases, one would expect the stiffness to scale directly with CNT density. This conclusion is based on the findings of the previous sections of this chapter where it was found that stiffness of

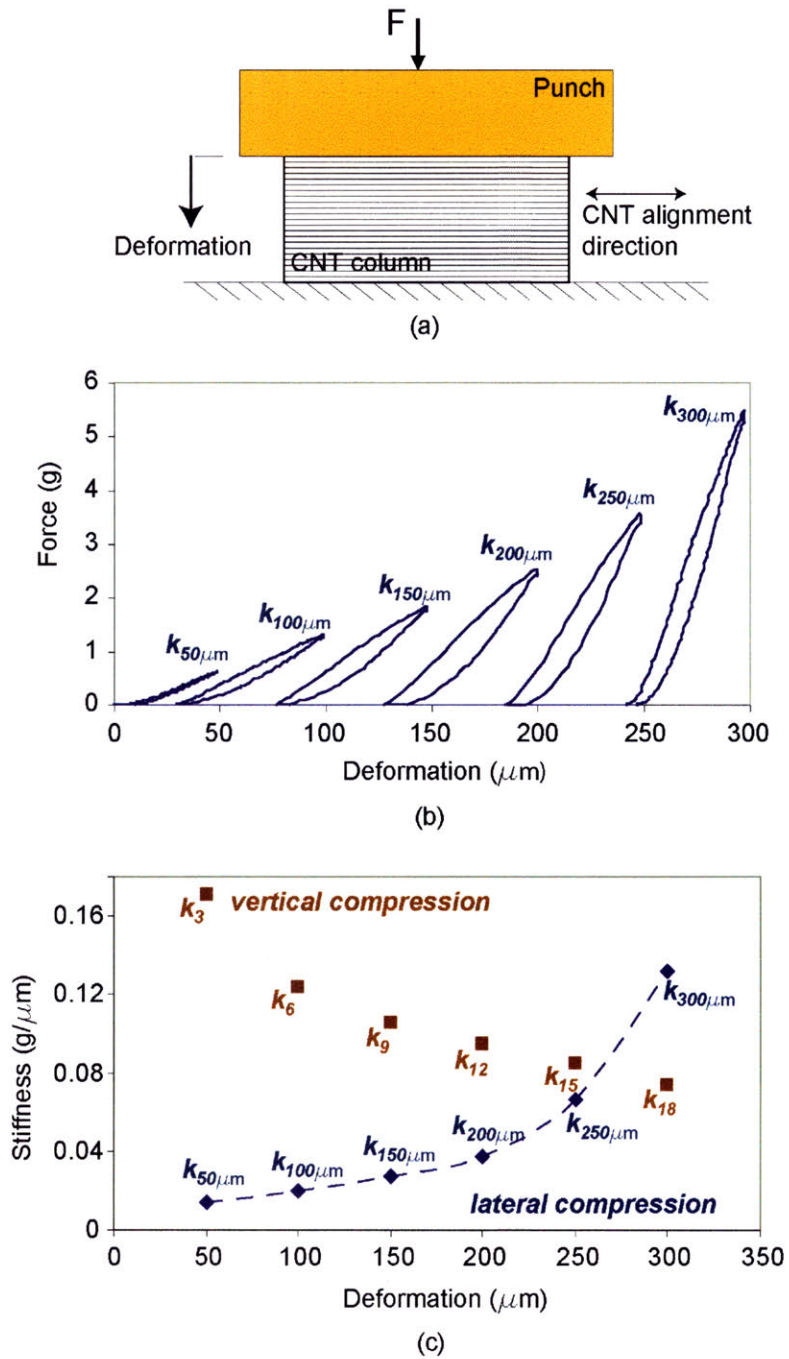


Figure 3-21: (a) Test configuration to characterize lateral stiffness of CNT column. (b) Test data showing that as the column gets densified, its stiffness increases. There is again large plastic deformation followed with relatively short elastic recovery. (c) Comparison of stiffness change during vertical and lateral compression.

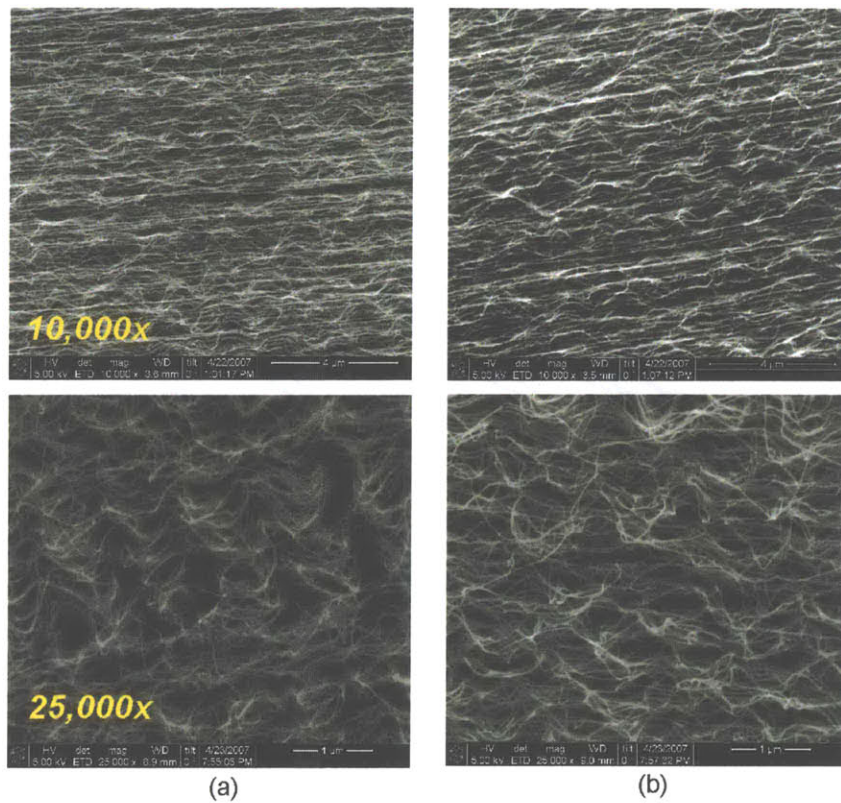


Figure 3-22: (a) SEM images of the sidewall of a CNT column before densification. (b) SEM images of the sidewall after 300 μm compression.

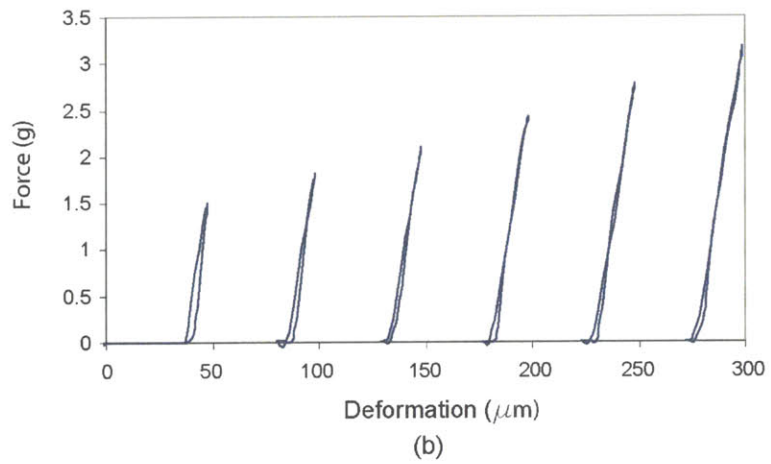
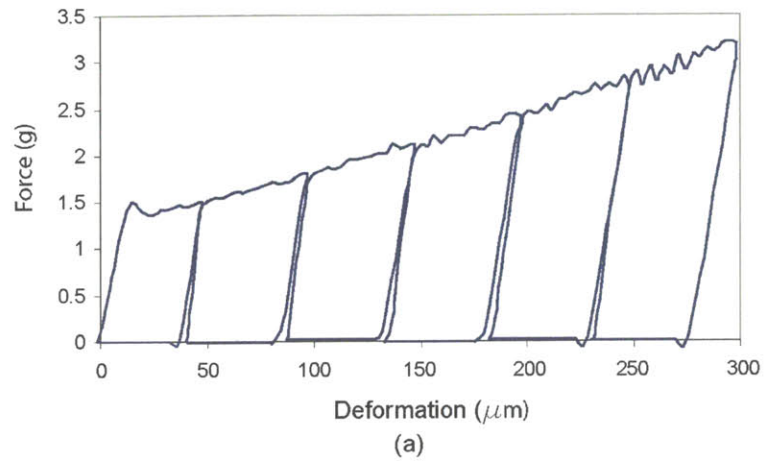


Figure 3-23: (a) Compression test and successive buckle formation of a CNT column grown with fixed catalyst method using hydrogen flush throughout the CVD process. (b) Stiffness values corresponding to successive buckles.

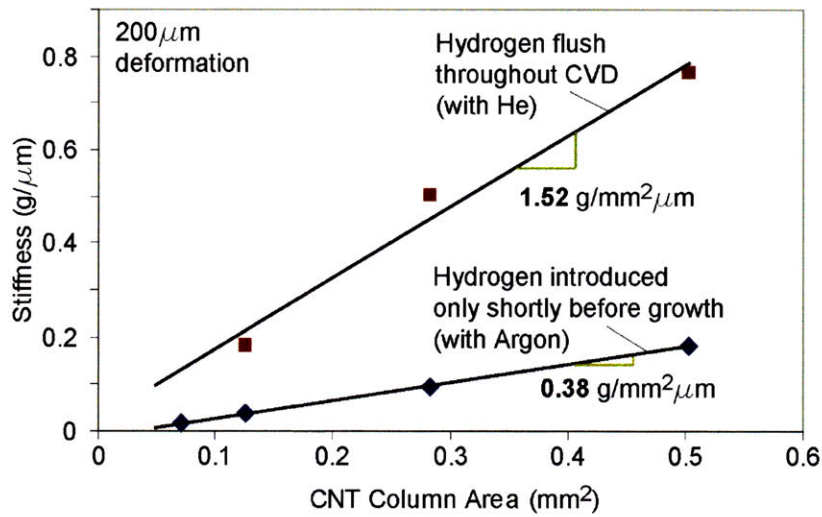


Figure 3-24: Effect of hydrogen flush throughout the CVD growth. The stiffness of the same size column under same test conditions increase four times.

a CNT column is directly proportional to the area and all the CNTs in the structure contribute to the deformation mechanism. As the area increase translates into an increase in number CNTs in the column, the density increase should also translate directly into a proportional stiffness change. As the average CNT diameter also changes, and the deformation mechanism is rather complicated, a detailed analysis of the individual contributions of the density and diameter of CNTs is beyond the scope of this thesis. Nevertheless, this result constitutes the first demonstration of stiffness tuning of CNT structures by modification of CVD gas composition during CNT growth.

### 3.3 Deformation Mechanism of Columns Grown with Floating Catalyst CVD

#### 3.3.1 Initial Observations and In-situ SEM compression

For the case of growth with the floating catalyst, buckle formation can still be observed, but the buckles recover almost fully after the force is released. This behavior is observed in-situ

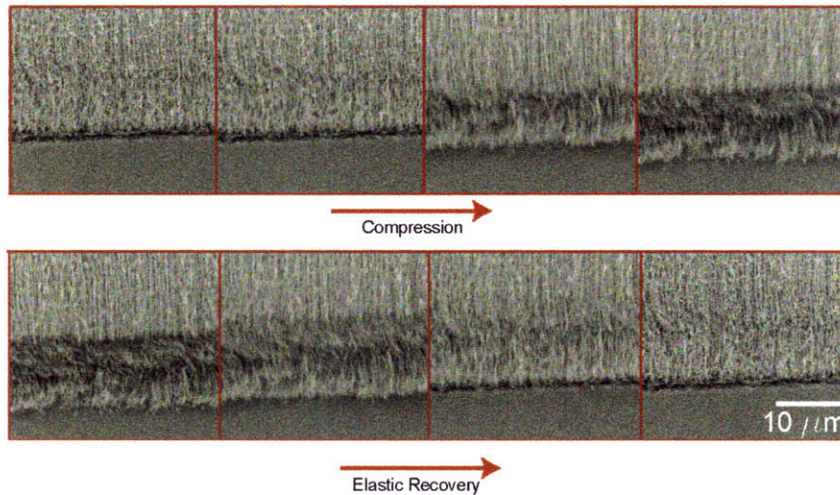


Figure 3-25: In-situ SEM compression test snapshots of a CNT column grown with floating catalyst recipe. The images show the bottom section of the column. (a) Compression. (b) Subsequent release, showing the buckled region recovers elastically.

SEM, shown in Figures 3-25 and 3-26.

In almost all of the experiments, buckle formation started at the bottom. In some very rare cases, columns started buckling/deforming in the middle. However, these were circular columns and it is likely that particular run yielded a different morphology and the shell of the column had different properties than the inside, causing the structure start deforming in the middle.

### 3.3.2 Detailed Testing with Tribometer

As CNT columns grown with floating catalyst behave different than the columns grown with fixed catalyst recipe, the same test routine applied for fixed catalyst CNT columns is not repeated. As the columns recover elastically, they are compressed at different compression levels and force data is recorded. It is observed that the columns tested, which were grown using the same mask shown in Figure 3-18, can sustain deformation up to  $100\mu m$ . Beyond this, they start forming macro cracks parallel to the CNT direction. This is attributed to the fact that the top portion of the columns is highly tangled and there is no force holding CNTs together, and after a certain force level is achieved, they are pushed sideways by the punch compressing the column.

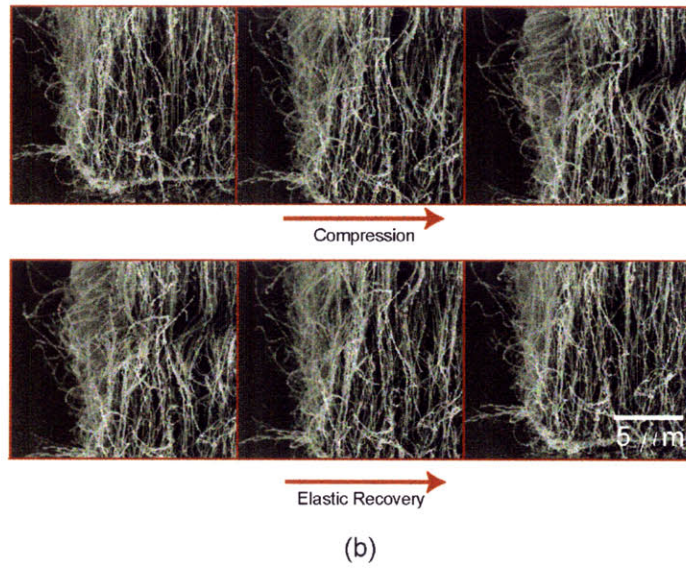
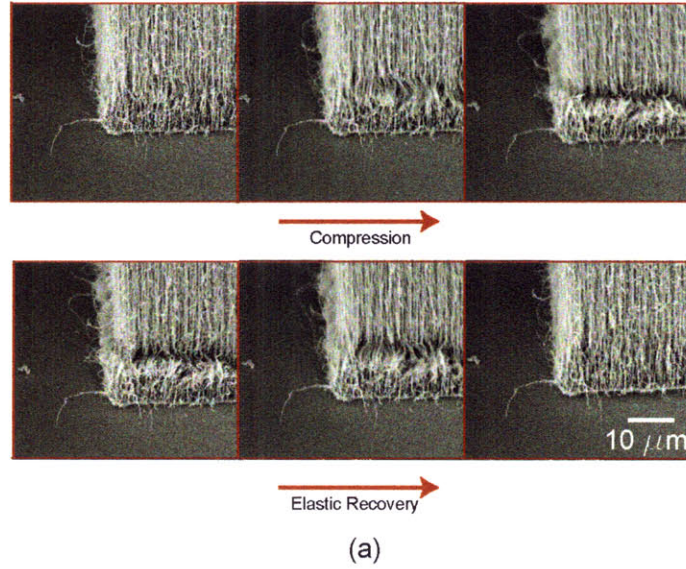
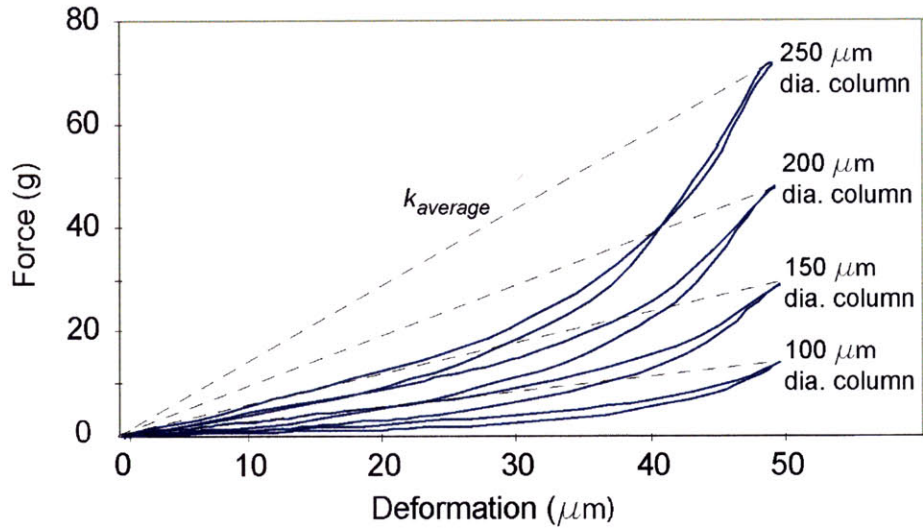
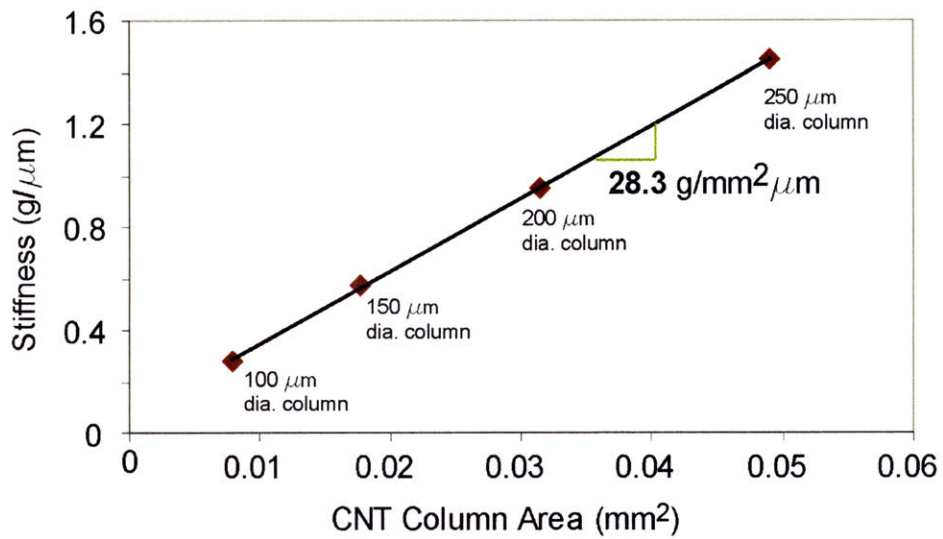


Figure 3-26: Cloe-up snapshots of the corner of a CNT column grown with floating catalyst during in-situ compression test.





(a)



(b)

Figure 3-27: (a) Compression test results of CNT columns grown with floating catalyst. (b) Average stiffness of the CNT columns plotted against column area.

Test results of various area columns are shown in Figure 3-27 (a) for  $50\mu m$  compression. As the columns are compressed, the stiffness increases resulting in nonlinear behavior. To be able to compare stiffness values of different area columns, the average stiffness values are measured, which is calculated using the straight line connecting maximum force and deflection with the initial point. Figure 3-27 (b) plots the average stiffness values as a function of the column area. Again, the stiffness of CNT columns is proportional to the area, indicating that all of the CNTs in the structure contribute to the stiffness.

Another very important observation is that CNT columns grown with floating catalyst are approximately 75 times stiffer than CNT columns grown with the fixed catalyst method (Argon flush), and approximately 18 times stiffer than CNT columns grown with fixed catalyst method and hydrogen flush. The numbers mentioned above are based on the slopes in the Figures 3-24 and 3-27 (b). It should be noted that the stiffness values of CNT columns depend on the final compression amount. For example, the stiffness values in Figure 3-24 correspond to a compression amount of  $200\mu m$ . A larger deformation will result in softer columns. Similarly, stiffness values in Figure 3-27 (b) correspond to  $50\mu m$  compression. Due to the nonlinear nature of the deformation mechanism, a smaller deformation will result in a smaller stiffness value. Nevertheless, these stiffness variations among one type of CNT column are relatively small compared to the huge difference between the stiffness values resulting from fixed and floating catalyst recipes.

### **3.4 Fundamental Findings and Guidelines for Probe-Design**

Previous sections of this thesis presented a detailed investigation and analysis of the deformation mechanism of columns made of vertically aligned carbon nanotubes. This section summarizes the fundamental findings of this chapter and discusses the implications of the observations for realistic applications such as probe design.

### **3.4.1 Effect of CVD Growth Method and Parameters on Mechanical Properties of CNT Structures**

As discussed earlier, the stiffness of CNT column, whether from fixed or floating catalyst CVD growth, depends on the deformation level. In the case of fixed catalyst CVD method, the deformation dictates the amount of buckles formed, and hence the ultimate compliance of the structure. On the other hand, for the floating catalyst CVD method, the deformation of the columns is nonlinear and larger deformations result in a stiffer structure. Nevertheless, these changes are relatively small, compared to the big differences between CNT columns coming from these different recipes. Structural stiffnesses of CNT columns of the types discussed are plotted against structural density in an Ashby chart [34] along with Young's Modulus of conventional materials. It should be emphasized that even though structural stiffnesses of CNT structures is compared with conventional materials on the Ashby chart, these values are not Young's Modulus as Young's modulus is defined for structures/materials which deform uniformly along the length of compression, which is not the case for CNT structures, except the very short initial elastic region. Hence, these values are defined as "structural stiffness". The structural stiffness values are calculated using equation 3.2 and the initial height of the column as  $L$ .

It is interesting to note that, as-grown CNT columns are lighter than aerogel materials for which elastic modulus has been reported. The lightest reported aerogel has a density of  $4\text{kg/m}^3$ [35], for which, however, no elastic properties are reported. This implies that CNT structures can be useful in weight sensitive applications as well. Also, since they can deform to very large strain levels plastically (fixed catalyst CNTs), they can have applications where energy absorption is critical. Instead of following the test routine described earlier in this chapter, one can take a CNT column, and deform all the way until all the aligned portion is consumed and turned into buckles, resulting in large energy absorption in the form of plastic deformation.

### **3.4.2 Summary of Findings for Fixed catalyst CNT Structures**

CNT columns grown with fixed catalyst recipe demonstrated a novel stiffness tuning method where the stiffness of the structure can be predictively controlled by the imposed deformation. The stiffness of the structure can be further tuned by changing the gas composition during

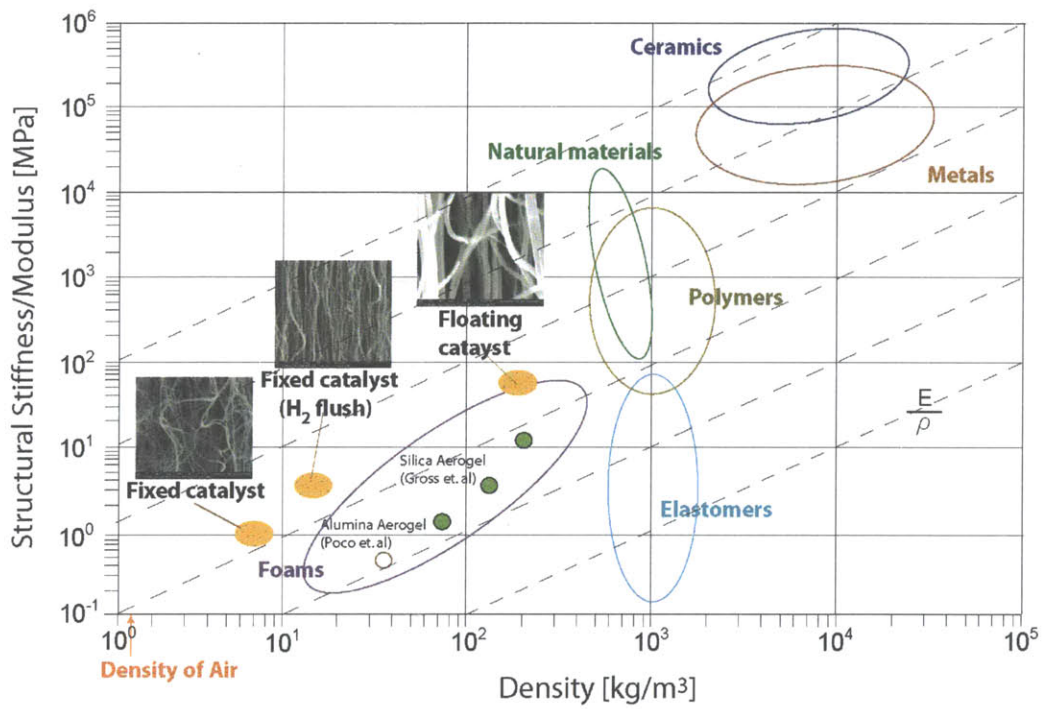


Figure 3-28: Ashby chart comparing mechanical properties of CNT structures grown with various CVD growth methods with conventional materials.

growth, namely introducing hydrogen at the very beginning of the CVD process. These are important findings as they enable designers to choose geometry, fabrication process and subsequent structural modification for desired mechanical properties. The fundamental observations for the case of fixed catalyst CNT structures can be summarized as:

- After localized plastic deformation/buckle formation, there is elastic recovery, which can be used as a spring.
- Each buckled layer acts as a spring and breath during the elastic deformation.
- Elastic properties can be controlled by controlling the imposed deformation and thereby the amount of buckles formed, or cross-sectional area.
- Buckle formation is shape and size independent.
- Elastic properties depend on the area, not the shape.
- Buckling starts at imperfections, i.e. buckles can start at the top of a column, or in the middle as well.
- Elastic properties of a CNT structure depend on average CNT diameter and CNT spacing.
- VA-CNT structures are highly anisotropic. Stiffness in the lateral direction increases with increased deformation.

These findings can also be summarized in equations which can be used as useful design tools. For example, the stiffness of a column can be expressed as

$$k_{fixed} = \frac{c_b A}{d_p} \quad (3.9)$$

where  $A$  is the area of the column,  $d_p$  is the imposed plastic deformation and  $c_b$  is a growth condition dependent coefficient, which would be different for the cases of growth with and without hydrogen flush. Also, the over-travel, or the useful elastic range, can be expressed as

$$OT_{fixed} = c_t d_p \quad (3.10)$$

where  $c_t$  is again a growth condition dependent coefficient. This equation basically summarizes the fact that as the imposed deformation increases, number buckles increase, and since each buckled layer has a elastic range, the overall elastic range of the structure, or the over-travel increases.

These findings can also be summarized in a graph, shown in Figure 3-29, which is basically the stiffness map of the CNT columns for given CNT column diameter, which directly translates into the pitch of the column, and the deformation amount. In fact, Figure 3-29 is just another interpretation of Figure 3-19, where the stiffness values are plotted as a function of the column area for the case of fixed catalyst CVD growth.

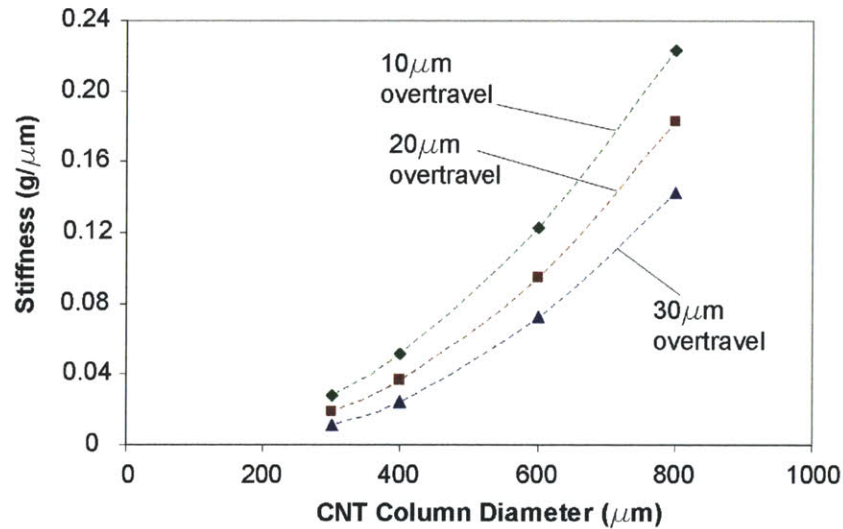


Figure 3-29: Stiffness map of various geometry and compression level CNT columns which can be used for design purposes.

### 3.4.3 Summary of Findings for Floating catalyst CNT Structures

CNT columns grown with floating catalyst recipe demonstrate elastic recovery and nonlinear behavior. The average stiffness calculated by the final deformation and corresponding force is proportional to the column area. The fundamental observations can be summarized as:

- There is localized reversible deformation.

- Buckle formation occur but the buckles recover elastically.
- Elastic properties can be controlled by cross-sectional area.

These findings can also be summarized in the following equations:

$$k_{fl} = c_f A \quad (3.11)$$

where  $k_{fl}$  is the stiffness of the column,  $A$  is the column area, and  $c_f$  is a growth condition dependent coefficient. This thesis dealt with only one growth condition for the floating catalyst recipe, but any process parameter affecting CNT diameter or density would change this coefficient. And, as discussed earlier, the overtravel needs to be lower than a certain value to avoid cracks in the structure:

$$OT_{fl} \leq OT_m \quad (3.12)$$

where  $OT_m$  is the maximum overtravel allowed for the structure.





## Chapter 4

# Transfer of CNT Structures onto Conductive Substrates and Electrical Characterization

The previous chapters discussed CNT growth techniques and mechanical characterization of CNT structures. For probing applications, electrical conduction through the CNT structures as well as electrical coupling to the base substrate are critical for successful device operation. This chapter presents a transfer printing technique to simultaneously transfer, densify and electrically connect CNT structures onto metal substrates and a methodology for characterizing electrical properties of VA-CNT structures.

Growth of vertically-aligned CNTs (VA-CNTs) by thermal chemical vapor deposition discussed in Chapter 2 has created films and microstructures containing large numbers of CNTs in parallel. Unfortunately, these high-temperature synthesis processes are typically optimized for growth from metal nanoclusters on silicon and ceramic substrates, while most devices utilizing these CNTs will require a wider variety of substrates, including metals and plastics which cannot withstand the harsh conditions for high-yield CNT growth. Growth of VA-CNTs by thermal CVD with simultaneous ohmic contact on electrically conductive substrates is a major challenge due to the apparent necessity of a buffer layer such as  $Al_2O_3$ ,  $SiO_2$ , or  $MgO$  for high-yield VA-CNT growth. Further, weak mechanical adhesion to the substrate and low

bulk density often prevent robust electrical and mechanical integration of CNTs in as-grown conditions.

An emerging approach for device integration of VA-CNTs is to transfer the VA-CNTs from the growth substrate to a second “device” substrate. Full films of VA-CNTs have transferred with a main emphasis on field emission applications; however, the nature of interconnection to the CNTs, and the lengthwise electrical and mechanical properties of the transferred films have not been assessed. CNTs have been previously embedded in an otherwise insulating matrix to form conducting composites [36], but these are not aligned CNTs. Demonstrations of transfer processes of VA-CNTs in the literature have been on bulk quantities of carbon nanotubes and more specifically on aligned CNT films mostly aimed for field emission applications [37, 38, 39], where no electrical measurements are presented through the thickness of the transferred film. To our best knowledge, the only electromechanical characterization (excluding actuation demonstrations) of transferred VA-CNTs is presented in [40] where the resistance perpendicular to the array is measured as the array is again strained in the same direction. However, for conductive CNT composites, a complete electromechanical characterization parallel to the CNT array has not been reported.

This chapter presents a low temperature, robust and versatile process for transfer-printing films and arrays of patterned microstructures of VA-CNTs, which demonstrates good electrical and mechanical coupling to the CNTs as well as useful mechanical and electrical integrity of the structures under compressive loads. A layer of two-part conductive epoxy facilitates simultaneous transfer and reinforcement of the structures, creating the first conductive composite CNT micro-probes. Selection and preparation of the device substrate is decoupled from conditions for high-yield and high-quality synthesis of VA-CNTs, enabling direct integration of CNTs grown using already established high-temperature CVD processes. This is also a new platform for electromechanical characterization of parallel assemblies of CNTs and other nanostructures, enabling new insights on their interfacial (e.g., thermal and electrical contact resistance) and bulk properties.

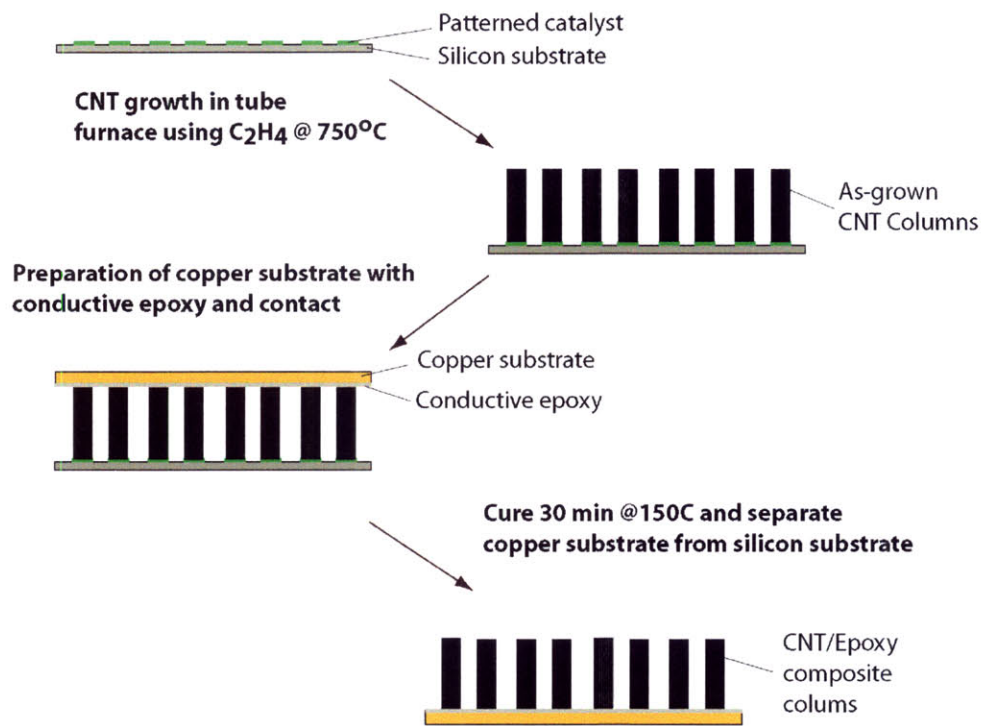


Figure 4-1: Fabrication sequence of the CNT columns. The columns are grown from a patterned catalyst on silicon substrate, and then transferred onto a copper substrate using a thin conductive epoxy.

## 4.1 Transfer Process

The transfer process, summarized in Figure 4-1, starts by covering a copper substrate with a thin layer of two part isotropic conductive epoxy (Loctite 3888), which consists of a silver paste and hardener. To establish a uniform epoxy film thickness, tapes are applied on both edges of the substrate. Then the epoxy is applied in the area between the tapes, and then the epoxy is spread with a razor blade which slides along the tapes as reference edges. The copper substrate is then brought into contact with CNT columns, and gentle vertical pressure is applied to avoid collapse or shearing of the columns (Figure 4-2(b) and 4-2(c)). The assembly is cured at 150 °C for 30 min. to achieve final strength of the epoxy. The copper substrate is then manually separated from the silicon substrate, and the CNT columns are transferred to the copper substrate, owing to the relatively strong adhesion with the epoxy compared to the weak adhesion to the growth substrate (Figure 4-2d).

Figures 4-2(e) and 4-2(f) show SEM pictures of as-grown columns and columns after they are transferred onto copper substrate. Large arrays of CNT columns having different cross-sectional area and pitch can be transferred with this method. Figure 4-3 a shows transferred CNT columns having various pitches and cross-sections and Figure 4-3 b shows columns with 100  $\mu\text{m}$  pitch and 50  $\mu\text{m}$  x 50  $\mu\text{m}$  cross-section.

## 4.2 Internal Structure

Figure 4-4a shows a single transferred CNT composite column (“micro-probe”). The curing process causes the columns to shrink to about 80% of their original width as well as results in “mushroom-like” tops. During curing, the epoxy consistently wets and penetrates into the columns except the top portion, and leaves a “cap”, which is comprised of not wetted and sharp CNT tips due to the peeling off from the substrate. Capillary action causes the CNTs to densify; capillarity-driven assembly and wetting phenomena of CNT films have been previously reported [41].

To examine their internal structure, micro-probes were sectioned as shown in Figure 4-4b, by laser micromachining (Resonatics, 248nm KrF excimer @ 100Hz, 33kV). It can be seen that the wetting/curing process shrinks the cross-sectional area of a column, and causes formation

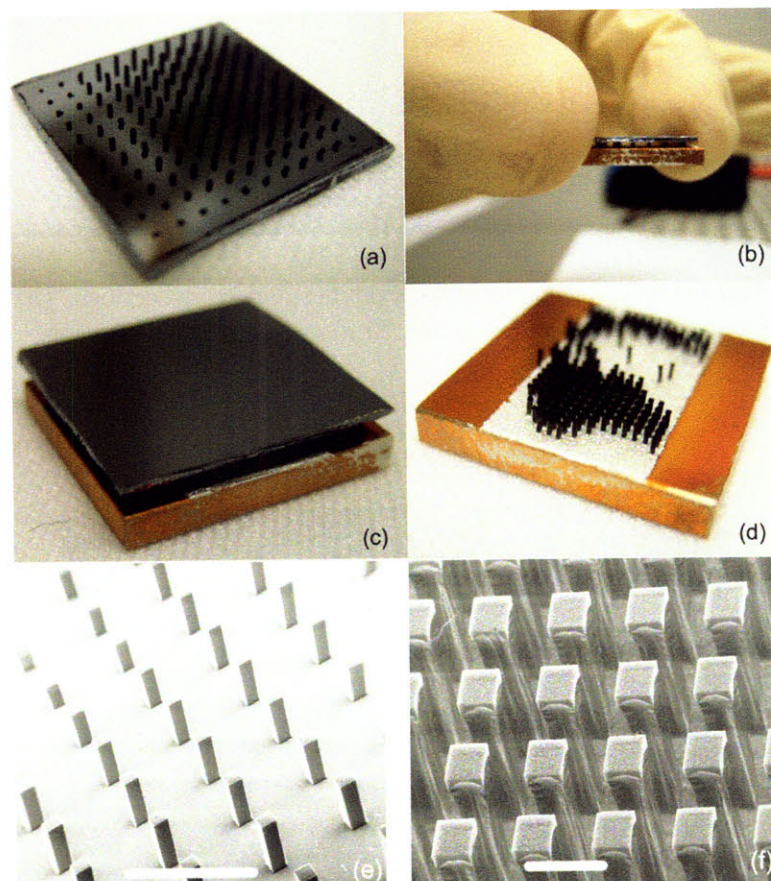


Figure 4-2: Transfer process from silicon substrate to a copper substrate using a thin film of epoxy. (a) As-grown columns on silicon substrate. (b), (c) Copper substrate, epoxy layer, CNT columns and silicon substrate assembly after curing. (d) Composite CNT columns on copper substrate after separation from silicon substrate. Uniform height after growth, alignment of the two substrates and pressure applied prior curing are critical for a good transfer. SEM images of (e) as grown MWNT columns from patterned catalyst and (f) large array of transferred columns onto copper substrate. Note the “mushroom” structures. The scaling bar in (e) corresponds to 2 mm and scaling bar in (f) correspond to 500 $\mu$ m.

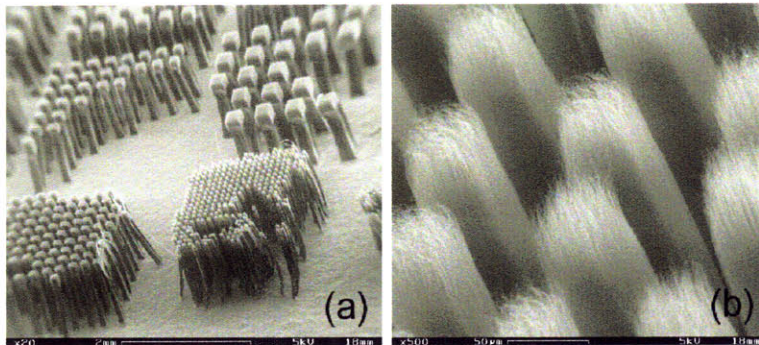


Figure 4-3: (a) Transferred columns of various pitches and cross-sections. (b) Close up image of transferred columns with  $100\ \mu\text{m}$  pitch and  $50\ \mu\text{m} \times 50\ \mu\text{m}$  cross-section

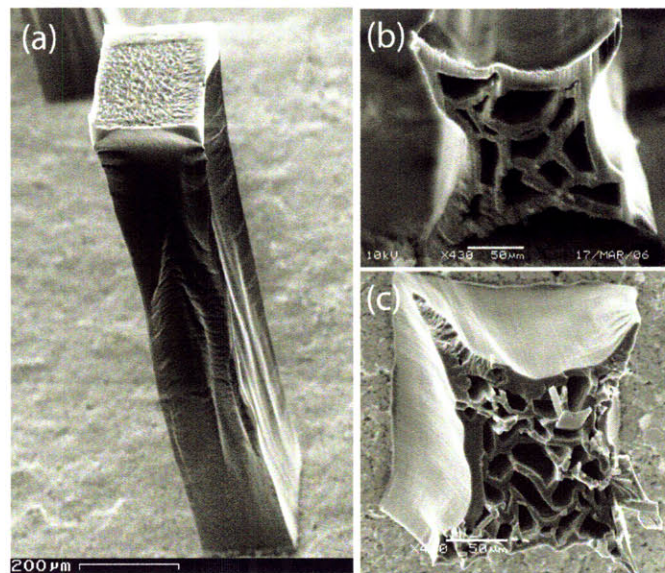


Figure 4-4: (a) SEM image of a composite CNT micro-probe. The CNT columns typically shrink to 80% of their original width due to capillary action of penetrating composite resin during curing process (b) Cross-section of the micro-probe after cutting with laser beam. The cross-section shrinks to 27% of its original area. The density increases from  $8.1\text{kg}/\text{m}^3$  to  $1070\text{kg}/\text{m}^3$ . (c) Cross-section of the micro-probe after cutting using a microtome. The scaling bar in (a) corresponds to  $200\ \mu\text{m}$ , and scaling bars in (b) and (c) correspond to  $50\ \mu\text{m}$ .

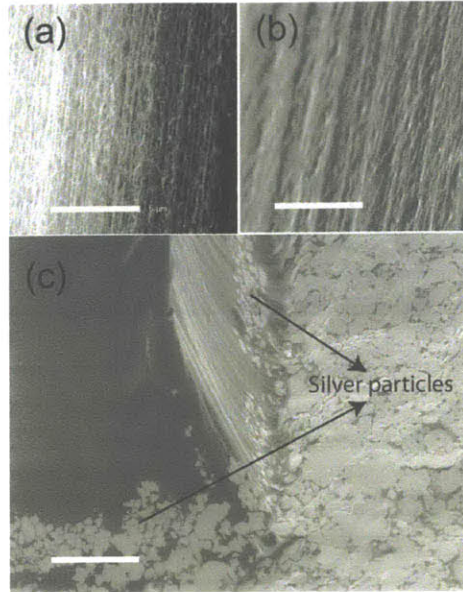


Figure 4-5: (a) SEM image of sidewall of CNT column before curing. (b) SEM image of sidewall of CNT column after curing. (c) SEM image of the bottom of a CNT column showing silver particles, which stay at the roots, and do not penetrate into the structure. The scaling bar in (a) and (b) correspond to  $5\ \mu\text{m}$ , and scaling bar in (c) correspond to  $20\ \mu\text{m}$ .

of a “honeycomb” like structure. This structure has walls with dense CNT arrays and hollow regions, which is typical of cellular structures and foams. Figure 4-4c shows top view of a column which was cut using microtome, where the shrinkage can be clearly seen as well. Figures 4-5a and 4-5b show SEM pictures of the sidewall of a column before and after curing. It can be seen that the curing process modifies the surface as well, causing the CNT-CNT spacing to decrease.

Energy dispersive X-ray analysis (EDX) performed at various locations including the sidewalls and cross-section indicates that the silver particles do not penetrate the columns and remain at the roots of the columns. As shown in Figure 4-5c, this makes sense because the silver particles are much larger than the initial CNT-CNT spacing. This observation is especially important because the silver particles make electrical contact to the ends of the CNTs, yet because the particles do not penetrate upward into the CNT pillars we expect the bulk electrical characteristics of the CNTs to be preserved.

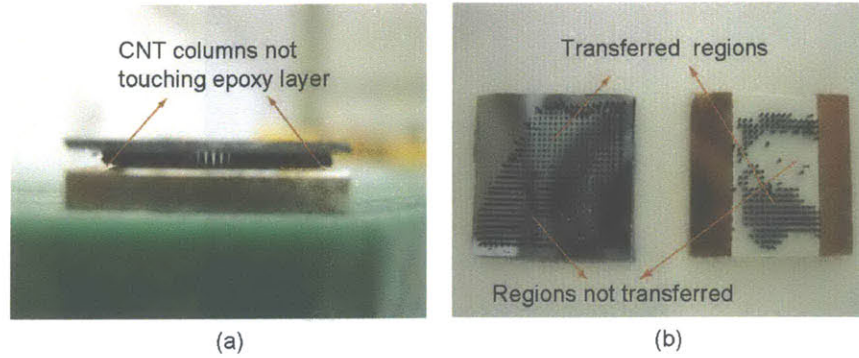


Figure 4-6: Partial transfer due to non-uniform height of as grown columns.(a) Close-up image showing the substrate with CNT columns come into contact with the transfer substrate. Due to nonuniform growth, there are regions which do not come into contact with the conductive epoxy. (b) Silicon and copper substrates after the transfer.

### 4.3 Practical Issues and Yield

As discussed in Chapter 2, growth of VA-CNTs is not uniform across a given die. There are variations depending on pattern size and density. Due to the contact printing nature of the transfer process, not all of the columns come into contact with the epoxy layer during the curing process and the process may result in partial transfer of the columns, as depicted in Figure 4-6.

### 4.4 Electromechanical Characterization

Compression tests of the CNT micro-probes are performed using the same tribometer and setup described in Chapter 3 with the addition of a 4-point electrical resistance measurement setup as shown in Figure 4-7. A column is compressed with an Au-plated ball-end steel punch ( $D = 4mm$ ), after alignment is performed using two cameras aimed perpendicular to the punch. The probes are compressed with quasi-static loading at a strain rate of  $5 \times 10^{-3} s^{-1}$ , while the applied force and time are measured. For simultaneous electrical characterization, two Au wires were attached to the steel punch and two wires to the copper substrate. This enables a 4-point resistance measurement, where current is imposed and the voltage drop across the column is measured. During compression, the probes preserve their initial cross-section and don't expand laterally. This is probably due to their porous internal structure, as depicted in Figure 4-4b ,



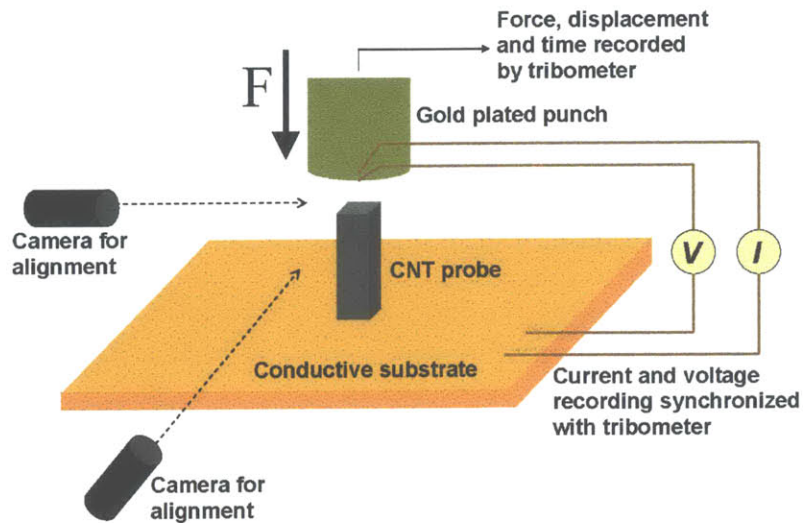


Figure 4-7: Experimental setup for electromechanical characterization of CNT columns and composite micro-probes. Applied force, and voltage drop are measured, while displacement and current are imposed.

where during the compression the hollow sections are filled with CNTs resulting from collapse of adjacent walls.

The electromechanical characteristics of the micro-probes are shown in Figure 4-8a which plots stress, strain and electrical resistance of a CNT probe during a full cycle of loading and unloading. Once the punch is brought into contact with the CNT micro-probe, the resistance starts dropping very rapidly, followed by a slower drop corresponding to a constant stiffness compression regime for which the structural stiffness is calculated to be approximately 1.23 *GPa*. If the strain does not exceed this elastic limit, the micro-probes can perform up to 200 cycle's without degradation of electrical or mechanical properties. This regime is followed by a short force relaxation period, after which the stiffness is less than that at the beginning and the resistance settles and keeps the same value until the very end of the loading. Before unloading begins, the displacement is kept constant and the force is observed. Interestingly, at this point we observed a large amount of force, which is analogous to creep. This is clearly seen in Figure 4-8b which shows time histories of stress and strain. The unloading occurs through almost the same stiffness as the initial compression, and the cycle ends with significant permanent

|                      | As-grown columns                      | Transferred columns                   |
|----------------------|---------------------------------------|---------------------------------------|
| Mass Density         | 8.1 $kg/m^3$                          | 1070 $kg/m^3$                         |
| Structural Stiffness | 0.0022 $GPa$                          | 1.23 $GPa$                            |
| CNT density          | $1.5 \times 10^{10} \frac{CNT}{cm^2}$ | $5.6 \times 10^{10} \frac{CNT}{cm^2}$ |
| Porosity             | 99.6%                                 | 98.5%                                 |

Table 4.1: Comparison of the mechanical properties of as-grown and transferred columns.

deformation.

The mechanical properties of as-grown columns and reinforced micro-probes are summarized in Table 4.1. Adding epoxy to a column increases its bulk density, calculated by dividing the mass of the column by its volume, by 3 orders of magnitude. Further, accounting for the effective cross-sectional area of the “honeycomb” we find the areal density of CNTs is increased by approximately 400%. The significant increase in bulk density is due to the penetration of the epoxy and subsequent filling and reinforcement. Figure 4-9 compares as-grown CNT columns and transferred CNT structures in an Ashby chart with conventional materials, along with aerogels. Since the transferred columns have comparable mechanical properties with conventional structures, this reinforcement scheme presents a suitable platform to characterize VA-CNTs and understand their collective behavior.

The deformation mechanism is rather complicated and is beyond the scope of this discussion. However, it is worth noting that there are significant similarities to cellular structures[42], both in terms of structure and mechanical behavior and we are currently working on a comprehensive model to understand the deformation phenomena of the columns. Furthermore, although we measure the modulus of the cured epoxy as 2GPa (as a mixture of silver particles and polymer, without CNTs), the curing process with CNTs leaves silver particles at the root and therefore we would need to measure the modulus of only the hardener as it interacts with the CNT “scaffold”. Nevertheless, we believe there are three main reinforcement mechanisms present in our results: the additional new material which is the polymer, the densification of CNTs by capillarity-induced contraction of the columns, and “bridging” among CNTs which improves load transfer within the column.

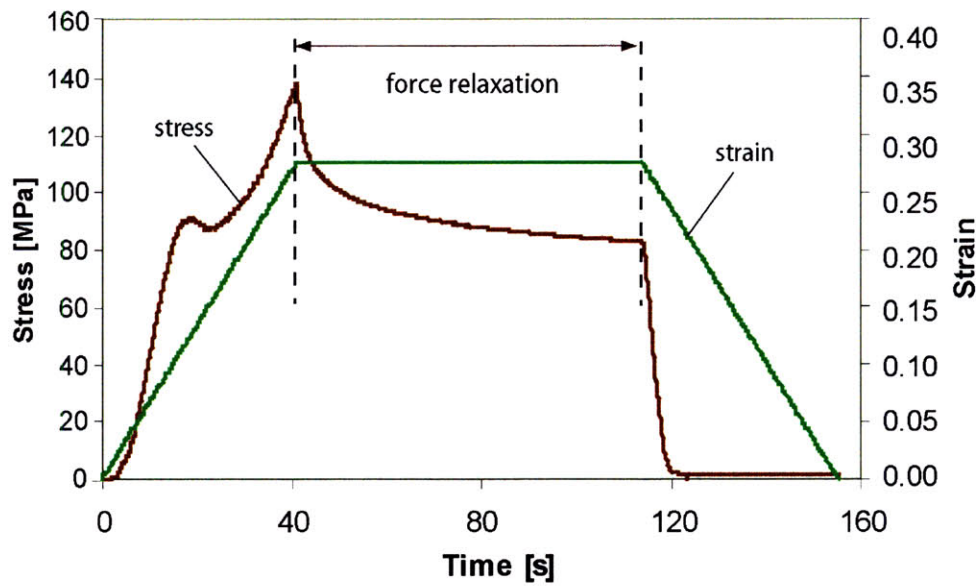
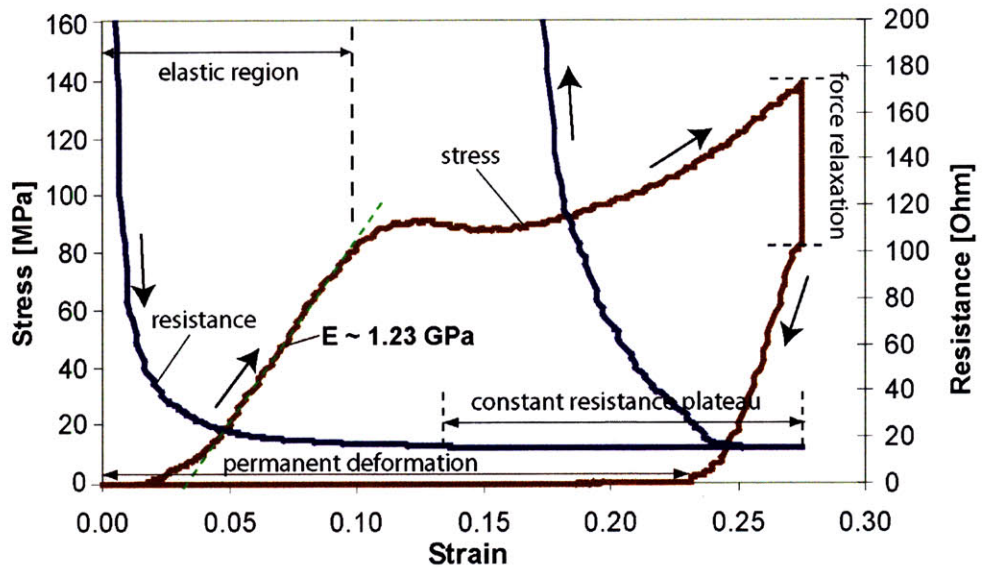


Figure 4-8: (a) Stress-strain curve and electrical resistance of a micro-probe under a full cycle of loading and unloading. Force relaxation occurs when the displacement is held constant. Note constant resistance plateau and large permanent deformation after compression. (b) Time histories of stress and strain better illustrate the force relaxation.

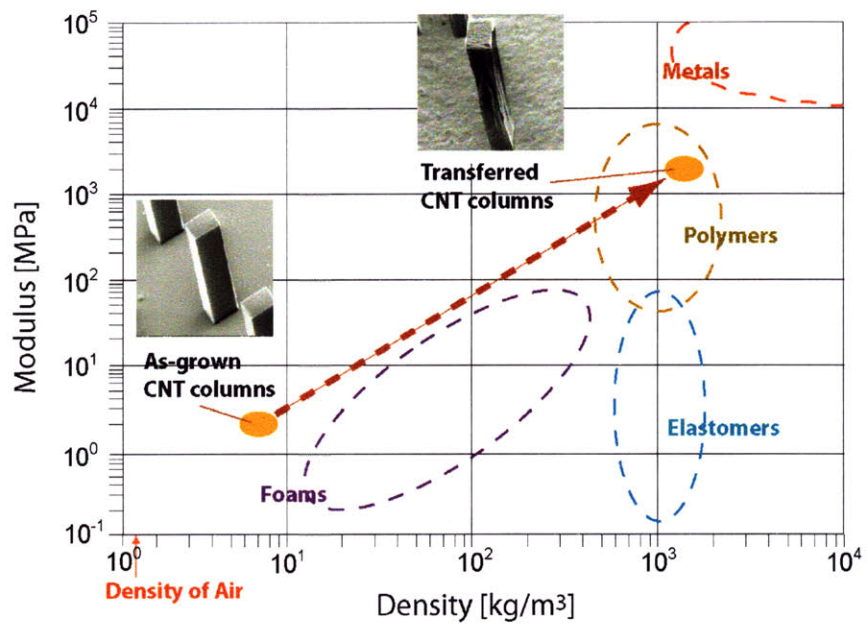


Figure 4-9: Ashby chart comparing as grown columns and transferred columns with conventional materials. Note the very low density and relatively large modulus of as grown columns.

## 4.5 Electrical Characterization Discussion

Along with theoretical studies [43, 44, 45, 46], it has been experimentally shown [47], [48] that electrical transport through CNTs is affected by strain where the conduction reduces with stretching. Tomblor et. al. and Liu et. al suggest that the conduction is reduced due to a reversible transition from  $sp^2$  to  $sp^3$  bonding configurations in the bending region, leading to a 2 orders of magnitude reduction in conductance. On the other hand, Maiti et. al. and Minot et. al. show that carbon atoms remain essentially  $sp^2$  coordinated and attribute the change in conductance to a modification in band gap of a semiconducting CNT or opening a band gap in the case of a metallic CNT (metal to semiconductor transition). There is also a wide variation in predictions of the change in conductance due to strain. All the literature mentioned above dealt with semiconducting or metallic single walled carbon nanotubes. A recent study [49] demonstrated the opposite behavior for multi walled carbon nanotubes, where the conductance increases drastically upon compression or bending. The authors attribute this behavior to increasing number of conduction channels in the nanotube and parallel transport through them. In the experiments presented here a reduction in resistance was observed as the carbon nanotubes are compressed and bent which is expected as the structures are also composed of multi walled carbon nanotubes.

The lowest resistance obtained for a  $200\mu m \times 200\mu m \times 700\mu m$  column which has approximately  $5 \times 10^6$  CNTs is  $6\Omega$  (at the constant resistance plateau region). Assuming that CNTs behave as parallel resistors, the resistance of an individual CNT can be calculated from the total resistance using:

$$R_{CNT} = nR_{total} \quad (4.1)$$

where  $n$  is the number of CNTs in the bundle. This corresponds to an individual CNT resistance of  $30M\Omega$ . A comparison of this work and selected literature presenting resistance measurements of CNT bundles of comparable geometry is presented in Table 4.2. The value found above is lower than other reported values, suggesting the transfer process makes good electrical contact to large numbers of CNTs in parallel. However, this comparison is highly qualitative given the lack of standardized test methods for electrical testing of CNTs, as well as

| Reference              | CNT bundle length | Resistance per CNT          |
|------------------------|-------------------|-----------------------------|
| Agrawal et al.[50]     | 100 $\mu m$       | $10^{12} \Omega$            |
| Zhu et al.[51]         | 215 $\mu m$       | $2.9 \times 10^{11} \Omega$ |
| Yun et al.[7]          | 4 $mm$            | $1.1 \times 10^8 \Omega$    |
| Reinforced CNT columns | 700 $\mu m$       | $3 \times 10^7 \Omega$      |

Table 4.2: Comparison of individual CNT resistance for vertically aligned CNT bundles at comparable scales. It should be noted that resistance values include both contact and bulk resistance; hence we the values are not normalized with respect to bundle length.

differences among CNT growth processes which introduce variations among the structural and electrical characteristics. Also the contributions of contact resistance and bulk resistance to the total resistance measured for the CNT micro-probes should be isolated. Going forward, this process provides a versatile platform for anchoring, electrically contacting and mechanically reinforcing parallel groups of nanostructures on a wide variety of substrates, and for evaluating their electromechanical properties for device applications.

## Chapter 5

# Hybrid Metal-CNT

# Electromechanical Probes

### 5.1 Strategies for Probe Design and Manufacturing

As discussed in Chapter 4, the resistance of transferred columns are around 10 Ohms, the lowest value measured being 6 Ohm, for a typical CNT probe size ( $200\mu m \times 200\mu m \times 700\mu m$ ). These resistance values are not acceptable for most probing applications where much lower values, and in some cases sub 1 Ohm resistance values are desired. In addition to this, the yield issue discussed in previous chapter along with the penetration of the epoxy material into the structure and changing the mechanical properties of the CNT structures, makes the transfer method less attractive for a scalable process where predictability and robust design is very important. These considerations led to the idea of externally modifying electrical properties of CNT columns by metal deposition directly onto the surface of the columns.

Figure 5-1 depicts possible strategies for electromechanical probe design. Both of the strategies are hybrid metal-CNT designs which uses CNT columns as the main elastic structural element and outside metal coating as the main electron carrier. For the scenario where as-grown columns are used as the probes, CNT structures resulting from the floating catalyst CVD growth are much better candidates due to their larger structural stiffness, which would be much suitable for smaller size columns necessary for lower pitch applications. As discussed, as-grown CNT structured fabricated using the fixed catalyst method can be utilized in the

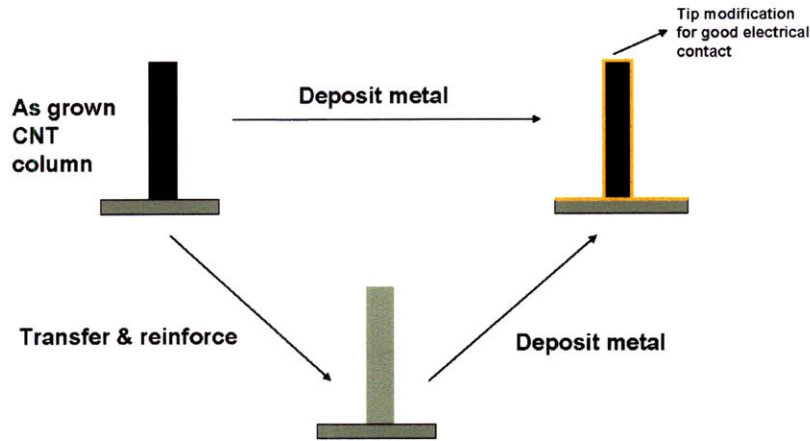


Figure 5-1: Strategies for electromechanical probe design and manufacturing.

second scenario, where the columns are reinforced through the transfer process. However, due to reasons discussed in Chapter 4, this method is not very reliable in terms of yield and not very predictable in terms of mechanical properties. The rest of the chapter will concentrate on the first scenario where CNT structures grown with floating catalyst recipe is utilized.

## 5.2 Metal Deposition Techniques

This section investigates two metal deposition techniques onto CNT structures, namely electroless plating and sputtering.

### 5.2.1 Electroless Plating

Electroless plating is a technique which enables metal deposition from a solution onto conductive surfaces without external current flow provided by electrodes. CNT films grown with both fixed and floating catalyst technique were plated with  $Pd$  where the CNT film along with the growth substrate is dipped into a solution whose content is summarized in Table 5.1.

The plating solution is heated to  $50^{\circ}C$ . At this temperature the hypophosphite begins to oxidize on any conducting surface. The released electrons then reduce the  $Pd^{2+}$  from solution onto any area electrically connected to the surface that accepts the electrons from the hypophosphite. At higher temperatures or higher concentrations of hypophosphite the  $Pd$  can



|   | Bath volume:1000 ml |           |
|---|---------------------|-----------|
| Solution heated to 50°C to start deposition | Target              | Qty. req. |
| 27 wt% $NH_4OH$                             | 250 ml/l            | 250ml     |
| Ammonium Sulfate                            | 31 g/l              | 31g       |
| Sodium hypophosphite                        | 10g/l               | 10g       |
| PC1 Pd make up powder                       | 4g(Pd)/l            | 57ml      |
| Water                                       |                     | 693ml     |

Table 5.1: Contents of the solution used for electroless plating of Pd onto CNT films.

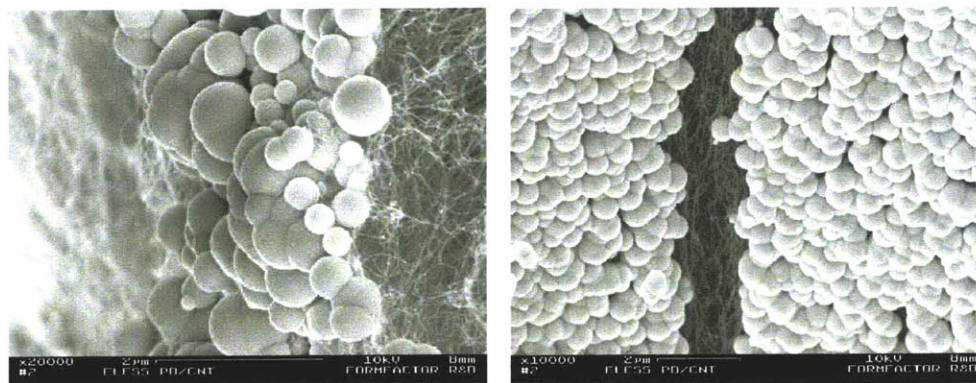


Figure 5-2: SEM images of electroless plated Pd on CNT films grown with fixed catalyst CVD method.

spontaneously reduce in solution. At this point all surfaces will coat as well as the formation of black colloidal  $Pd$  particles in the solution. Once the formation of  $Pd$  particles occurs then there the solution will continue to decompose on the  $Pd$  particles until either the  $Pd^{2+}$  or hypophosphite is consumed. It is important to carefully time the process and pull the CNT films out of the solution before  $Pd$  particles start reducing into the solution. This point is not very repeatable and sensitive to a lot of process parameters such as bath temperature, which makes the film thickness control difficult.

Figure 5-2 show electroless plated Pd film on CNT film grown with the fixed catalyst CVD method. The main observation with this deposition technique is that due to the nature of the deposition process, metal particles start forming small islands on the surface of the CNT film and keep growing off of those islands, forming metal "*spheres*". The deposition technique also results in intrinsic film stress as depicted on Figure 5-3 where electroless plated Pd film on

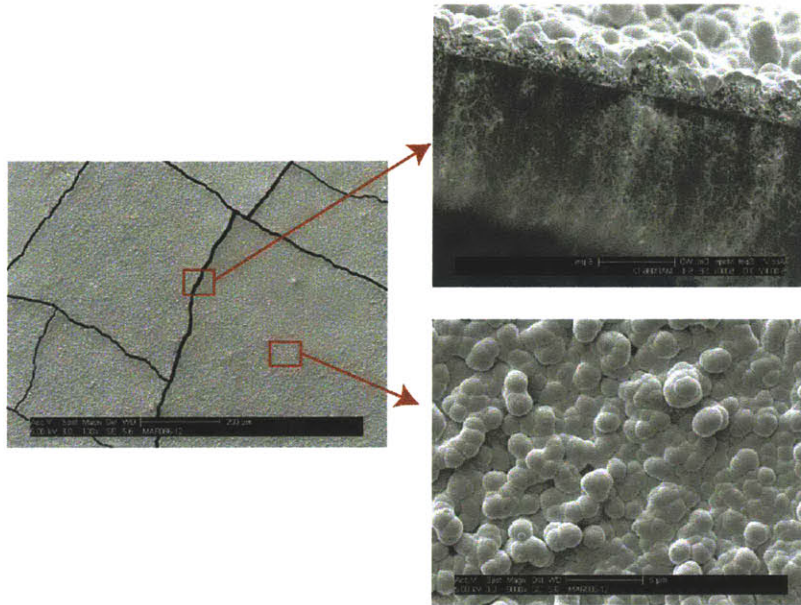


Figure 5-3: SEM images of electroless plated Pd on CNT film grown with floating catalyst CVD technique. Electroless depositions results in intrinsic stress.

CNT film grown with the floating catalyst CVD method forms cracks and peels off at various locations. The electroless plated film is continuous and has good adhesion to the CNTs, as can be seen in Figure 5-3, where during peeling off from the film, the film pulls CNTs along.

### 5.2.2 Sputter Deposition

Various metals including Ti, Pd and Au were deposited with DC magnetron sputtering method onto CNT films grown by both fixed catalyst recipe and floating catalyst recipe. All depositions were done at  $1.5mTorr$  pressure and  $300W$  power for Au, and  $500W$  for Pd and Ti. To understand the deposition stages, CNT films were partially covered with a shadow mask which were spaced approximately  $1mm$  above the film to enable the sputtering process deposit various thicknesses across the boundary of the shadow mask and thereby simulating the film evolution.

Figure 5-4 shows the Pd film evolution onto the CNT film grown with fixed catalyst CVD method. It can be easily seen that the Pd particles cover individual CNTs and gradually make them thicker. This is attributed to the high diffusion of the Pd particles during the

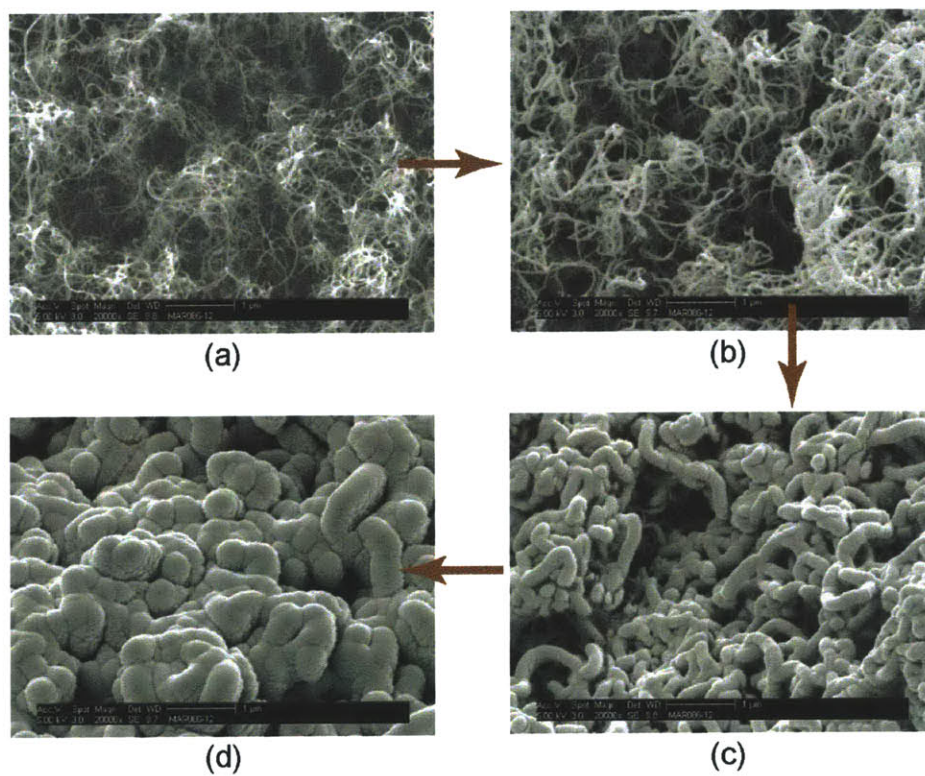


Figure 5-4: Film evolution during sputter deposition of Pd onto CNT film grown with fixed catalyst CVD method.

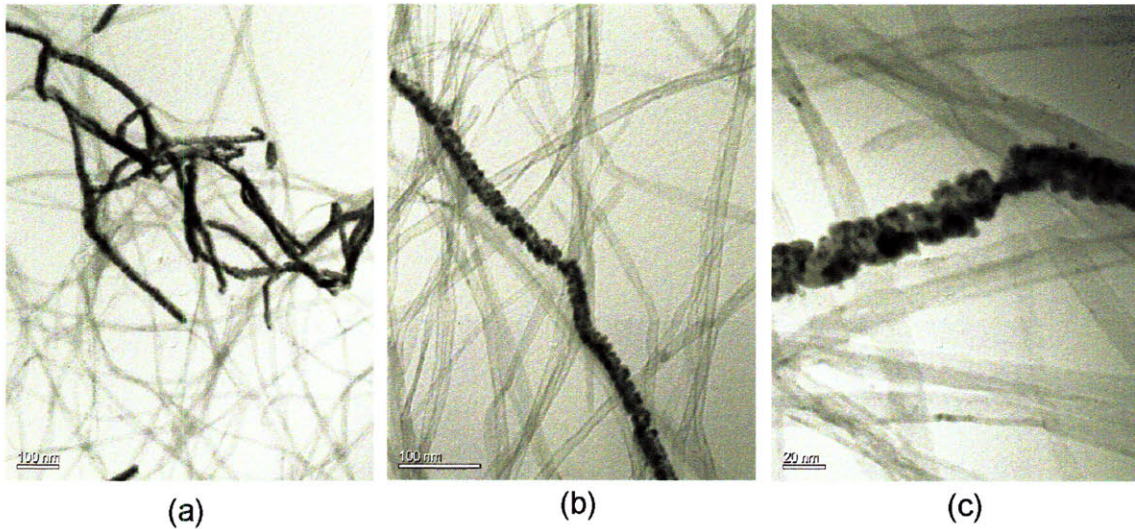


Figure 5-5: TEM images of Pd sputtered CNTs showing full coverage.

sputtering process. The resulting metal film is continuous without significant intrinsic stress. The deposition also provides good adhesion between the metal film and CNTs mainly due to the fact that individual CNTs are coated fully with metal on the surface of the film. The sputtered films are also continuous and no intrinsic stress was observed.

The coverage of individual CNTs by the Pd particles is verified with TEM investigations. Figure 5-5 shows TEM images of CNTs covered with Pd particles confirming the observations made with SEM. These findings indicate that metal sputtering onto CNT structures can be an attractive candidate for scalable applications.

Similar results are obtained for the case of CNT films grown with floating catalyst technique. Figure 5-6 demonstrates that metal sputtering also works for larger CNTs resulting from this method.

### 5.3 Probe Development

As mentioned earlier, minimal interference with the mechanical properties is key for the choice of the metal deposition method. Other requirements are good wetting of CNTs, ability of formation of films thick enough for the desired electrical performance, and scalability. In addition,

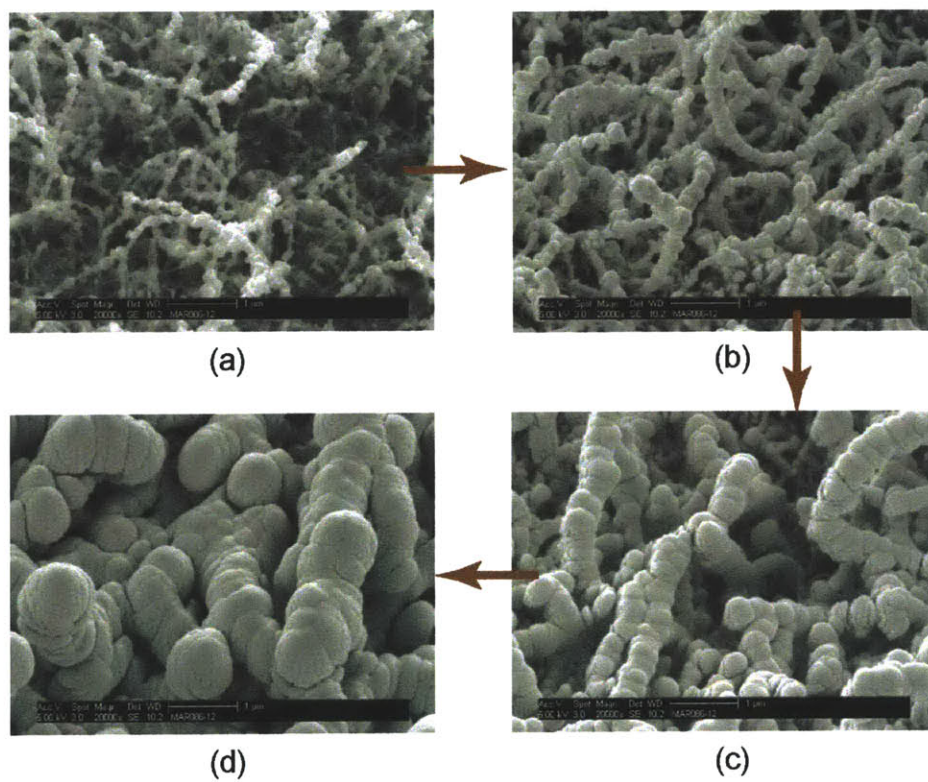


Figure 5-6: Film evolution during sputter deposition of Pd onto CNT film grown with floating catalyst CVD method.

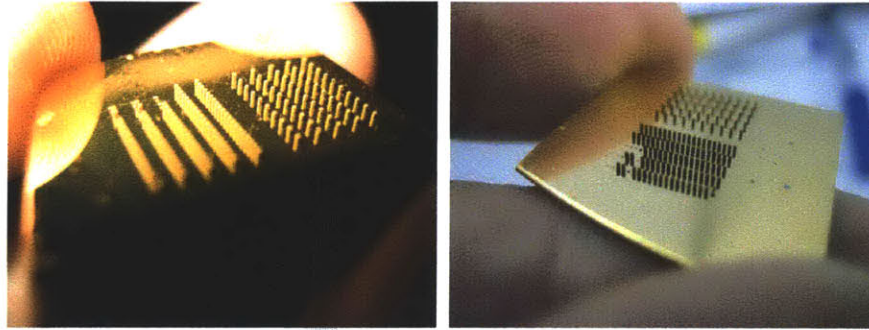


Figure 5-7: Pictures of hybrid metal-CNT probes.

it is preferable to have a dry deposition process any liquid penetration and capillarity effect from happening within the CNT structure. Considering all of the criteria just mentioned, sputtering technique is a much stronger candidate mainly due to its dry nature. This method also provides good coverage of individual CNTs on the surface, is scalable and enables batch fabrication of thousands of CNT columns in one deposition run.

As the metal for deposition onto CNT probes, Au was chosen due to the fact that it is a noble metal and will provide consistent results for a given probe where oxidation over time can increase contact resistance significantly. As mentioned in Section 5-1, the hybrid-CNT probes are manufactured with the floating catalyst CVD method. Figure 5-8 shows hybrid metal-CNT probes of various areas and pitches. There is good metal coverage on all surfaces of the probes. To investigate the sidewall coverage in more detail, CNT columns were sputtered for different durations as shown in Figure 5-9. The resulting evolution is similar to the one obtained with vertically spaced shadow mask where again individual CNTs are getting thicker as the deposition continues.

It is important to know the metal film thickness around the CNT column to predict electrical resistance. Hence, it is crucial to understand how deep the sputtered metal penetrates into the CNT columns. To investigate this, metal deposited CNT columns are cut with focused ion beam (FIB) to be able to see the cross-section and measure the metal film thickness. Figure 5-10 demonstrates FIB cutting technique and the resulting interface.

Figure 5-11 depicts two cases where columns were deposited for different durations, namely

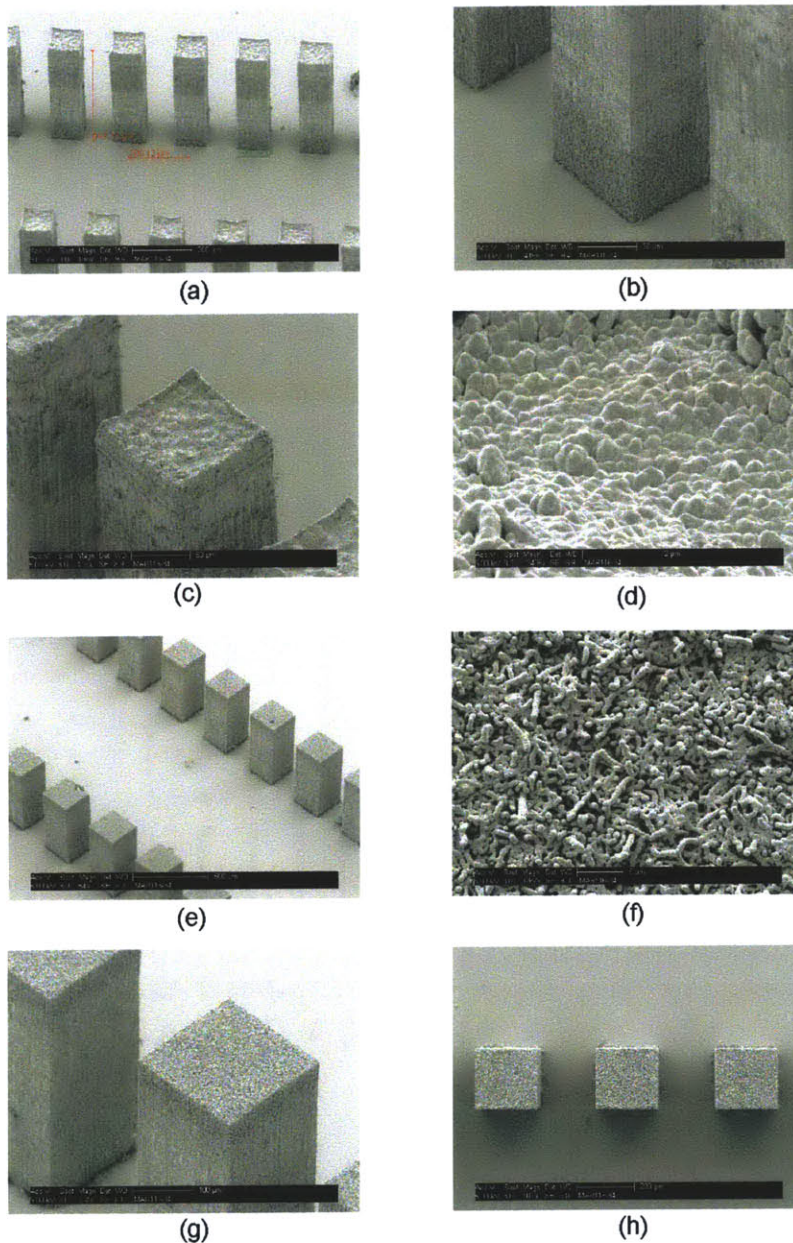
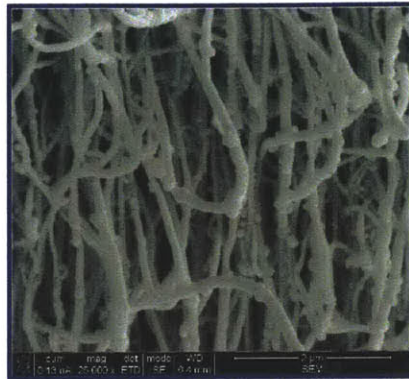
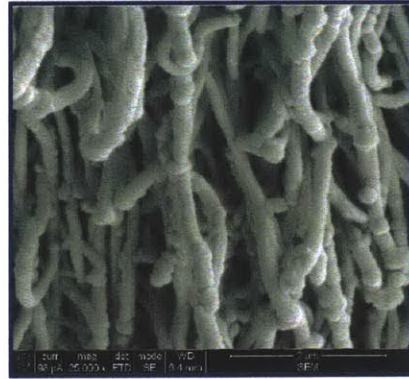


Figure 5-8: Hybrid electromechanical probes made by sputtering Au onto CNT columns grown with floating catalyst CNT method. (a-d)  $200\mu\text{m}$  pitch square columns sputtered with Au for 24 minutes. (e-h)  $400\mu\text{m}$  pitch square columns sputtered with Au for 12 minutes. (d) and (f) are close-up images of the top surfaces of the sputtered CNT columns. Even though the main difference is the sputter time, it is easy to note that the top surface of the larger columns are much smoother, which is a result of the growth process, particularly the termination of the growth and total growth time. The two different size columns were grown at separate CVD runs.



**4 min.**



**8 min.**



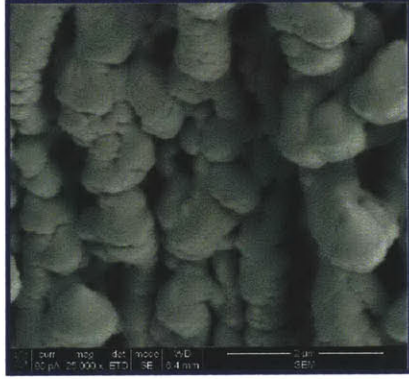
**12 min.**



**16 min.**



**20 min.**



**24 min.**

Figure 5-9: CNT side-wall coverage after different durations of metal sputtering.



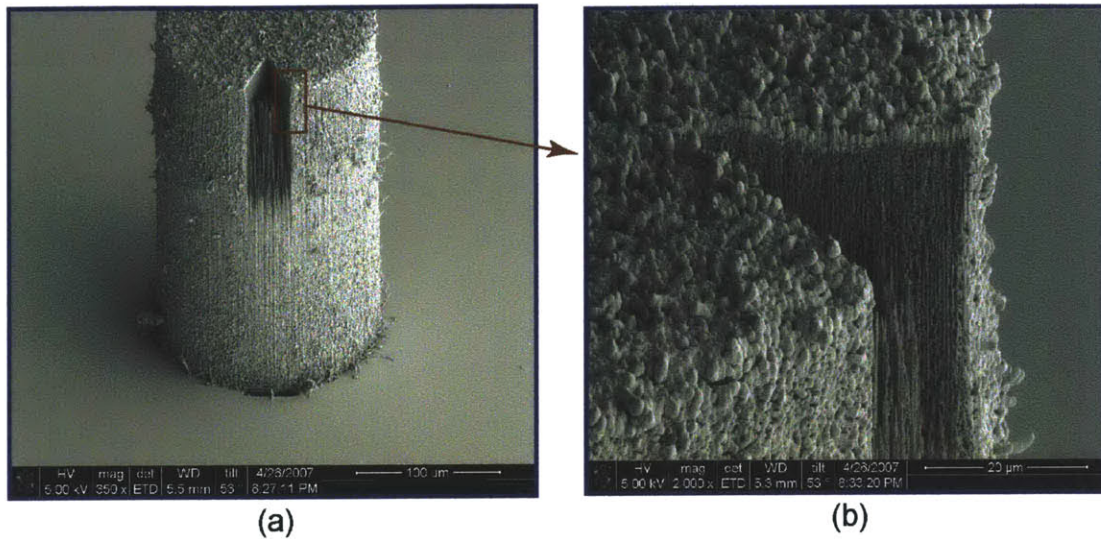


Figure 5-10: Au sputtered CNT column cut with FIB to observe Au penetration into the structure.

for 4 minutes and 24 minutes. As expected, the penetration of the metal particles into the structure is the same for both cases. As the metal particles deposit onto the film the CNTs get thicker. At a certain point, the thickened CNTs start touching each other and form a continuous film blocking new arriving metal particles and stopping further penetration. Beyond this point, as the sputtering process continuous, the additional material keeps increasing the thickness of the metal film on the CNT film.

## 5.4 Electromechanical Characterization

Hybrid metal-CNT electromechanical probes were characterized with the same setup described in Figure 4-7. Figure 5-12 shows the cyclic electromechanical performance of a probe with 200  $\mu\text{m}$  diameter with approximately 1  $\mu\text{m}$  Au coating. This is an important demonstration as these structures are the first fully functional electromechanical probes made fully of CNTs. This probe was demonstrated to perform reliably for 6000 cycles, after which the performance started degrading, where the stiffness of the CNT structure started decreasing and the electrical resistance of the probe started increasing due to failure mechanisms discussed in the next

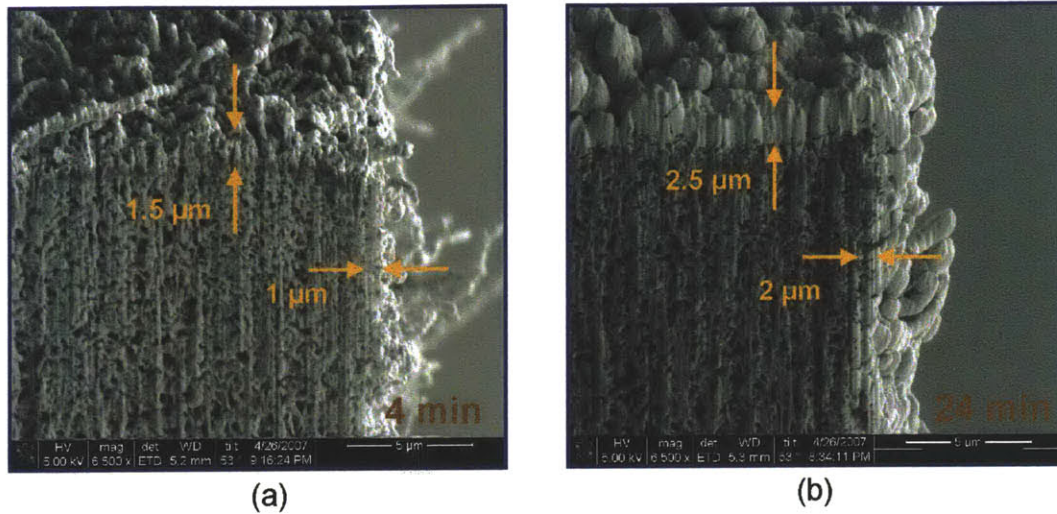


Figure 5-11: Close-up SEM images of sections of Au sputtered CNT columns cut with FIB. (a) Sputtered film penetration after 4min. of Au deposition. (b) Sputtered film penetration after 24 min. Au deposition.

section.

Figure 5-13 compares the resistance of the outer Au layer for two different porosities, namely 90% and 99%, assuming that the metal shell conduction scales with the porosity of the CNT structure. Performance of the CNT probes for two cases, namely the one shown in Figure 5-12 and another one where the Au coating is almost 2 μm thick, fall in between these two cases. However, it should be noted that the conduction mechanism is rather complicated and these two assumptions present limit cases.

## 5.5 Failure Mechanisms

As cyclic operation and many touch-downs are very critical for realistic industrial applications, it is important to understand failure mechanism of the hybrid metal-CNT probes. Figure 5-14 depicts the most common failure mechanisms observed after operation.

The most drastic, but not very predictable, failure mechanism is the failure of the contacting section, where the top surface comes off and loses electrical contact with the rest of the column completely. This failure is not very consistent and not observed in all probes. The likelihood of

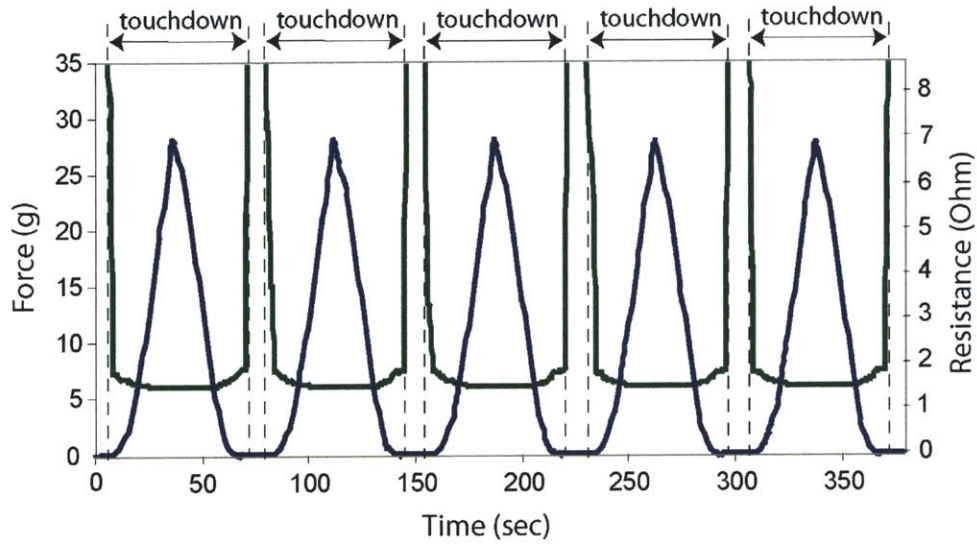


Figure 5-12: Performance of a  $200\mu\text{m}$  diameter hybrid metal-CNT probe under cyclic load.

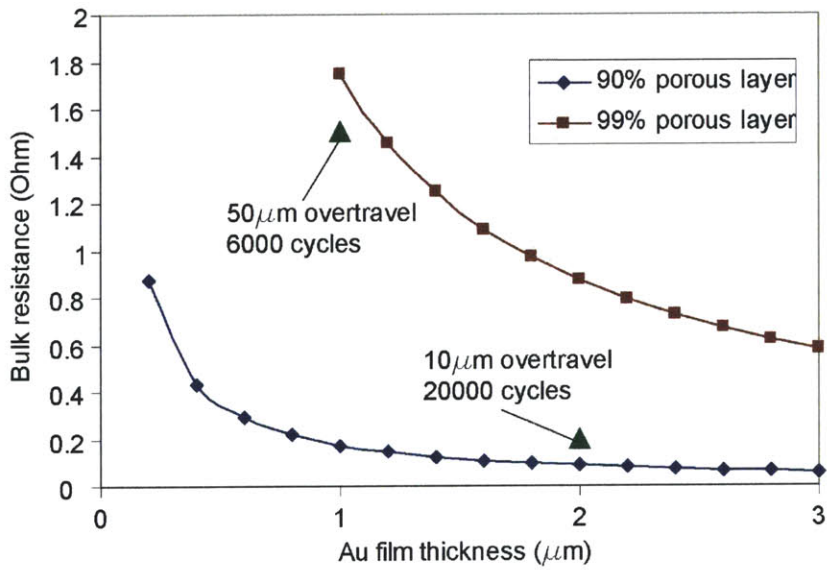


Figure 5-13: Electromechanical probe performance and comparison with two different porosity outer metal shell.

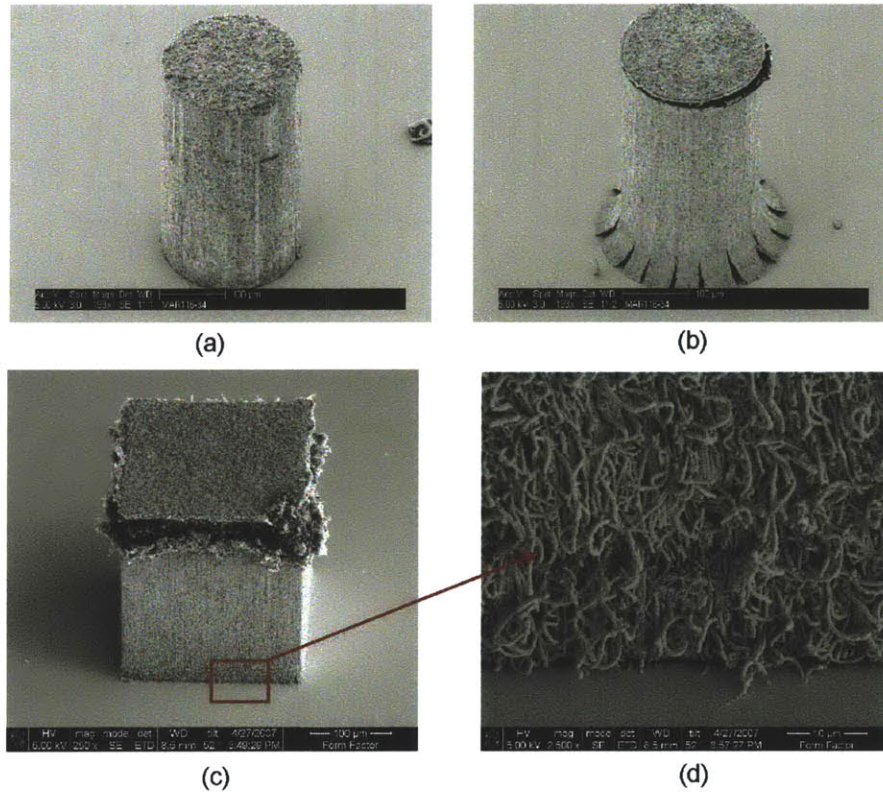


Figure 5-14: Failure mechanisms observed during deformation hybrid CNT-Au electromechanical probes. (a) A circular Au sputtered (24min) column before deformation. (b) Same column after deformation showing failures at the top and bottom. Due to the thick top Au layer, as well as due to the inherent property of the top surface resulting from the termination of the CVD process, the top "cap" comes off. The outer metal layer also peels off at the bottom where the buckling and deformation occurs. (c) A square column shown after deformation where the top cap comes off, but the bottom section failure is not as drastic. (d) Close up image of the bottom section showing traces of deformation, but experiments show that electrical continuity is maintained due to the large number of CNTs remaining in contact.

this failure increases with the thickness of the metal layer, but significant differences between different batches of CVD growth has been observed, which makes it difficult to distinguish contributing factors to the failure mechanism. Some CNT columns have rough top surface, such as in Figure 5-8c, and some have smooth top surface, such as in 5-8g. It is believed that this difference is a consequence of the total growth time, and particularly the nature of the growth termination, that is if the growth has been terminated by stopping the growth process or if the growth stops naturally even though the supply of gasses and catalyst continues. This is still an active research area.

The other failure mechanism is the formation of discontinuities in metal shells surrounding individual CNTs, mainly caused due to large strain deformations during probe operation. However, this mechanism does not cause significant increase in the resistance as there are so many metal covered CNTs that even though there is no continuity along one given CNT, continuity is achieved by contacting thousands of metal covered CNTs.



## Chapter 6

# Other Applications: Nano Art

CNT structures along with some of the tools used throughout this thesis present an interesting platform for nano/micro art. The following pages compile some of the interesting SEM images taken during research while performing compression tests on CNT structures or working with techniques like focused ion beam, sputter etching, metal sputtering and metal deposition with electroless plating onto CNT structures. All of the pictures are pure scanning electron microscope images without any post processing or editing in any format.

Controlled buckling presents an interesting tool where regular bellow shaped structures can be created and controlled with compression amount (Figures 6-1, 6-2, 6-3). Etching techniques like focused ion beam (Figures 6-4 and 6-5), sputter etching (Figure 6-6), or reactive ion etching, where the film surface, the CNTs in this case, are bombarded with ions or particles, yield a very interesting phenomena resulting in sharp CNT structures. This is mainly caused by the high porosity of the CNT structures and some of the particles penetrate more than the others and create this nonuniform etch pattern resulting in sharp CNT tips. And finally, metal deposition onto CNT structures yields interesting observations, as discussed in Chapter 5, such as full coverage of a CNT surface with metal particles and formation of "worm-like" structures (Figures 6-7), or electroless deposition where metal particles form small islands and then larger spheres (Figure 6-8). Also, a combination of these tools and methods can be used to modify CNT structures, or the surface of the CNT film to create various art-work.

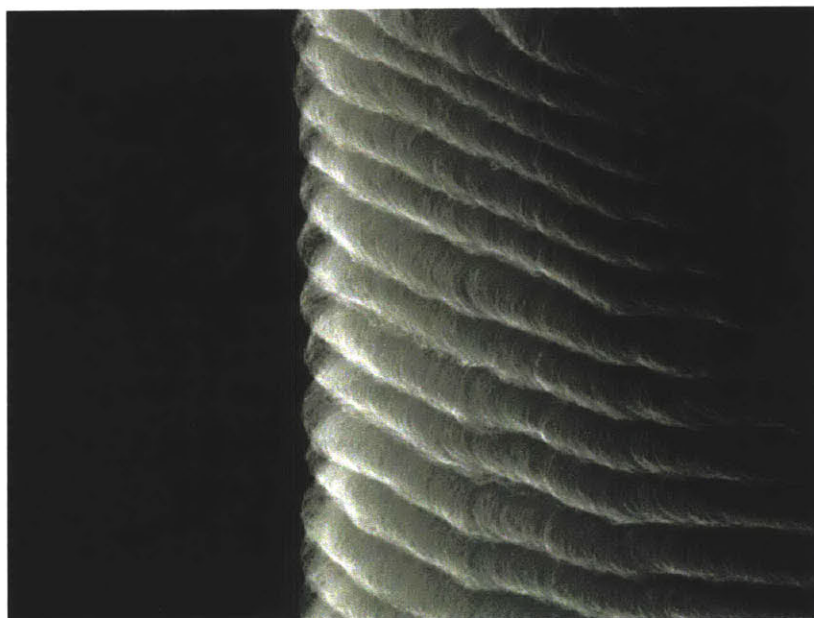
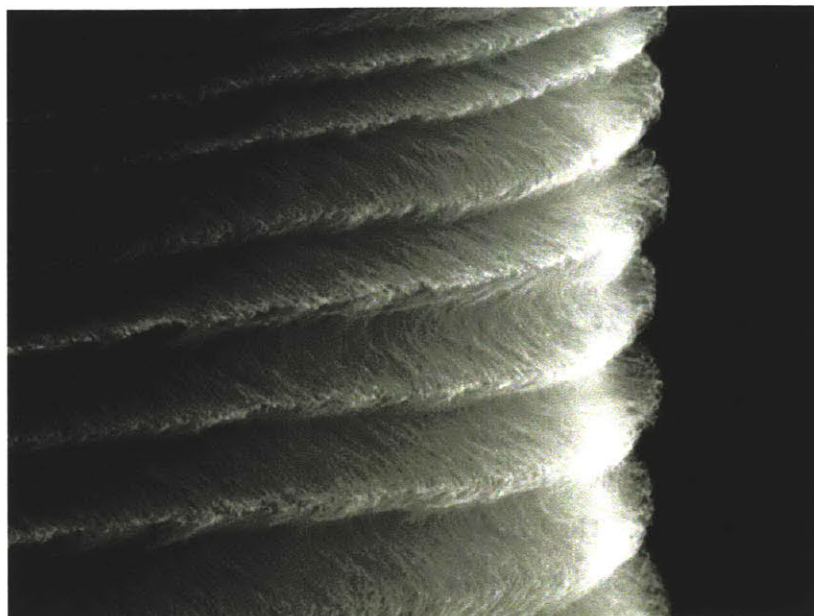


Figure 6-1: Controlled buckling of CNT structures.



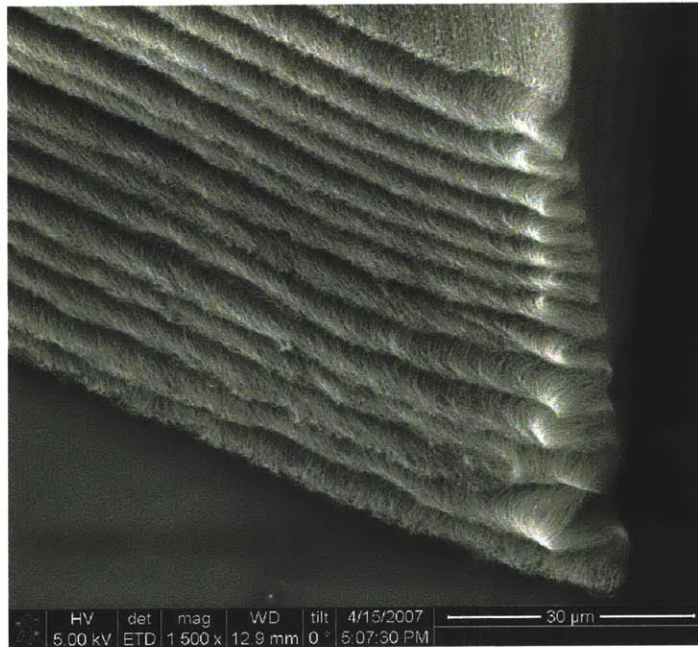
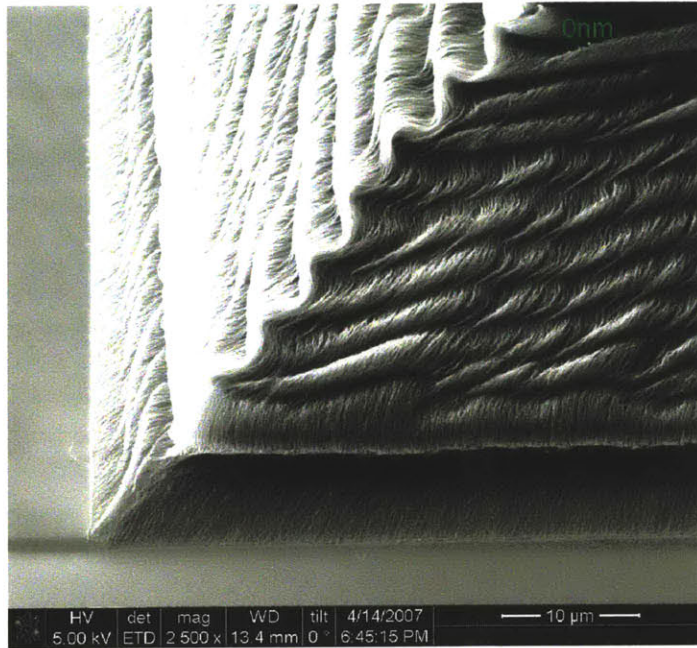


Figure 6-2: Controlled buckling of CNT structures.

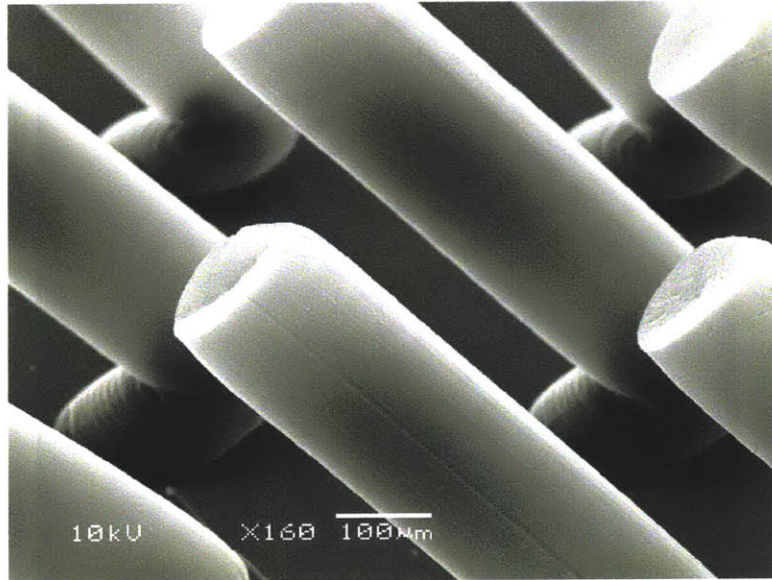
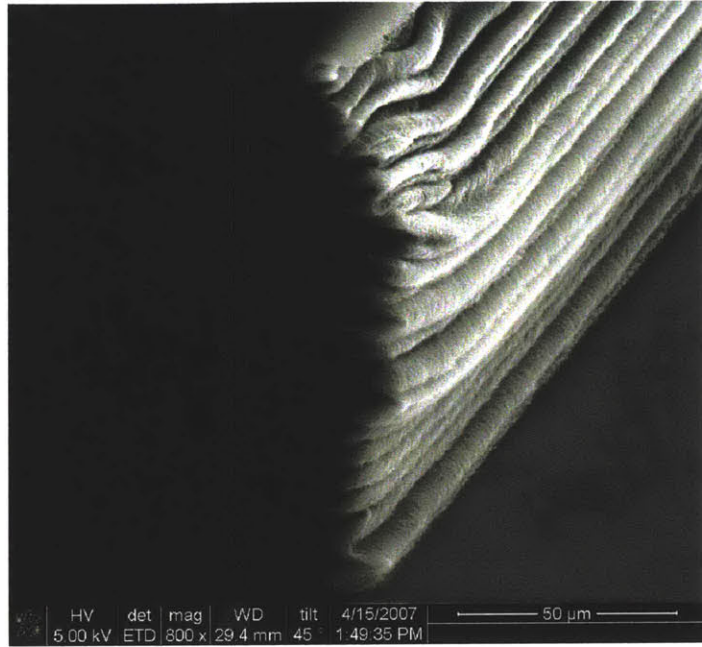


Figure 6-3: Controlled buckling of CNT structures.

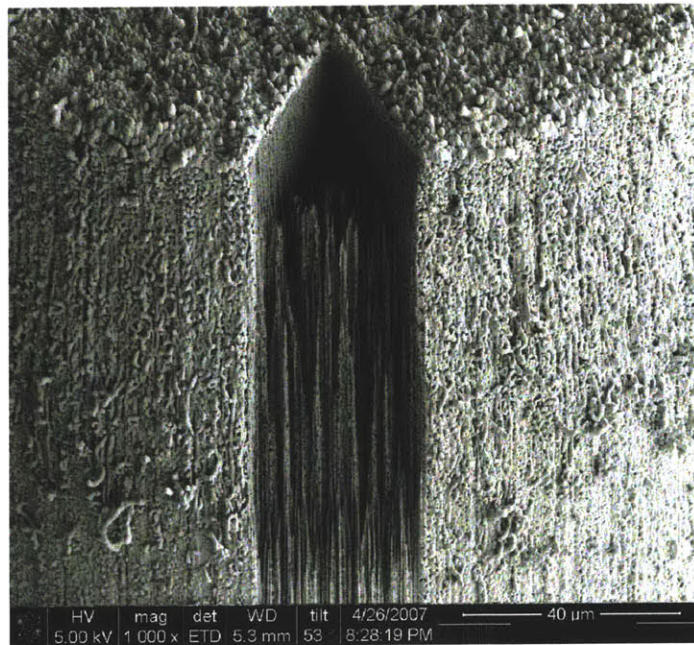
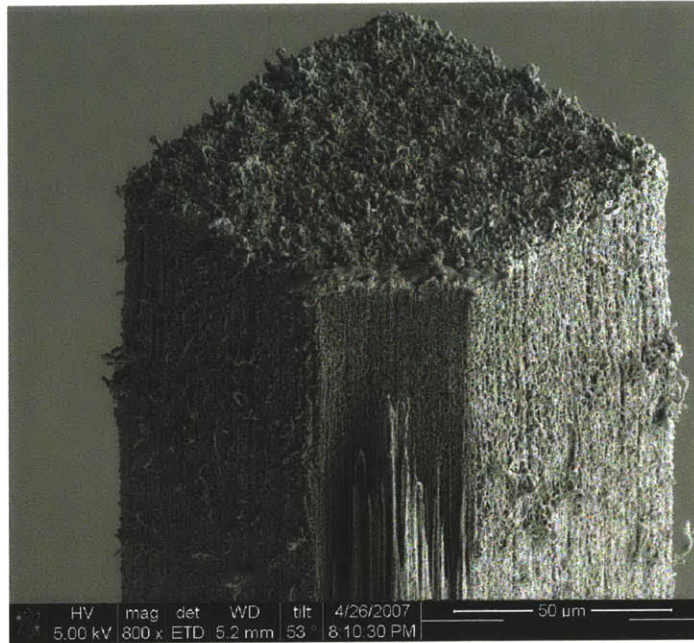


Figure 6-4: Focused ion beam (FIB) cutting and etching of metal-CNT hybrid columns.

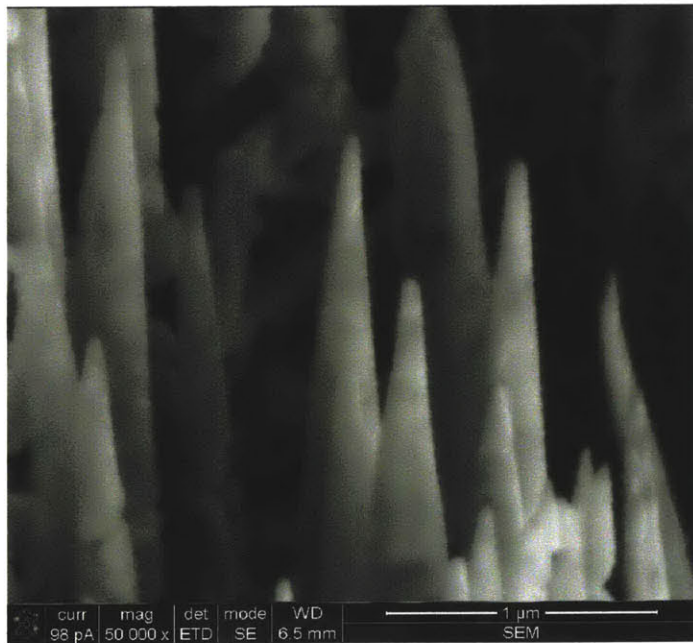
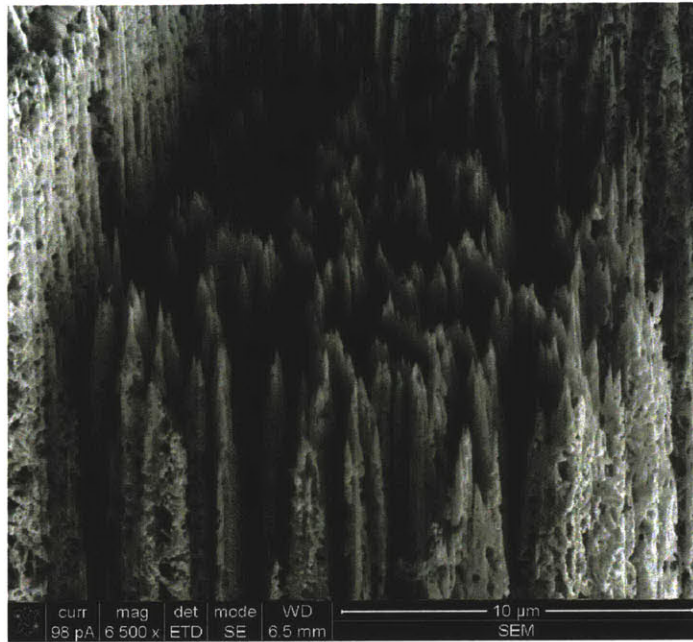


Figure 6-5: FIB cutting and etching of CNT structures.

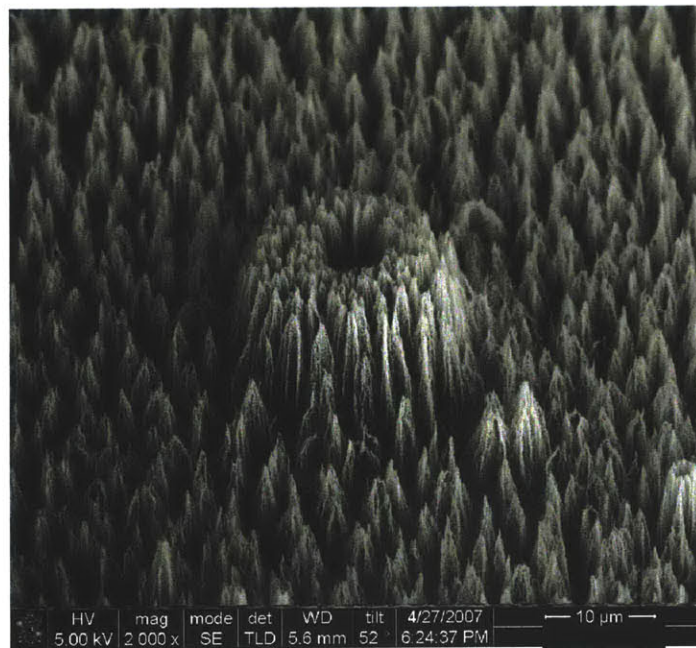
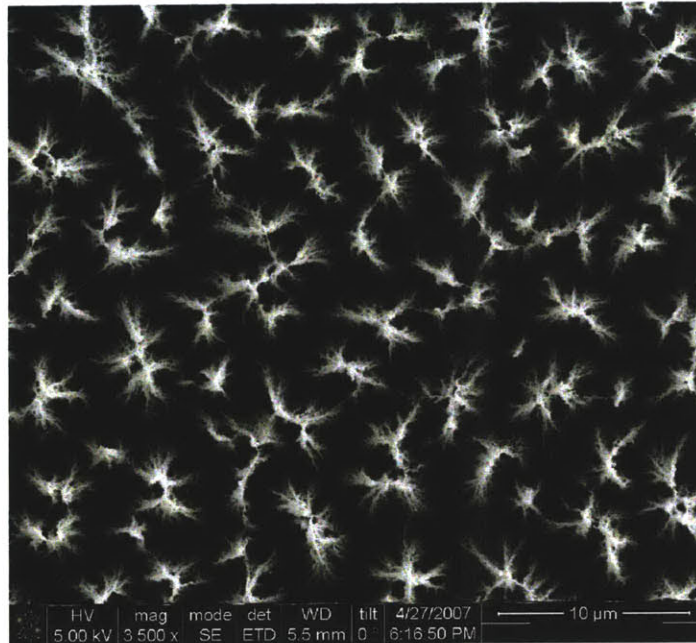


Figure 6-6: Sputter etching of CNT film.

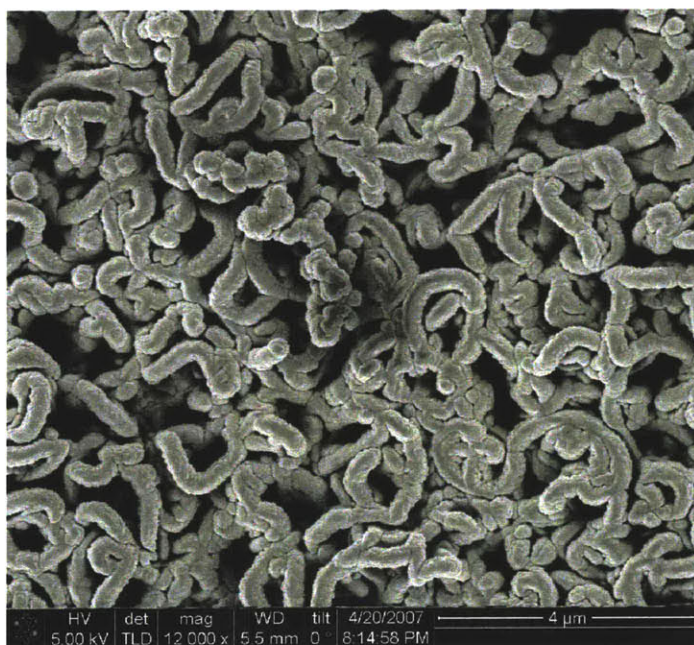
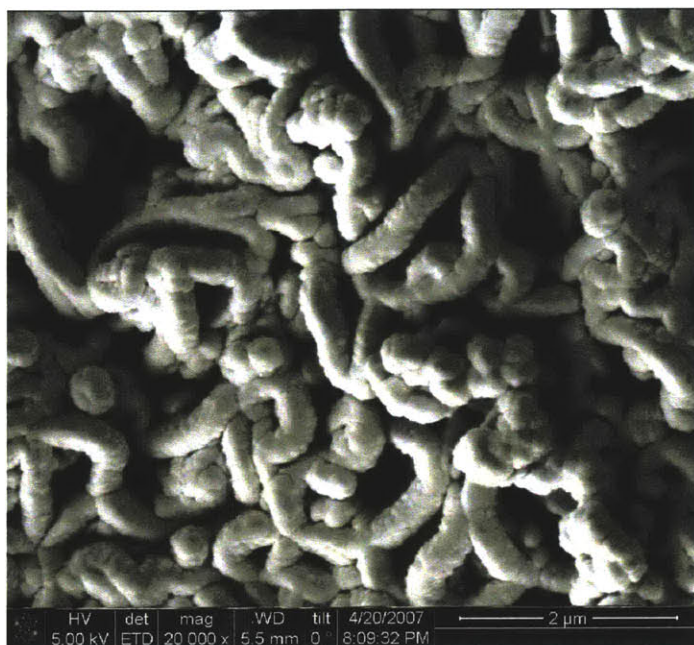


Figure 6-7: Sputtered Au onto CNT film.

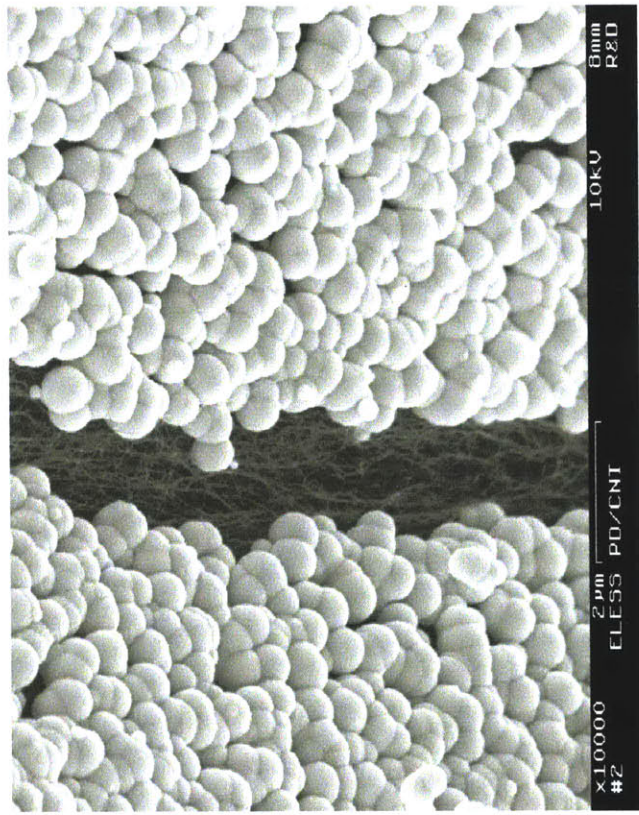
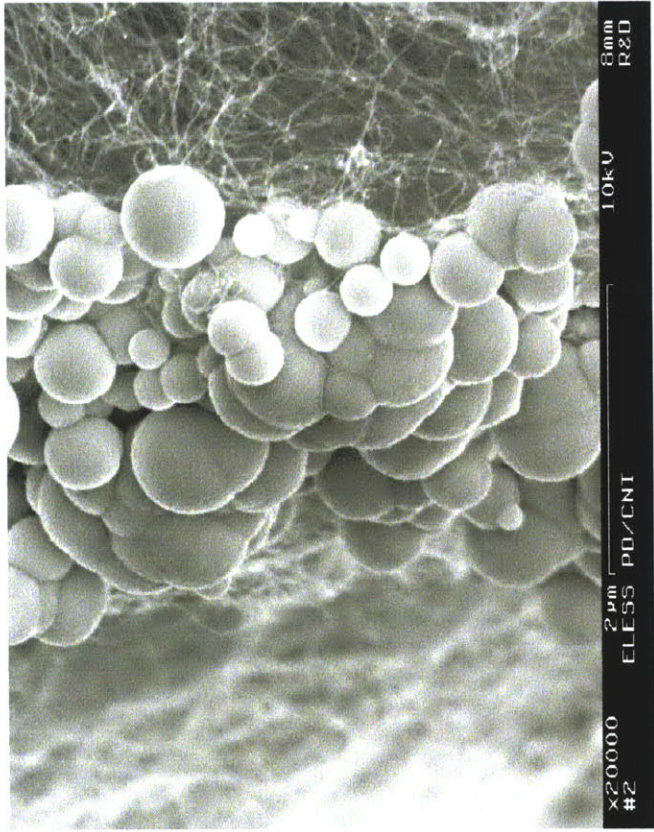


Figure 6-8: Electroless plating of Pd onto CNT film.





## Chapter 7

# Conclusions and Recommendations for Future Work

### 7.1 Summary

The main objectives of this thesis were to:

- Gain insight into the deformation mechanism of structures made of vertically aligned CNTs.
- Relate growth conditions to inherent CNT properties and final mechanical properties of CNT structures.
- Develop design tools for CNT structures to be used as electro-mechanical probes.
- Develop methods for improved electrical conduction and adhesion to substrate.

Chapter 1 presented a brief overview of the CNT technology and motivated the current work for electromechanical probing applications.

Chapter 2 presented a comprehensive comparison of various CVD growth techniques and growth issues relevant to probing applications such as nonuniform growth, size dependent growth and loading effects, growth rate variation and other process control issues which might impact batch production of CNT probes.

Chapter 3 provided a comprehensive discussion of systematic mechanical characterization of CNT columns. CNT column grown with the fixed catalyst CVD method showed a very unique deformation mechanism which allowed the tuning of the stiffness by controlled compression, which resulted in controlled buckle formation. It was shown that each buckle was performing like an elastic bellow and added a new spring in series with the existing spring, thereby reducing the overall stiffness of the structure. Further stiffness tuning ability was demonstrated when columns grown with the same fixed catalyst recipe, but with hydrogen flush during ramp time showed 4 times stiffness increase. Columns grown with floating catalyst recipe performed as elastic springs and didn't demonstrate controlled buckling phenomena observed with the fixed catalyst recipe. It was found that they are much stiffer, almost 75 times as the columns with the fixed catalyst recipe without hydrogen flush. This is attributed to the very large diameters resulting from the floating catalyst recipe ( $\sim 90nm$  vs.  $\sim 25nm$ ).

Chapter 4 presented a versatile transfer printing technique which was used to transfer as-grown CNT columns onto conductive substrates. The purpose was to overcome the problem of weak adhesion to the growth substrate as well as to make electrical connection to the base substrate as the support layer ( $Al_2O_3$ ) used during growth is insulating. Due to the penetration of the epoxy material used, the transfer process resulted into simultaneous stiffening and densification of the CNT structures. Electrical measurement reveals resistance values which were too high for the particular application of interest.

Chapter 5 presented a scalable metal coating technique, namely sputtering, to overcome the high resistance problem which was one of the most important outcomes of Chapter 4. TEM investigations revealed that sputtering process results in full coverage of CNTs on the surface of the probe. Various deposition times were analyzed and focused ion beam was used to cut slices from the sides of coated columns to investigate metal penetration into the columns. It was discovered that metal penetration after a certain deposition time stops as the CNTs on the surface get thicker and avoid the new arriving metal particles to penetrate into the structure. Fully functional metal-CNT hybrid electromechanical probes were demonstrated. 1.5 Ohm resistance at  $50\mu m$  over-travel was achieved for a column of  $200\mu m \times 200\mu m$  cross-section and  $1\mu m$  of Au deposition. Further Au deposition decreased resistance to  $170mOhm$  but in the expense of reduced reliable over-travel of  $10\mu m$ . It was found that excessive metal deposition

results in a failure mechanism where the continuity of the metal layer is broken at the top surface of the CNT column.

Chapter 6 presented artistic scanning electron microscope images of CNT structures modified by controlled buckling, sputter etching, focused ion beam cutting and etching as well as CNT structures coated with *Pd* by electroless plating method. The limitation for the art community, however, is the resources needed to utilize these techniques. The equipment used for these techniques, including the very method of taking the images, namely scanning electron microscope, are very expensive tools. Nevertheless, until SEM becomes a commodity in the future, these observations can at least stimulate the creativity of scientist who have access to these tools.

Fundamental contributions of this thesis can be summarized as:

- Methodology for mechanical characterization of VA-CNT structures
- In-situ scanning electron microscope mechanical testing of CNT structures
- Demonstration of stiffness tuning by controlled compression and buckle formation of CNT column
- Demonstration of stiffness tuning by controlling gas composition during growth
- Investigation of the relationship between CNT growth method, resulting CNT structures, and macro-scale mechanical behavior.
- Transfer printing technique to simultaneously transfer, densify and electrically connect CNT structures onto metal substrates.
- Methodology for characterizing electrical properties of VA-CNT structures.
- Metal formation on CNT structures for increased electrical conduction.
- Metal-CNT hybrid electrical probe design where VA-CNT acts as elastic spring and metal coating serves for improved electrical conduction
- Demonstration of first fully functional electromechanical probes made fully of CNTs.
- Models and design guidelines for CNT probe design.

This thesis developed a framework to fabricate, characterize and design CNT structures for electromechanical probing applications. Insight into the CNT structures as functional materials is gained and important factors affecting the performance of this structures is identified and analyzed.

## **7.2 Recommendations for Future Work**

Recommendations for future work can be summarized in the following subgroups:

### **CNT Growth**

CVD growth techniques provides a scalable approach to manufacture CNT structures. However, many issues such as growth rate control, height uniformity and loading effects, are outstanding. In other words, the growth methods need to be optimized to obtain robust growth. It should be emphasized that this is a very active research area and the growth mechanisms, effect of CVD gasses on the catalyst particles, and many other variables, are still under investigation. These investigations are very critical in terms of achieving control over intrinsic properties of CNTs independently. For example, independent control of CNT density without effecting the CNT diameter would be a great stiffness tuning tool for CNT probes. Similarly for the case of floating catalyst CVD, effect of individual process conditions such as syringe pump rate, catalyst concentration, steel bottle temperature and tube furnace temperature should be investigated for predictive control of CNT film properties.

### **Mechanical Characterization**

Primarily due to the backlash problem described in 3, a comprehensive study of the cyclic behavior of the CNT structures could not be performed. To overcome this problem, direct measurement of the sensor tip/punch combined with feedback control to accurately impose displacement should be employed. This would also eliminate the need to compensate for the load sensor stiffness when extracting mechanical properties of the CNT structures under test. In-situ SEM mechanical compression test were performed without measuring force or displacement. Even though this technique provided very valuable insight into the deformation mechanism, integrated sensors enabling in-situ measurements could enable further understanding.

### **Stiffness Tuning by Controlling CVD Gas Composition**

This thesis demonstrated that stiffness of CNT structures can be tuned by changing CVD growth parameters. This is a very new field and has promising applications where there are geometric constraints, such as required pitch for probing applications, and the only parameter to be tuned is the intrinsic material properties in hand. This is very difficult with conventional materials. With CNTs, however, stiffness of CNT structures can be tuned as desired. This thesis presented two growth conditions for the fixed catalyst method, i.e. with and without hydrogen flush, and future work needs to address more experiments to address the space in between these two extreme cases, as well as beyond, the ability of tuning the stiffness in small increments as the ultimate goal. This thesis also demonstrated that CNT structures grown with floating catalyst are in completely different regime than the ones grown with fixed catalyst recipe. Future work needs to explore the space between these two fundamentally different regimes.

#### **Stiffness Tuning by Controlled Initial Deformation**

This thesis demonstrated a novel method of tuning the stiffness of CNT structures by controlling the initial deformation imposed on the structures, namely by controlling the ultimate plastic deformation and thereby the number of buckles formed. It is shown that this technique works for the CNT structures grown with fixed catalyst method only. This method has important implications. For example, in a situation where thousands of probes need to be the same height, and there are nonuniformities in column heights due to the CVD growth, the columns can be compressed collectively until they have the same height, thereby achieving planarization, and yet, keeping the stiffness values within the usable range. Future work needs to address the stiffness tuning mechanism for various column heights for scalable applications.

#### **Cycle Operation**

This thesis presented mechanical testing of CNT structures for characterization of the deformation mechanism. For most applications, especially for electro-mechanical probes, cyclic operation is critical. A systematic study of the effect of number of cycles on the stiffness and plastic deformation is required to be able to reliably use CNT structures in real applications.

#### **Buckling Mechanism**

Chapter 3 analyzed the deformation mechanism and modeled the stiffness mechanism of the CNT structures. Further investigation is necessary to understand the buckle formation and the associated forces involved with the process. The buckling of CNT structures is complicated

requires very careful experimentation. The first issue that needs to be addressed is the fact that as a CNT column is compressed, the force required to form individual buckle increase. For example, the force required to form the third buckle is larger than the force required to form the second buckle. This can be attributed to the fact that during the formation of the previous buckle, there is densification happening at the interface where the aligned portion joins the buckled portion. Another hypothesis is that the top aligned portion behaves similar to Euler-type buckling, where buckling force is inversely proportional to the length of a column which undergoes buckling. As more buckles form, the length of the top portion becomes shorter, which can be the cause of the increased buckling force. For both hypothesis, different height columns needs to be tested for the buckling force causing the first buckle. If the force required to form the first buckle is independent of the columns height, and is only a function of column area, then this would rule out the Euler-type buckling hypothesis.

### **Transfer Technique**

The transfer technique utilized in this thesis resulted in simultaneous densification and stiffening of the CNT structures due to the penetration of the epoxy used during the process. An ideal transfer process should not interfere with the mechanical properties for predictive design. Further work could investigate various epoxy/adhesive mixtures to affect the wetting properties of the CNTs and thereby avoiding the penetration.

Another issue discussed in Chapter 4 was the yield issue due to the non-uniform growth of the CNT columns resulting in partial transfer. This problem can be overcome by planarization techniques such as focused ion beam cutting of individual CNTs, controlled compression prior to transfer process, or by EDM cutting of all columns in a die at once as a more scalable approach.

### **Metal Coating**

As discussed in Chapter 5, the sputtered metal doesn't penetrate into the CNT structure. The amount of metal required to achieve low resistance values result in a thick outer metal shell around the CNT structures which interferes with the mechanical properties, and effectively reducing the resulting over-travel. It should be emphasized that the resistance values measured in Chapter 5 were bulk resistance values including the contact resistance between the punch and the top surface of the CNT column, bulk resistance of the column, and the resistance

between the column and the Au layer on the growth substrate, which was achieved only through the circumference of the bottom section since the columns were grown on an oxide layer. A systematic study can be performed to separate these resistances from each other where the length and the area of the column can be varied and by careful design of experiments the individual contributions of the resistance components mentioned above can be identified.

### **Failure Mechanism of Hybrid Metal-CNT Probes**

Chapter 5 discussed common failure mechanisms of hybrid Metal-CNT probes. These can be further investigated to understand under what strain levels the metal coating starts yielding. Assuming a thin uniform metal shell around a CNT column, the vertical stiffness of the metal layer can be calculated as:

$$k_{metal} = E_{metal} \frac{\pi D t}{L} \quad (7.1)$$

where  $t$  is the film thickness and  $D$  is the CNT diameter. Assuming good adhesion to the CNT walls, the deformation of the CNT structure should be small enough to avoid metal yielding. However, it can be generally said that, if the metal shell is much softer than the CNT structure, that is

$$k_{CNT} \gg k_{metal} \quad (7.2)$$

the metal will recover after deformation and the structure will spring back after the compression. The above discussion is valid for vertical compression of a CNT. However, as observed during the tests and in-situ experiments, the deformation of CNT columns is mostly bending based, most probably a combination of vertical compression and bending, which makes the problem rather complicated. Figure 7-1 illustrates the failure mechanism often observed after deformation. The other important factor is the thickness of the metal layer. As discussed in Chapter 5, for good electrical properties, thick layers of metal coatings are necessary.

It should be also noted that, during deformation, the CNTs aren't able to bend freely. They are constrained by other CNTs around them and during compression it is very likely that they are rubbing against each other, which might be another reason responsible for metal failure. For this purpose, in-situ SEM mechanical testing and detailed observation would be very useful.

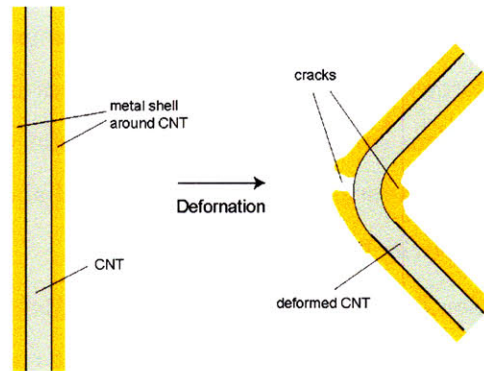


Figure 7-1: Failure mechanism of metal layer around a CNT.

And finally, as the thickness of the film becomes larger and larger, the CNTs covered with metal aren't free to move at all, as shown in Figure 5-9 which makes the problem more of a metal shell coated around the whole CNT column than metal coated an individual CNT.

### Alternative Column Geometries

As an alternative to the column geometries discussed in this thesis, hollow columns, as shown in Figure 7-2 can have certain advantages. First, this geometry gives more flexibility in terms of stiffness control. For example, if the columns at a certain pitch prove to be too stiff, then the hollow cylinder design can be a solution as the stiffness of CNT columns scale directly with the area, as discussed in Chapter 3.

Another advantage is the increased area for metal coating. During metal coating process, such as sputtering, the internal wall of the column will also be sputtered, in addition to the outer wall, which will enable to obtain the same electrical performance with a thinner metal shell, and thereby compromising the mechanical properties of the CNT column much less.

### Outlook

This thesis is provided an introduction to bridge CNT growth process conditions to macro level mechanical properties of CNT structures. A better understanding of the relations between various conditions and interdependencies of inherent CNT properties and resulting physical properties are crucial for robust design. Even though the analysis in this thesis was done in the context of electromechanical probes, most of the findings are useful for many other



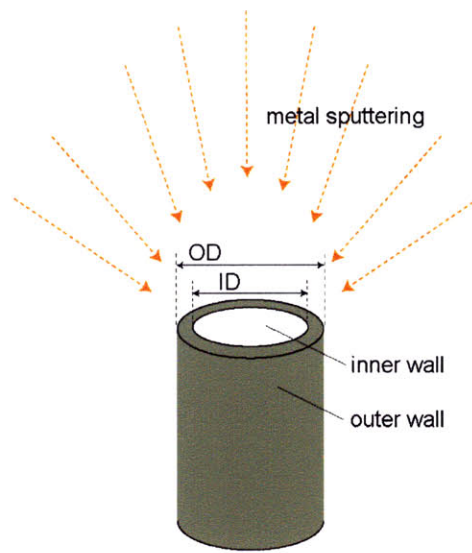


Figure 7-2: Hollow cylinder column design.

structural application such as energy absorption and storage. To get a better understanding of the relationship between inherent CNT properties and macro-mechanical properties, external means can be used to modify the structural properties. For example, to independently control the CNT density of a structure without affecting the CNT diameter, a column can be squeezed laterally and densified to a predetermined amount and then the structure can be tested in vertical direction. Chapter 3 already presented lateral compression results and the next logical step would be to systematically squeeze them and test in vertical direction.

As presented in Chapter 6, etching techniques such as sputter etching, reactive ion etching or focused ion milling can create sharp tips made of CNTs. These resulting structures can be further investigated to explore their potential benefit as contacting surfaces. Due their very sharp nature, they can prove useful in penetrating into oxide surfaces, which is achieved through lateral scrubbing in most conventional probing applications. However, it still needs to be determined if these sharp tips will accumulate material and clog. If so, cleaning techniques to prepare the probe for subsequent operations need to be investigated.

The buckling mechanism investigation revealed that the buckle size is independent of the geometry. An interesting question is if the models developed in the thesis would hold if the

column size shrink further to levels that becomes comparable with buckle size. A thorough investigation of this could enable the design of hollow CNT columns which would have the advantage of additional metal deposition area inside the columns.

As depicted in Chapter 6, CNT structures also present a very suitable and interesting platform for artists. The only limitation is that the tools used to create the images are very expensive and difficult to access for artistic purposes. However, as the technology evolves and these tools become more accessible and cheaper, this platform can generate very interesting works of art.

# Bibliography

- [1] M. S. Dresselhaus, Y. M. Lin, O. Rabin, A. Jorio, A. G. Souza, M. A. Pimenta, R. Saito, G. G. Samsonidze, and G. Dresselhaus, “Nanowires and nanotubes,” *Materials Science and Engineering C*, vol. 23, no. 1, pp. 129–140, 2003.
- [2] M. Dresselhaus, G. Dresselhaus, and P. Avouris, *Carbon nanotubes : Synthesis, Structure, Properties, and Applications. Topics in Applied Physics*. Berlin: Springer, 2001, vol. 80.
- [3] C. Stampfer, T. Helbling, D. Oberfell, B. Schoberle, M. K. Tripp, A. Jungen, S. Roth, V. M. Bright, and C. Hierold, “Fabrication of single-walled carbon-nanotube-based pressure sensors,” *Nano Letters*, vol. 6, no. 2, pp. 233–237, 2006.
- [4] R. H. Baughman, C. X. Cui, A. A. Zakhidov, Z. Iqbal, J. N. Barisci, G. M. Spinks, G. G. Wallace, A. Mazzoldi, D. De Rossi, A. G. Rinzler, O. Jaschinski, S. Roth, and M. Kertesz, “Carbon nanotube actuators,” *Science*, vol. 284, no. 5418, pp. 1340–1344, 1999.
- [5] S. Courty, J. Mine, A. R. Tajbakhsh, and E. M. Terentjev, “Nematic elastomers with aligned carbon nanotubes: New electromechanical actuators,” *Europhysics Letters*, vol. 64, no. 5, pp. 654–660, 2003.
- [6] G. M. Spinks, G. G. Wallace, L. S. Fifield, L. R. Dalton, A. Mazzoldi, D. De Rossi, I. I. Khayrullin, and R. H. Baughman, “Pneumatic carbon nanotube actuators,” *Advanced Materials*, vol. 14, no. 23, pp. 1728–+, 2002.
- [7] Y. Yun, V. Shanov, Y. Tu, M. J. Schulz, S. Yarmolenko, S. Neralla, J. Sankar, and S. Subramaniam, “A multi-wall carbon nanotube tower electrochemical actuator,” *Nano Letters*, vol. 6, no. 4, pp. 689–693, 2006.

- [8] Y. H. Yun, V. Shanov, M. J. Schulz, Z. Y. Dong, A. Jazieh, W. R. Heineman, H. B. Halsall, D. K. Y. Wong, A. Bange, Y. Tu, and S. Subramaniam, "High sensitivity carbon nanotube tower electrodes," *Sensors and Actuators B-Chemical*, vol. 120, no. 1, pp. 298–304, 2006.
- [9] S. S. Fan, W. J. Liang, H. Y. Dang, N. Franklin, T. Tombler, M. Chapline, and H. J. Dai, "Carbon nanotube arrays on silicon substrates and their possible application," *Physica E*, vol. 8, no. 2, pp. 179–183, 2000.
- [10] Z. W. Pan, S. S. Xie, B. H. Chang, L. F. Sun, W. Y. Zhou, and G. Wang, "Direct growth of aligned open carbon nanotubes by chemical vapor deposition," *Chemical Physics Letters*, vol. 299, no. 1, pp. 97–102, 1999.
- [11] Y. C. Choi, Y. M. Shin, Y. H. Lee, B. S. Lee, G. S. Park, W. B. Choi, N. S. Lee, and J. M. Kim, "Controlling the diameter, growth rate, and density of vertically aligned carbon nanotubes synthesized by microwave plasma-enhanced chemical vapor deposition," *Applied Physics Letters*, vol. 76, no. 17, pp. 2367–2369, 2000.
- [12] G. Y. Zhang, D. Mann, L. Zhang, A. Javey, Y. M. Li, E. Yenilmez, Q. Wang, J. P. McVittie, Y. Nishi, J. Gibbons, and H. J. Dai, "Ultra-high-yield growth of vertical single-walled carbon nanotubes: Hidden roles of hydrogen and oxygen," *Proceedings of the National Academy of Sciences of the United States of America*, vol. 102, no. 45, pp. 16 141–16 145, 2005.
- [13] L. B. Zhu, Y. H. Xiu, D. W. Hess, and C. P. Wong, "Aligned carbon nanotube stacks by water-assisted selective etching," *Nano Letters*, vol. 5, no. 12, pp. 2641–2645, 2005.
- [14] A. Cao, R. Baskaran, M. J. Frederick, K. Turner, P. M. Ajayan, and G. Ramanath, "Direction-selective and length-tunable in-plane growth of carbon nanotubes," *Advanced Materials*, vol. 15, no. 13, pp. 1105–+, 2003.
- [15] A. Y. Cao, P. L. Dickrell, W. G. Sawyer, M. N. Ghasemi-Nejhad, and P. M. Ajayan, "Super-compressible foamlike carbon nanotube films," *Science*, vol. 310, no. 5752, pp. 1307–1310, 2005.

- [16] L. J. Ci, Z. L. Rao, Z. P. Zhou, D. S. Tang, Y. Q. Yan, Y. X. Liang, D. F. Liu, H. J. Yuan, W. Y. Zhou, G. Wang, W. Liu, and S. S. Xie, "Double wall carbon nanotubes promoted by sulfur in a floating iron catalyst cvd system," *Chemical Physics Letters*, vol. 359, no. 1-2, pp. 63–67, 2002.
- [17] Y. Y. Fan, A. Kaufmann, A. Mukasyan, and A. Varma, "Single- and multi-wall carbon nanotubes produced using the floating catalyst method: Synthesis, purification and hydrogen up-take," *Carbon*, vol. 44, no. 11, pp. 2160–2170, 2006.
- [18] S. M. Huang, X. Y. Cai, C. S. Du, and J. Liu, "Oriented long single walled carbon nanotubes on substrates from floating catalysts," *Journal of Physical Chemistry B*, vol. 107, no. 48, pp. 13 251–13 254, 2003.
- [19] X. S. Li, A. Y. Cao, Y. J. Jung, R. Vajtai, and P. M. Ajayan, "Bottom-up growth of carbon nanotube multilayers: Unprecedented growth," *Nano Letters*, vol. 5, no. 10, pp. 1997–2000, 2005.
- [20] W. C. Ren, F. Li, and H. M. Cheng, "Evidence for, and an understanding of, the initial nucleation of carbon nanotubes produced by a floating catalyst method," *Journal of Physical Chemistry B*, vol. 110, no. 34, pp. 16 941–16 946, 2006.
- [21] G. B. Zheng, Y. F. Shi, J. W. Feng, and J. K. Guo, "Morphology and structure of carbon nanotube synthesized continuously by floating catalysis of hydrocarbon," *Journal of Inorganic Materials*, vol. 16, no. 5, pp. 945–950, 2001.
- [22] Z. P. Zhou, L. J. Ci, X. H. Chen, D. S. Tang, X. Q. Yan, D. F. Liu, Y. X. Liang, H. J. Yuan, W. Y. Zhou, G. Wang, and S. S. Xie, "Controllable growth of double wall carbon nanotubes in a floating catalytic system," *Carbon*, vol. 41, no. 2, pp. 337–342, 2003.
- [23] R. Andrews, D. Jacques, A. M. Rao, F. Derbyshire, D. Qian, X. Fan, E. C. Dickey, and J. Chen, "Continuous production of aligned carbon nanotubes: a step closer to commercial realization," *Chemical Physics Letters*, vol. 303, no. 5-6, pp. 467–474, 1999.

- [24] M. Taniguchi, H. Nagao, M. Hiramatsu, Y. Ando, and M. Hori, "Preparation of dense carbon nanotube film using microwave plasma-enhanced chemical vapor deposition," *Diamond and Related Materials*, vol. 14, no. 3-7, pp. 855–858, 2005.
- [25] K. B. K. Teo, S. B. Lee, M. Chhowalla, V. Semet, V. T. Binh, O. Groening, M. Castignolles, A. Loiseau, G. Pirio, P. Legagneux, D. Pribat, D. G. Hasko, H. Ahmed, G. A. J. Amaratunga, and W. I. Milne, "Plasma enhanced chemical vapour deposition carbon nanotubes/nanofibres - how uniform do they grow?" *Nanotechnology*, vol. 14, no. 2, pp. 204–211, 2003.
- [26] Y. Yao, L. K. L. Falk, R. E. Morjan, O. A. Nerushev, and E. E. B. Campbell, "Cross-sectional tem investigation of nickel-catalysed carbon nanotube films grown by plasma-enhanced cvd," *Journal of Microscopy-Oxford*, vol. 219, pp. 69–75, 2005.
- [27] M. Chhowalla, K. B. K. Teo, C. Ducati, N. L. Rupesinghe, G. A. J. Amaratunga, A. C. Ferrari, D. Roy, J. Robertson, and W. I. Milne, "Growth process conditions of vertically aligned carbon nanotubes using plasma enhanced chemical vapor deposition," *Journal of Applied Physics*, vol. 90, no. 10, pp. 5308–5317, 2001.
- [28] X. Chen, Z. Hu, X. Z. Wang, Q. Wu, Y. Chen, S. G. Yang, and Y. W. Du, "Well-aligned carbon nanotube array synthesized at low temperature by microwave plasma enhanced chemical vapor deposition," *Chemical Journal of Chinese Universities-Chinese*, vol. 22, no. 5, pp. 731–733, 2001.
- [29] Y. A. Kim, T. Hayashi, M. Endo, Y. Kaburagi, T. Tsukada, J. Shan, K. Osato, and S. Tsuruoka, "Synthesis and structural characterization of thin multi-walled carbon nanotubes with a partially faceted cross section by a floating reactant method," *Carbon*, vol. 43, no. 11, pp. 2243–2250, 2005.
- [30] M. Nihei, A. Kawabata, and Y. Awano, "Direct diameter-controlled growth of multiwall carbon nanotubes on nickel-silicide layer," *Japanese Journal of Applied Physics Part 2-Letters*, vol. 42, no. 6B, pp. L721–L723, 2003.

- [31] A. J. Hart and A. H. Slocum, "Rapid growth and flow-mediated nucleation of millimeter-scale aligned carbon nanotube structures from a thin-film catalyst," *Journal of Physical Chemistry B*, vol. 110, no. 16, pp. 8250–8257, 2006.
- [32] A. Y. Cao, P. L. Dickrell, W. G. Sawyer, M. N. Ghasemi-Nejhad, and P. M. Ajayan, "Super-compressible foamlike carbon nanotube films," *Science*, vol. 310, no. 5752, pp. 1307–1310, 2005.
- [33] N. Yamamoto, E. J. Garcia, A. J. Hart, B. L. Wardle, and A. H. Slocum, "Fabrication and multifunctional characterization of hybrid woven composites reinforced by aligned carbon nanotubes," in *16th International Conference on Composite Materials*, Kyoto, Japan, 2007.
- [34] M. F. Ashby, *Materials Selection in Mechanical Design*. Butterworth-Heinemann Ltd, 2004.
- [35] R. W. Pekala, T. Tillostson, C. Alviso, J. Poco, and J. LeMay, "A comparison of mechanical properties and scaling law relationships for silica aerogels and their organic counterparts," in *MRS Symposium*, Boston, Massachusetts, USA, 1990.
- [36] M. B. Bryning, M. F. Islam, J. M. Kikkawa, and A. G. Yodh, "Very low conductivity threshold in bulk isotropic single-walled carbon nanotube-epoxy composites," *Advanced Materials*, vol. 17, no. 9, pp. 1186–+, 2005.
- [37] S. M. Huang, L. M. Dai, and A. W. H. Mau, "Patterned growth and contact transfer of well-aligned carbon nanotube films," *Journal of Physical Chemistry B*, vol. 103, no. 21, pp. 4223–4227, 1999.
- [38] T. Jeong, J. Heo, J. Lee, S. Lee, W. Kim, H. Lee, S. Park, J. M. Kim, T. Oh, C. Park, J. B. Yoo, B. Gong, N. Lee, and S. Yu, "Improvement of field emission characteristics of carbon nanotubes through metal layer intermediation," *Applied Physics Letters*, vol. 87, no. 6, pp. –, 2005.
- [39] L. B. Zhu, Y. Y. Sun, D. W. Hess, and C. P. Wong, "Well-aligned open-ended carbon nanotube architectures: An approach for device assembly," *Nano Letters*, vol. 6, no. 2, pp. 243–247, 2006.

- [40] Y. J. Jung, S. Kar, S. Talapatra, C. Soldano, G. Viswanathan, X. S. Li, Z. L. Yao, F. S. Ou, A. Avadhanula, R. Vajtai, S. Curran, O. Nalamasu, and P. M. Ajayan, “Aligned carbon nanotube-polymer hybrid architectures for diverse flexible electronic applications,” *Nano Letters*, vol. 6, no. 3, pp. 413–418, 2006.
- [41] N. Chakrapani, B. Q. Wei, A. Carrillo, P. M. Ajayan, and R. S. Kane, “Capillarity-driven assembly of two-dimensional cellular carbon nanotube foams,” *Proceedings of the National Academy of Sciences of the United States of America*, vol. 101, no. 12, pp. 4009–4012, 2004.
- [42] L. Gibson and M. Ashby, *Cellular Solids : Structure and Properties*, ser. Cambridge solid state science series. Cambridge: Cambridge University Press, 1997, vol. xviii.
- [43] L. Liu, C. S. Jayanthi, M. J. Tang, S. Y. Wu, T. W. Tomblor, C. W. Zhou, L. Alexseyev, J. Kong, and H. J. Dai, “Controllable reversibility of an  $sp(2)$  to  $sp(3)$  transition of a single wall nanotube under the manipulation of an afm tip: A nanoscale electromechanical switch?” *Physical Review Letters*, vol. 84, no. 21, pp. 4950–4953, 2000.
- [44] M. B. Nardelli and J. Bernholc, “Mechanical deformations and coherent transport in carbon nanotubes,” *Physical Review B*, vol. 60, no. 24, pp. R16 338–R16 341, 1999.
- [45] A. Rochefort, P. Avouris, F. Lesage, and D. R. Salahub, “Electrical and mechanical properties of distorted carbon nanotubes,” *Physical Review B*, vol. 60, no. 19, pp. 13 824–13 830, 1999.
- [46] A. Maiti, A. Svizhenko, and M. P. Anantram, “Electronic transport through carbon nanotubes: Effects of structural deformation and tube chirality,” *Physical Review Letters*, vol. 88, no. 12, pp. –, 2002.
- [47] E. D. Minot, Y. Yaish, V. Sazonova, J. Y. Park, M. Brink, and P. L. McEuen, “Tuning carbon nanotube band gaps with strain,” *Physical Review Letters*, vol. 90, no. 15, pp. –, 2003.



- [48] T. W. Tombler, C. W. Zhou, L. Alexseyev, J. Kong, H. J. Dai, L. Lei, C. S. Jayanthi, M. J. Tang, and S. Y. Wu, "Reversible electromechanical characteristics of carbon nanotubes under local-probe manipulation," *Nature*, vol. 405, no. 6788, pp. 769–772, 2000.
- [49] V. Semet, V. T. Binh, D. Guillot, K. B. K. Teo, M. Chhowalla, G. A. J. Amaratunga, W. I. Milne, P. Legagneux, and D. Pribat, "Reversible electromechanical characteristics of individual multiwall carbon nanotubes," *Applied Physics Letters*, vol. 87, no. 22, pp. –, 2005.
- [50] S. Agrawal, M. J. Frederick, F. Lupo, P. Victor, O. Nalamasu, and G. Ramanath, "Directed growth and electrical-transport properties of carbon nanotube architectures on indium tin oxide films on silicon-based substrates," *Advanced Functional Materials*, vol. 15, no. 12, pp. 1922–1926, 2005.
- [51] L. B. Zhu, J. W. Xu, Y. H. Xiu, Y. Y. Sun, D. W. Hess, and C. P. Wong, "Growth and electrical characterization of high-aspect-ratio carbon nanotube arrays," *Carbon*, vol. 44, no. 2, pp. 253–258, 2006.